Development of an Obround Polybenzimidazole Nozzle for Cold Gas Dynamic Spray

By

Samuel Croteau

Thesis submitted to the Department of Mechanical Engineering in partial fulfillment of the requirements for the degree of

Master of Applied Science

in Mechanical Engineering

University of Ottawa

Ottawa, Ontario, Canada

September 29th, 2020

ABSTRACT

Technoform, a worldwide manufacturer of polymer window frames and window insulation, needs to fulfill customer performance and aesthetic requirements. To this end, they have opted to use the Cold Gas Dynamic Spray (CGDS) process on an industrial scale to coat extruded polymer parts with a thin layer of aluminum. The CGDS process would be an added step in the production line where it would deposit an aluminum coating after the extrusion step, in a single pass. While commercially available equipment can be utilized for this purpose, it is rather inefficient due to the quantity of nozzles required to fulfill Technoform Bautec Ibérica's requirement of coating the substrate in a single pass. Multiple nozzles placed side-by-side would be required to coat the entire width of the substrate.

The focus of this work was to improve and optimise a prototype initially designed by Technoform Bautec Ibérica and Centerline (Windsor) Ltd. This prototype was designed with an obround shape (12.5 x 2.5 mm), to be wider than axisymmetric nozzles and reduce the number of nozzles needed for this specific application. A combination of computational and experimental methods were used to assess the issues with the tungsten carbide (WC) prototype produced by Technoform and Centerline (Windsor). Alternate injection points for the powder feedstock were tested through simulations to improve the particle distribution at the outlet of the nozzle. It was found that a 15° inlet provided a fuller coverage of particles at the outlet when compared to the original inlet, which was at the 90° position. A new, multi-part prototype was designed to be manufactured from polybenzimidazole (PBI) and to utilize the updated inlet position. The WC nozzle produced a single-pass coating of 6.5 mm in width on an aluminum 6061-T6 substrate, while the PBI prototype produced a 7.5 mm wide coating. Further simulations showed that a dual injection approach could provide a wider coating. The PBI prototype was modified for dual injection and produced a 10.5 mm wide coating. With optimised parameters, a 13.6 mm single-pass coating was produced. Different injection gas flow rates were also tested to produce flatter coatings. A gas flow rate of 6.52×10^{-4} kg/s (60 SCFH) produced the most even coating in terms of thickness across the entire width of the deposition. Finally, single-pass coatings were deposited on Technoform's polyamide substrate. The WC nozzle produced an 8.6 mm coating and the dual injection PBI nozzle produced a 13 mm coating.

ACKNOWLEDGEMENTS

I would first like to thank my supervisor, Dr. Bertrand Jodoin, for his guidance and support throughout the project and thesis writing. I very much enjoyed and appreciated working with you over the past few years! Thank you for taking me on your team of graduate students, I have learned a lot from everyone, and it has had a significant impact on my life.

A big thank you as well to our industrial partners, Technoform Bautec Ibérica and Centerline (Windsor) Ltd. for entrusting the project to us, and for their financial contribution towards the project. I hope they are satisfied with the end result and wish them all the best with the other aspects of development! I would also like to thank Boedeker Plastics Inc. for their willingness to work with us on the development of the nozzle prototype and overcoming manufacturing challenges. A special thanks to Dan Giossi from Boedeker as well, thank you for your prompt answers and your help with the prototyping process. Your professional input and recommendations were greatly appreciated.

I would also like to thank my fellow lab members, for their help, suggestions, and friendship during my time as a graduate student; Daniel MacDonald, Aleksandra Nastic, Maryam Razavipour, Amir Daoud, Saeed Rahmati, Rocio Dominguez, Roberto Fernandez, Justin Perry, Deliang (Leon) Guo, Roghayeh Nikbakht, and last but not least Mathieu Hinse. You have all made this an incredible experience, and I hope to stay in contact with all of you in the future.

I wish to thank the technicians from the machine shop at the University of Ottawa for sharing their insight and wealth of knowledge of the machining industry and processes, especially Stan, Jacques, and Paul. Your input and skills were essential for this project.

And finally, thanks to all my friends and family who were along for the ride. You were there for the highs and lows, whether on the professional or emotional side. I cannot begin to thank you enough; I could not have done without you. I hope some of you can forgive me for being dragged into graduate studies with me; François “Frodo” Lepage, Mathieu “Marchi” Marchildon, and Mathieu “Chest Bras” Hinse. Also, a very special thank you to Sarah Carson, for being by my side through thick and thin.

TABLE OF CONTENTS

LIST OF FIGURES

LIST OF TABLES

ACRONYMS

BSE	Back Scattered Electron
CAD	Computer-Aided Design
CFD	Computational Fluid Dynamics
CGDS	Cold Gas Dynamic Spray
CT	X-ray Computed Tomography
DE	Deposition Efficiency
DPM	Discrete Phase Model
DT	Divergence Theorem
EBDS	Electron Backscatter Diffraction
EDS	Energy Dispersive Spectroscopy
FVM	Finite Volume Method
LS	Least Squares
NRC	National Research Council
PBI	Polybenzimidazole (Celazole®)
PPF	Primary Powder Feeder
RANS	Reynolds-Averaged Navier Stokes
RNG	Renormalization Group
RPM	Revolutions Per Minute
SCFH	Standard Cubic Feet per Hour
SE	Secondary Electron
SEM	Scanning Electron Microscope
SIMPLE	Semi-Implicit Method for Pressure Linked Equations
SPF	Secondary Powder Feeder
SS	Stainless Steel
WC	Tungsten Carbide

NOMENCLATURE

∇T	Temperature gradient	[K]
ρ	Density	[kg/m^3]
ρ_0	Stagnation density	[kg/m^3]
ρ_{gas}	Gas density	[kg/m^3]
ρ_p	Density of the particle	[kg/m^3]
τ_{eff}	Viscous dissipation term	
μ	Dynamic viscosity	[Pa·s]
A	Area	[m^2]
A^*	Cross-sectional area at the nozzle throat	[m^2]
A_p	Projected area of the particle	[m^2]
a_1, a_2, a_3	Spherical drag law constants	
a_p	Acceleration of the particle	[m/s^2]
C_D	Drag coefficient	
C_p	Heat capacity (constant pressure)	[kJ/kg·K]
C_v	Heat capacity (constant volume)	[kJ/kg·K]
c	Speed of sound	[m/s]
d	Distance between nodes	[m]
d_p	Diameter of the particle	[m]
E	Energy	[kJ]
F_D	Drag force	[N]
G	Geometry factor	
$\vec{g}$	Gravitational acceleration	[m/s^2]
h_s	Enthalpy	[kJ/kg·K]
I	Unit tensor	
$\vec{J}_j$	Diffusion flux term	
k	Specific heat ratio	
k_{eff}	Effective conductivity	[W/m·K]

M	Molar mass	[kg/kmol]
M_a	Local Mach number	
$\dot{m}$	Mass flow rate	[kg/s]
m_p	Mass of the particle	[kg]
P	Static pressure	[MPa]
P_0	Stagnation pressure	[MPa]
P_{gas}	Gas pressure	[MPa]
R	Specific gas constant	[kJ/kg·K]
$\bar{R}$	Universal gas constant	[kJ/kmol·K]
Re	Reynolds number	
S_h	Source term (heat sources)	[W]
S_m	Source term (mass)	[kg/s]
T_0	Stagnation temperature	[K]
T_{gas}	Gas temperature	[K]
T_n	Temperature at cell centroid n	[K]
T_p	Temperature in starting cell centroid p	[K]
t	Time	[s]
$\vec{u}$	Velocity vector	[m/s]
V	Velocity	[m/s]
V_{gas}	Gas velocity	[m/s]
V_p	Particle velocity	[m/s]
V_r	Relative velocity between the gas flow and particle	[m/s]

1 INTRODUCTION

1.1 BACKGROUND

The use of surface coatings in the production of goods is widely utilized, and the Cold Gas Dynamic Spray (CGDS) process has established itself as a viable means of producing such coatings since the mid-1980s [1]. CGDS, also referred to as cold spray, is utilized as a solid-state coating technology in many industries to produce coatings for varied uses.

Of particular relevance currently, due to the worldwide coronavirus pandemic, are antimicrobial coatings which leverage the antimicrobial properties of copper to disinfect surfaces [2]. CGDS has shown to be an effective way to deposit this type of coating [3], [4]. However, protective cold sprayed coatings have typically been used in many domains, such as corrosion protection of magnesium in vehicles and airplanes [4]–[6], protection of air turbines in dry and humid climates [7], high-temperature oxidation prevention [8]–[11], and anti-fouling coatings for materials exposed to marine environments [8], [12], [13]. The process has also been used in other applications such as dimensional restoration and repair [1], [4], [14].

In an effort to improve and better understand this technology, many aspects of the process have been extensively researched. Other than basic process parameters, notable research areas include nozzle dimensions and Mach number limitations [15]–[17], the effect of the bow shock and standoff distance [18], [19], the performance and adhesion of different material combinations [20], [21], laser-assisted spraying and post treatment [22]–[24], post-spray annealing [25]–[27], evaluation of residual stresses [28]–[30], and surface pre-treatment [31]–[35]. Another area of development which is perhaps more relevant to the content of this thesis is polymer metallization [36]–[39].

While nozzle dimensions have been studied, one area of research that has been lacking with regards to nozzle geometry is the nozzle cross-section shape. Typically, the nozzles offered by commercial manufacturers of cold spray equipment are axisymmetric along the entire length of the nozzle, giving them a circular cross-section. However, *Alkhimov et al.* have suggested that the effects of the boundary layer on the final particle velocity should

be taken into further consideration, and that a possible solution is to use a nozzle with a thin, rectangular cross-section [40]. Figure 1.1 shows the nozzle shape and cross-section proposed by *Alkhimov et al.* [40] to resolve boundary layer issues.

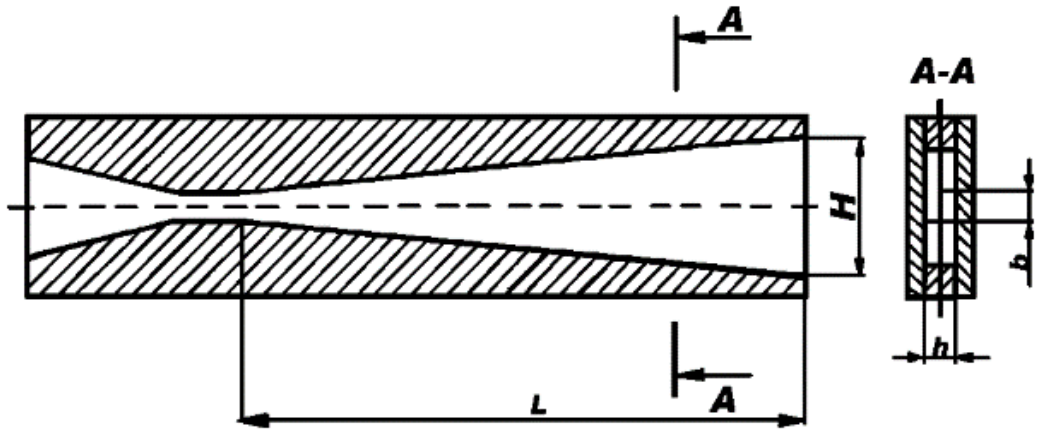

Figure 1.1 - Nozzle shape investigated by *Alkhimov et al.* [40] (© 2001 Springer Nature)

Another suggested advantage of the rectangular design is a decrease in gas consumption and a more even particle deposition compared to axisymmetric nozzles [40]. Since then, some computational analysis has been done to evaluate the effect of the nozzle cross-section for rectangular and oval nozzles by *Yin et al.* [41]. The effect of the radial injection angle, the expansion ratio, and traverse speed of multiple nozzles with rectangular cross-sections were also studied numerically and experimentally by *Varadaraajan et al.* [42].

In 2015, the National Research Council (NRC) of Canada filed a patent which included a diagram depicting nozzle cross-sectional shapes, shown in Figure 1.2 [43]. The schematic shows the cross-section of the nozzle exit plane and the spray profile produced by a single-track coating [43]. These single-track coatings are produced by spraying a single "line" onto the substrate. As initially proposed by *Alkhimov et al.* [40], the rectangular nozzle, and in this case the "hourglass" nozzle as well, both produce a wider and more consistent thickness across the nozzle width.

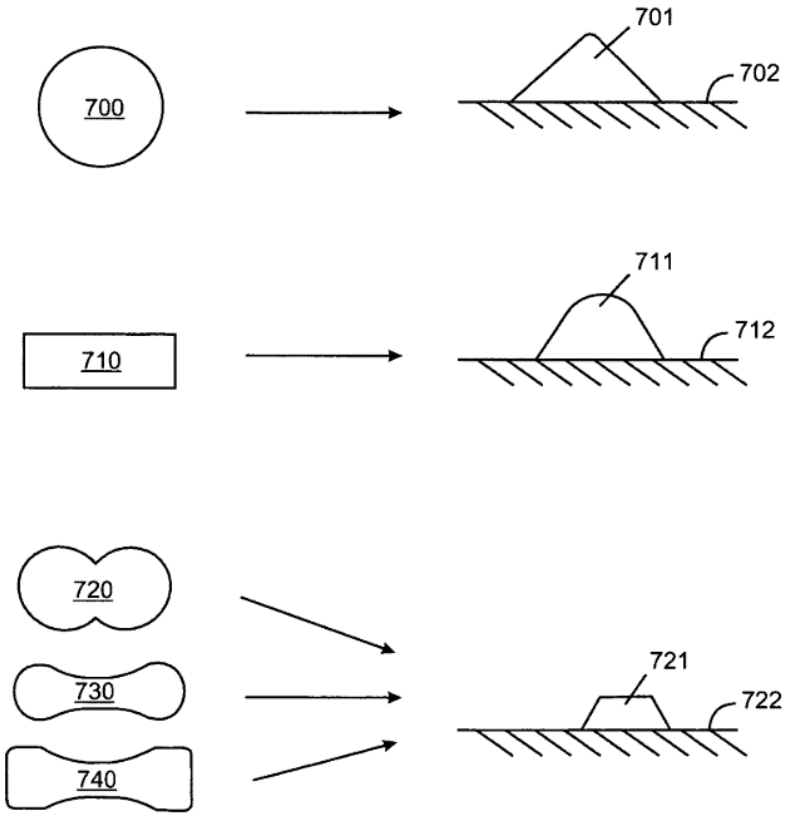

Figure 1.2 – Cross-sectional nozzle shapes patented by the NRC [43]

This makes alternate nozzle shapes an interesting prospect, as they have been shown to produce a more even coating thickness across the width of a single track compared to axisymmetric nozzles. [43]. This provides a flatter coating, as demonstrated by Figure 1.2.

1.2 RESEARCH OBJECTIVES

The motivation of this research is to investigate the possibility of improving the CDGS process by using a novel, non-axisymmetric nozzle profile. The goal is to produce, with a single pass, a wide coating of uniform thickness. The nozzle should also be adequate for use in an industrial setting for an extended period of time. This work was performed in collaboration with two industrial partners, Centerline (Windsor) Limited and Technoform Bautec Ibérica. The following steps were taken in order to complete this objective:

1. The flow characteristics of the initial WC obround prototype was simulated in CFD software, and particle-tracking was added to examine the particle distribution and velocity at the exit.

2. The nozzle was tested experimentally to validate and ensure the accuracy of the model.
3. Different powder injection points were tested through simulation to determine if particle distribution at the nozzle exit could be optimized.
4. A new PBI obround prototype was manufactured with an alternate injection location based on simulation results, and experimental tests were done to evaluate its performance compared to the initial obround nozzle.
5. The feasibility of a dual injection nozzle was investigated through simulations.
6. The PBI obround prototype was modified to add a second injection point for dual injection of powder.
7. Single-pass coatings were produced on aluminum and polymer substrates with the WC prototype and PBI dual injection prototype.
8. The coatings were evaluated to compare their characteristics and the efficacy of the dual injection obround nozzle to produce a wide track with even thickness.

1.3 THESIS CONTENT

The following thesis is arranged into six chapters. The content of each chapter is detailed in this subsection.

Chapter 1 is an introduction of the subject matter. This chapter also presents the motivations and objectives of the work.

Chapter 2 contains an overview of relevant literature, as well as previous work on this topic by the industrial partner. The first section of this chapter will outline the goals and challenges of this research, with regards to its industrial application. The second section will discuss the basics of the CGDS process and provide an overview of fundamental gas dynamics concepts. The third and final section of this chapter is an overview of current materials and manufacturing techniques utilized in the fabrication of CGDS nozzles.

Chapter 3 is a more in depth look at the research objectives. The sections contained in this chapter will outline the steps taken to achieve these objectives, and overcome the challenges and issues encountered.

Chapter 4 outlines the experimental procedure, including the materials used, and the equipment used for production and characterization of samples. This chapter will also provide details about the CFD simulations, such as the computational domain, domain meshing, governing equations of the model, convergence criteria, and mesh validation.

Chapter 5 discusses the results obtained through the experimental and numerical procedures performed to attain the research objectives. More specifically, this section presents the evolution of the obround nozzle design in terms of materials and manufacturing, as well as resulting single-track coatings on aluminum and polymer substrates. These results are also shown in comparison the original single injection WC obround nozzle and the CFD modelling.

Chapter 6, the closing chapter of this thesis, outlines the conclusions drawn from the work presented in the previous chapters. This is followed by recommendations on future work that should be performed to further the development of this nozzle. This chapter is followed by a list of references and relevant appendices.

2 LITERATURE REVIEW

2.1 INDUSTRIAL APPLICATION

This first subsection will present background information on the industrial partner, Technoform Bautec Ibérica, and the goals and challenges which motivated this research.

2.1.1 Goals

Technoform, founded in Germany in 1969, is a company focused on producing precise thermoplastic parts. The Technoform Bautec Ibérica division of the company is an international provider of extruded polymer strips for the insulation of aluminum windows, doors, and facades.

One of the company's current goals, in order to fulfill customer requirements, is to provide a polymer window frame with a coloured exterior. The company has opted not to use colour pigments in the production process due to European restrictions on the use of some pigments, such as cadmium pigments, as part of the REACH legislation (1907/2006) [44]. Another option to attain this goal is to paint the polymer profiles. However, the paint adheres poorly to the polymer material and does not provide sufficient durability to be a viable option.

Finally, the company has settled on the metallization of the polymer surface. The aim is to deposit a thin metal layer of consistent thickness, which would essentially act as a primer for the paint. As the paint adheres to aluminum, they have decided to opt for an aluminum coating deposited through CGDS. Their final goal is to integrate CGDS as an in-situ metallization step in the extrusion process for the window frame production.

2.1.2 Challenges

Prior to this project, Technoform Bautec Ibérica had already performed some CGDS testing to assess the feasibility of metallizing their extruded polymer profiles. The profiles are to be coated in-situ, as part of the extrusion process, while they exit the extruder at a velocity of 2 m/s. This is a significant challenge, as the substrate moves at a high velocity under the spray nozzle.

Initial in-situ metallization tests done by Technoform Bautec Ibérica were performed using an axisymmetric metal nozzle. However, one of the main issues encountered was not related to the high velocity of the substrate. While using this nozzle with the pure aluminum feedstock powder, Technoform encountered frequent nozzle clogging. This is an obvious challenge in this case, as it would cause significant downtime on a production line to replace or unclog the nozzles. Clogging is a common challenge in cold spray for certain feedstock powders, namely in the case of materials with a low melting point [45]. It has been shown that materials such as aluminum and nickel can begin to clog a metallic nozzle in just a few minutes of continuous operation [46]. Even partial clogging can be an issue since it alters the cross-sectional profile within the nozzle, causing a reduction in cross-sectional area which reduces the gas velocity. This in turn reduces the particle velocity, which results in lower coating quality [47]. Research has been done in an effort to better understand this problem and ultimately mitigate it [45], [47]–[51], with potential solutions ranging from nozzle cooling [45] to a nozzle redesign with the use of non-metal materials [46].

In fact, the patent submitted by *Haynes et al.* [46] suggests that a nozzle made of polybenzimidazole, a high-performance thermoset polymer, would increase the continuous operation time of the process by reducing clogging. Technoform Bautec Ibérica, in collaboration with Centerline (Windsor) Ltd., began testing the performance of Centerline's UltiLife™ nozzle. The UltiLife™ line is an axisymmetric nozzle made of polybenzimidazole which helped mitigate the clogging issue seen with the metal nozzle previously tested.

With the clogging issue resolved, the two companies began working on improving the process for Technoform's specific application by optimizing process parameters and experimenting with different nozzle shapes. This research was therefore motivated by the search for a more efficient nozzle shape, which would create a more desirable coating for Technoform's commercial application.

2.2 COLD GAS DYNAMIC SPRAY

This subsection will introduce and examine the CGDS process and relevant gas dynamics principles. It will provide a general overview of past research related to the work performed as part of this thesis, as well as key concepts required to understand the relevancy and purpose of the work.

2.2.1 Background

Cold Gas Dynamic Spray (CGDS), also commonly referred to as cold spray, is an additive manufacturing method which is a part of the thermal spray processes. The history of cold spray can be traced back to the early 1900s, where Samuel Thurston patented a "Method of impacting one metal upon another" [52], where metal particles can be embedded in a metal substrate by accelerating them with a pressurized gas [53], [54].

In 1958, a patent was filed by Charles F. Rocheville which resembles the design of Thurston, but improves it by using a DeLaval converging-diverging nozzle to achieve higher, supersonic velocities [55]. Using this device, he was able to create uniform coatings over an entire surface. However, the powder particles were only embedded in the original surface and would not build upon each other, only creating a very thin layer [53].

In the 1980s, scientists from Novosibirsk, Russia filed two patents after studying interactions between two-phase flows and solid bodies [56], [57]. These documents outline a device and method in which powder particles are accelerated by a hot, high-pressure gas flow [56], [57]. The temperatures reached by the gas are well below the particle melting point, and the impact of the solid particles upon a substrate results in a thick, dense coating. In 1994, another method was patented [58]; the new process could not only be used with metal particles, but also polymers, alloys, and mixtures [53].

Modern cold spray systems are a result of these innovations. These modern systems use the DeLaval type nozzles to accelerate high-pressure, preheated gas to supersonic velocities using well-known gas dynamics principles. Micron-size particles are then injected either radially or axially into the flow to be accelerated and then projected onto a workpiece, generally to create a dense and well-adhered coating of a desired thickness. As with the process patented in the 1980s, and as opposed to conventional thermal spray

processes, the gas temperature at the powder inlet is kept below the melting point of the powder material. Therefore, particles do not undergo any melting prior to impact with the substrate. The process depends on many parameters, such as gas operating temperature and pressure, the gas nature, particle size, shape, and material, substrate material, and nozzle geometry [59].

2.2.2 Gas Dynamics Principles and Process Parameters

The CGDS process relies on gas dynamic principles to accelerate the gas in a converging-diverging nozzle and drag forces between the gas and particles to accelerate them before impact. Generally, the flow is considered to be one-dimensional, ideal, and isentropic so that an estimate of gas velocity, pressure, and temperature can be obtained along the length of the nozzle [60], [61]. Since the gas is accelerated to supersonic speeds, its velocity V_{gas} can be expressed as:

$$V_{gas} = M_a c \qquad \text{(Eq. 2.1)}$$

Where M_a is the local Mach number and c is the speed of sound.

In the case of an ideal gas, the equation for the speed of sound is given as [61], [62]:

$$c = \sqrt{kRT_{gas}} \qquad \text{(Eq. 2.2)}$$

Where k is the specific heat ratio of the gas, R is the specific gas constant, and T_{gas} is the temperature of the gas.

Therefore, the gas velocity relationship can be described as:

$$V_{gas} = M_a \sqrt{kRT_{gas}} \qquad \text{(Eq. 2.3)}$$

Using the previously stated assumptions, the following isentropic relations can be obtained for the gas conditions in the nozzle [61], [62]:

$$\frac{P_0}{P_{gas}} = \left(1 + \frac{k-1}{2} M_a^2\right)^{\frac{k}{k-1}} \quad \text{(Eq. 2.4)}$$

$$\frac{T_0}{T_{gas}} = 1 + \frac{k-1}{2} M_a^2 \quad \text{(Eq. 2.5)}$$

$$\frac{\rho_0}{\rho_{gas}} = \left(1 + \frac{k-1}{2} M_a^2\right)^{\frac{1}{k-1}} \quad \text{(Eq. 2.6)}$$

Where the subscript "0" denotes the stagnation conditions of the gas. It is also important to note that the local Mach number is a function of the gas specific heat ratio, k, and the cross-sectional area of the nozzle, A, as shown in the following relationship [60]:

$$\frac{A}{A^*} = \frac{1}{M_a}\left(\frac{2}{k+1} + \frac{k-1}{k+1} M_a^2\right)^{\frac{k+1}{2(k-1)}} \quad \text{(Eq. 2.7)}$$

Where A^* denotes the area at the throat of the nozzle, where the cross-sectional area is the smallest. Since A and A^* are set by the geometry of the nozzle and k is determined by the gas nature, it can be shown that for a specific gas the local Mach number Ma is set by the area ratio of the nozzle. If both Ma and k are fixed, Equation 2.4 – 2.6 show that the other local parameters of the flow are determined solely by the stagnation conditions.

Generally, the stagnation conditions that can be controlled for cold spray systems are the temperature and pressure. Equation 2.4 and 2.5 show that increasing the stagnation pressure or temperature will result in an overall higher pressure P_{gas} or temperature T_{gas} in the flow, respectively. The effect of a higher gas temperature is demonstrated in Equation 2.3, and will result in a higher achievable gas velocity. The effect of higher gas pressure can be shown by the ideal gas law, which can be written as:

$$P_{gas} = \rho_{gas} R T_{gas} \quad \text{(Eq. 2.8)}$$

As can be seen in Equation 2.8, higher gas pressure will result in higher gas density for a set temperature. Higher gas density will result in higher particle acceleration, and

potentially higher particle velocity, which will be demonstrated by Equation 2.14. However, there are practical limitations to consider regarding both pressure and temperature parameters.

High stagnation temperatures can cause multiple issues, such as substrate overheating [63], [64]. Since the gas flow must come to a stop as it hits the substrate, that surface experiences a steady-state temperature near the gas stagnation temperature as the kinetic energy is converted back to thermal energy. Another potential issue that can arise with high stagnation temperature is nozzle clogging [65], [66]. It has been hypothesized by *MacDonald et al.* that the effect of interactions between the particles and nozzle walls may be stronger as the stagnation temperature is increased [66]. The particle-wall interactions could cause smearing of the particles, increasing friction and reducing their velocity [66]. Limits on the stagnation temperature are also imposed by the commercially available cold spray systems [54].

In the case of stagnation pressure, there is also a maximum due to practical limitations. High pressure cold spray systems can reach a pressure of up to 6.89 MPa [67]. The pressure is generally limited to avoid issues with gas consumption and heater capacity [68]. An increase in pressure results in increased density, which in turn increases mass flow rate $\dot{m}$, as shown by the following relation:

$$\dot{m} = \rho_{gas} V_{gas} A \qquad \text{(Eq. 2.9)}$$

As such, if the pressure is too high, the heater might not be able to heat the gas to the desired temperature due to the increased flow rate.

Now that the laws governing the flow and the effect of stagnation parameters are understood, the interaction between gas and particles must be studied. The solid particles in the flow are affected by drag force, which is given by the following equation [61]:

$$F_D = \frac{1}{2} \rho_{gas} V_r^2 C_D A_p \qquad \text{(Eq. 2.10)}$$

Where V_r is the relative velocity between the gas and solid ($V_{gas} - V_p$), C_D is the drag coefficient, and A_p is the projected area of the solid perpendicular to the flow of the gas. The force applied by the drag upon a particle must be equal to Newton's second law of motion. Due to the low mass of the particles, and the velocities they reach during the process (on the order of hundreds of meters per second), gravitational forces are considered to be negligible, such that:

$$m_p a_p = \frac{1}{2}\rho_{gas} V_r^2 C_D A_p \qquad \text{(Eq. 2.11)}$$

Where m_p and a_p are the mass and acceleration of the particle, respectively. By replacing the relative velocity V_r by its definition ($V_{gas} - V_p$), and then substituting V_{gas} by the relationship shown in Equation 2.3:

$$m_p a_p = \frac{1}{2}\rho_{gas} \left(M_a \sqrt{kRT_{gas}} - V_p\right)^2 C_D A_p \qquad \text{(Eq. 2.12)}$$

Gas-atomized, spherical powders are a common occurrence in cold spray [69], [70], so it is a reasonable assumption to take a spherical powder particle in this case. The mass of a spherical solid is given by:

$$m_p = \frac{4}{3}\rho_p \left(\frac{d_p}{2}\right)^3 \qquad \text{(Eq. 2.13)}$$

Where ρ_p and d_p are the density and diameter of the spherical particle, respectively. Substituting m_p in Equation 2.12 by its definition from Equation 2.13 yields the following:

$$\frac{4}{3}\rho_p \left(\frac{d_p}{2}\right)^3 a_p = \frac{1}{2}\rho_{gas} \left(M_a \sqrt{kRT_{gas}} - V_p\right)^2 C_D A_p \qquad \text{(Eq. 2.14)}$$

From Equation 2.14, it is seen that multiple parameters will affect the resulting velocity of the particle, which are all function of the particle material (ρ_p), particle size and/or shape (d_p, C_D, A_p), gas nature (k), or process parameters (T_{gas} function of T_0).

It is well-known in the field of cold spray that irregularly shaped particles reach a higher velocity than spherical particles at the nozzle exit [71], [72]. It has also been known since the early days of cold spray that the gas nature has a significant impact on particle velocity, as shown by gas-dependant variable k and R in Equation 2.14 [68]. One of the desired characteristics of any propellant gas for use in cold spray is a low molar mass [73], since it greatly affects the specific gas constant as shown in Equation 2.15:

$$R = \frac{\overline{R}}{M} \quad \text{(Eq. 2.15)}$$

Where $\overline{R}$ is the universal gas constant ($8.3145\ kJ/kmol \cdot K$) and M is the molar mass of the gas. The molar mass also relates to the specific heat ratio through the following equations:

$$k = \frac{C_p}{C_v} \quad \text{(Eq. 2.16)}$$

Where C_p is the heat capacity at constant pressure, and C_V is the heat capacity at constant volume. And:

$$R = C_p - C_v \quad \text{(Eq. 2.17)}$$

Thus, a lower molar mass will result in a higher specific gas constant, as well as higher specific heat ratio. As demonstrated by Equation 2.3, for a set local Mach number M_a and gas temperature T_{gas}, a gas with lower molar mass will reach higher velocities within the nozzle.

Monoatomic gasses typically have a specific heat ratio around 1.67, whereas diatomic gasses are approximately 1.4 [60]. Helium, nitrogen, and dry air are viable propellant gasses for CGDS as they are non-toxic, and neither inflammable or explosive [73]. Helium ($k = 1.67, R = 2080\ J/kg \cdot K$) is significantly more expensive, but consistently provides much higher velocities than dry air and nitrogen ($k = 1.4, R = 287\ J/kg \cdot K$ and $k = 1.4, R = 297\ J/kg \cdot K$, respectively) [58], [68].

Other parameters to consider in cold spray include traverse speed, standoff distance, and powder feed rate. Traverse speed refers to the translational velocity of the gun on a 2D plane parallel to the substrate (or vice versa, velocity of the substrate if the gun is stationary). Traverse speed affects total spray time, as well as coating thickness. When the traverse speed is reduced, the overall spray time to cover the full surface of the substrate increases. This also causes the nozzle to spend more time above a certain unit area, resulting in more particle impacts in said area when compared to higher traverse speeds. Reducing the traverse speed also exposes the surface of the substrate/coating to the hot stagnation gas temperature for increasing periods of time, resulting in increased local heating of the surface. This has been shown to affect deposition by *Fukumoto et al.* [74].

Standoff distance is the perpendicular length between the substrate surface plane and the nozzle exit prior to the start of the spray. Studies have shown that the standoff distance can affect the particle impact velocity and deposition efficiency [18], [19]. When the standoff distance is very short, the bow shock is more pronounced as the supersonic gas flow cannot be slowed by the ambient air before impacting the substrate. This can significantly affect the particle velocity before impact, depending on particle mass and shape. As the standoff distance is increased, the bow shock is less pronounced. However, the gas flow, and subsequently the particles it carries, can be slowed by friction with the ambient air outside of the nozzle which is stagnant [18], [19].

Increasing the powder feed rate has been shown to linearly increase coating thickness [75]. This rule applies until a limit is reached, where too many particles impact the substrate per unit area, in which case the coating thickness and quality begins to degrade. Excessive bombardment of the substrate/coating occurs when exceeding this powder flow rate limit, which results in strong residual stresses that cause the coating to delaminate. This can be remedied by reducing the feed rate, or increasing the gun traverse speed to reduce particle impacts per unit area [75].

Finally, it should be noted that while the one-dimensional isentropic model is a reasonable approximation to use, the gas dynamic equations derived in this section and the conclusions drawn from them heavily rely on the assumptions from this one-dimensional approach [60], [61]. In a study performed by *Jodoin*, a two-dimensional model was used and compared to

the one-dimensional approach [17]. The results reinforced that stagnation temperature is an important factor in cold spray, due to particles being exposed to this temperature between the bow shock and substrate just before impact. The model shows that the heat transfer between the gas flow and ambient air is minimal, and the stagnation temperature at the substrate surface is nearly the same as the process stagnation temperature [17]. This two-dimensional model has also revealed that particle-shockwave interactions have a noticeable effect on particle impact velocity. Figure 2.1 shows the change in velocity caused by the formation of the bow shock in front of the substrate surface, which will affect the impact velocity of the particles. Due to these factors, nozzles for cold spray should be designed to attain a Mach number between 1.5 and 3 at the exit plane, in an effort to limit the negative impacts of high stagnation temperature and interactions between the bow shock and particle impact velocity [17].

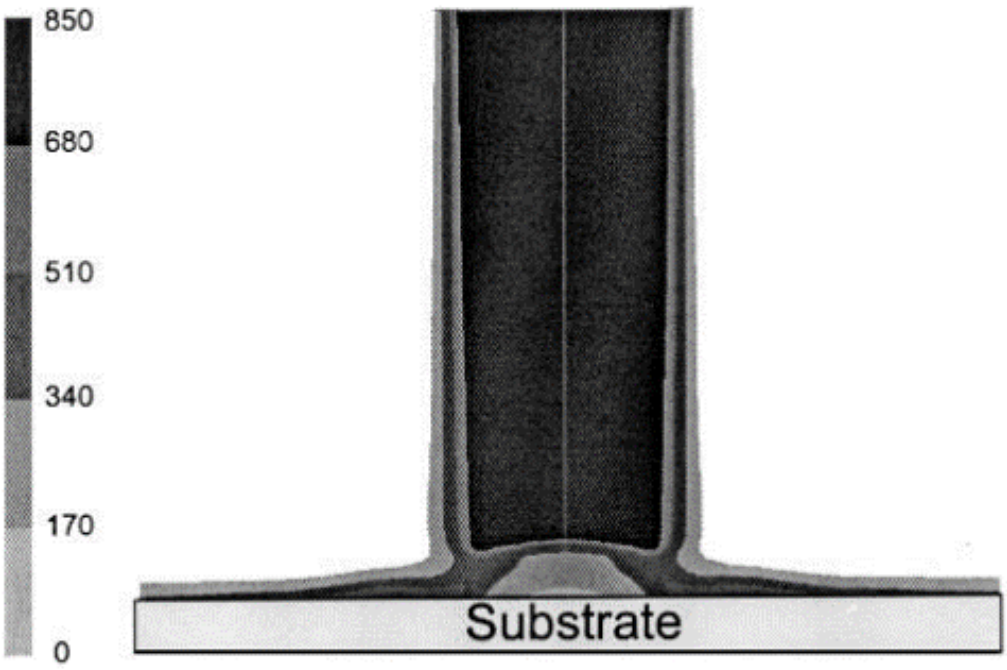

Figure 2.1 – Velocity field of gas jet impacting a substrate, demonstrating the bow shock occurring in front of the surface [17] (© 2001 Springer Nature)

2.2.3 Adhesion Mechanism

Adhesion in cold spray is typically the result of one of two mechanisms, or a combination of them. These mechanisms are usually referred to as mechanical bonding, and metallic bonding [76]–[78]. Bonding is a result of local particle deformation during impact, which requires an impact velocity threshold to be surpassed, called the critical velocity [59], [60]. Critical velocity will be further discussed in Section 2.2.4, but it is dependant on particle and substrate materials, as well as temperatures at the moment of impact [59], [60].

In the case of mechanical bonding, particle/substrate or particle/particle impact results in mixing and interlocking between the two. This requires high contact pressure to create significant deformation during impact [79]. The mixing occurring at the impact site is a result of adiabatic softening, which is the effect of a phenomenon called adiabatic shear instability [80]. This phenomenon occurs when the material is subjected to extremely high strain rates. In simulations performed by *Schmidt et al.*, it was shown that a 10 µm copper particle impacting at 600 m/s can experience maximum strain rates of up to 10^9 s^{-1} [59]. The mechanical properties of many metals are strain rate sensitive at such extreme strain rates [81], [82]. Due to the short time scale of particle impacts, on the order of nanoseconds in cold spray, the heat generated by the deformation cannot be transferred out of the particle. The adiabatic nature of the impact causes the particle to heat up, resulting in softening of the material despite the significant deformation [77], [79], [80]. The combination of these factors allows the two impacting surfaces to flow, resulting in the 'jetting' phenomenon, where material is ejected from the impact site at the periphery of the particle. Figure 2.2 shows the jetting process during impact, as seen in simulations and experimentally.

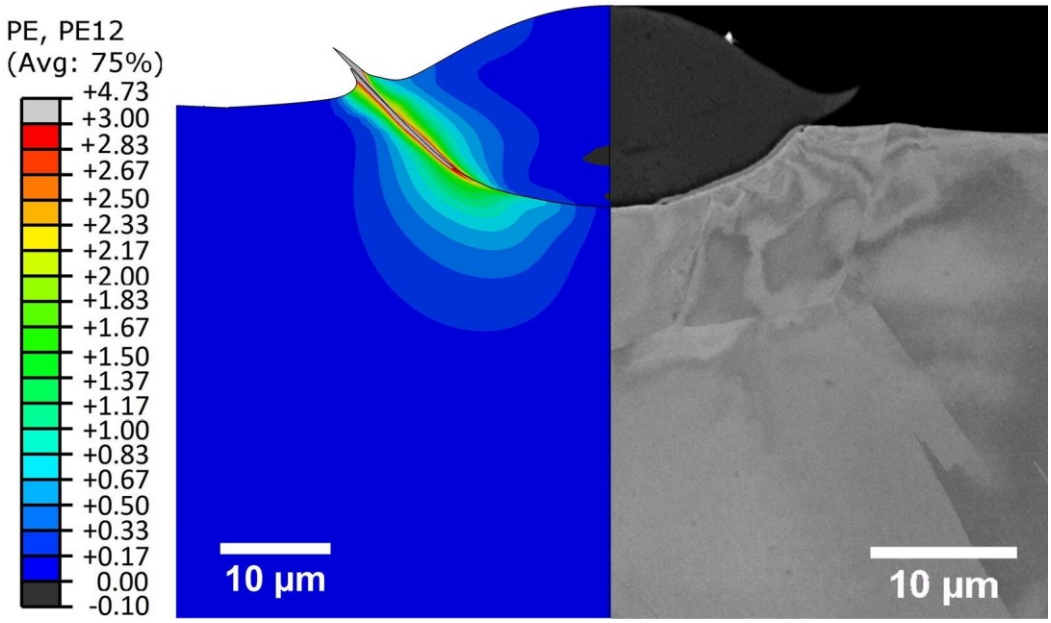

Figure 2.2 – Cross-sectional view of particle impact and jetting, as seen through computational (left) and experimental (right) results [83] (© 2018 Elsevier)

In the case of metals, the jetting of material effectively cleans both surfaces of oxides, resulting in intimate metal to metal contact, promoting the formation of metallic bonds (sometimes also referred to as metallurgical bonding) [79]. Figure 2.3 shows local metallic bonding sites in an etched Ti-6Al-4V coating as a result of direct metal to metal contact between titanium particles.

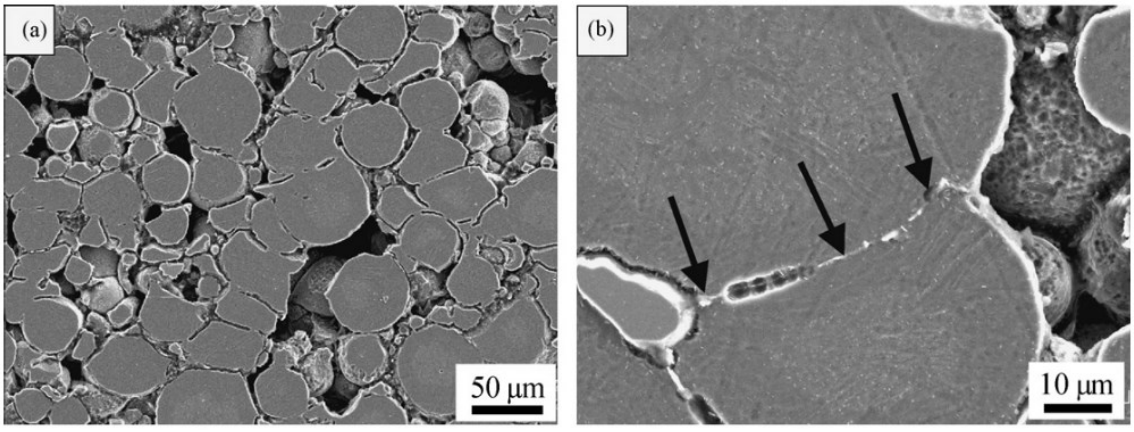

Figure 2.3 – High magnification SEM image of a Ti-6Al-4V coating deposited on mild steel, as seen after etching of the sample. The arrows in (b) point to the metallic bonding locations between Ti particles in the coating [84] **(© 2007 Elsevier)**

Many surface preparation methods can be utilized with the aim of creating sites for mechanical anchoring or to clean the substrate surface [34]. Such methods include, but are not limited to, grinding, polishing, grit blasting, and pulsed water jetting [34], [35], [85]. By increasing the surface roughness of the substrate, the bond strength is generally increased due to an increase in mechanical bonding [34], [77]. An example of mechanical interlocking between a copper coating and aluminum substrate is shown in Figure 2.4. It has been suggested that mechanical interlocking is the main adhesion mechanism in cold spraying, much like other thermal spraying processes [84]. However, in some cases where metallic bonding is dominant, surface preparation such as grit blasting can in fact reduce the bond strength due to a reduction in viable metallic bonding sites [21], [34].

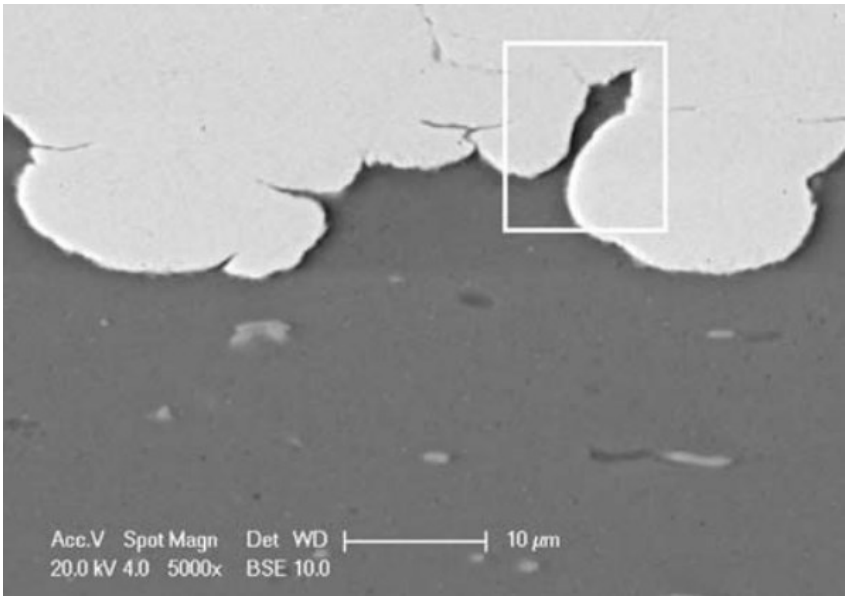

Figure 2.4 – High magnification image of copper sprayed on aluminum, showing a site of mechanical bonding or "interlocking" between both materials [77] (© 2009 Springer Link)

2.2.4 Critical Velocity

As previously mentioned, to obtain phenomena such as adiabatic shear instability and jetting at the impact site, extreme strain rates are required which can only be achieved by particles exceeding a certain velocity threshold, nicknamed the critical velocity. The critical velocity is dependant on multiple factors; the particle material, the particle temperature at impact, particle size and geometry, and the material of the surface being

impacted (substrate or particle) [59], [60]. It is well-known that larger particles will attain lower in-flight velocities due to their increased mass, so the velocity of the largest particle that adheres to the substrate is considered as the critical velocity for bonding [59], [78]. However, particles that are smaller than 10 µm are severely affected by the bow shock, and their impact velocity is subsequently reduced. *Schmidt et al.* have determined that the optimal size range to minimize the difference between in-flight velocity and impact velocity, which should be maintained above the critical velocity, is between 10 and 45 µm [59]. Figure 2.5 shows the theoretical critical impact velocity of a variety of powder materials, given a 25 µm particle size. The dark portion seen in each band represents the uncertainty of the theoretical result due to available materials data. Experimentally, a laser system can be used to measure particle velocities. By altering process parameters to obtain deposition, and measuring the particle velocities, the average critical velocity can be determined [86], [87].

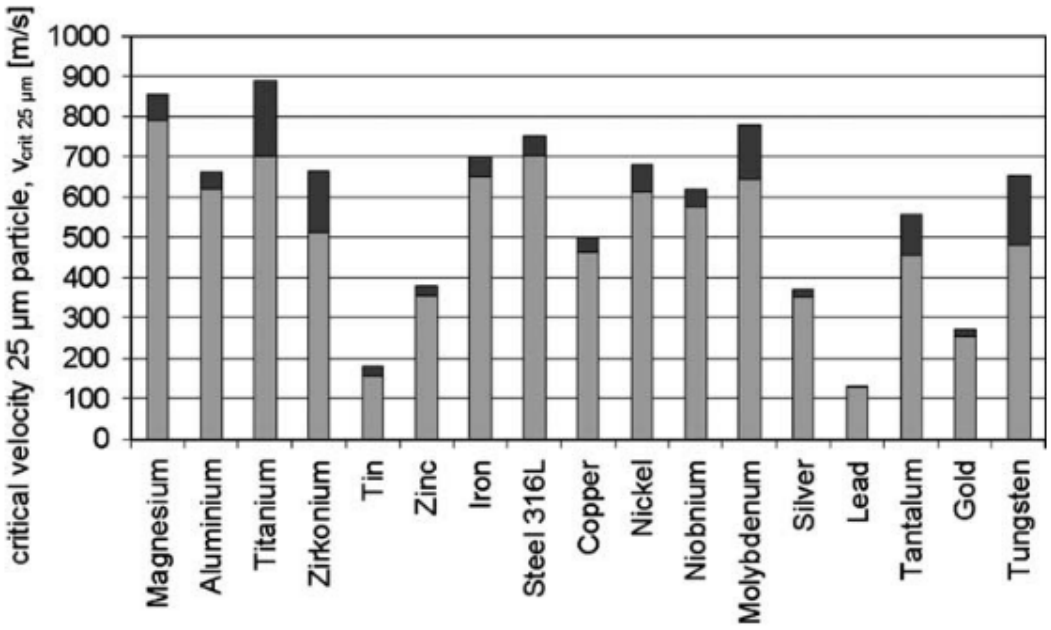

Figure 2.5 – Theoretical critical impact velocity of a 25 µm particle for different materials. The dark grey area indicates the range of uncertainty considering available materials data [59] (© 2005 Elsevier)

Below the critical velocity, particles lack enough energy to deform significantly on impact and displace the oxide layer to create clean metal to metal contact [76]. Particles at these velocities will typically rebound and fail to create a coating buildup. Once the critical

velocity is reached, the deposition efficiency (further explained in Section 2.2.5) can increase significantly. However, if the velocity is increased further beyond a certain threshold, the deposition efficiency will start to decrease as the particles begin to erode the surface instead of adhering to it [59], [88]. Therefore, while critical velocity is an important metric, the so-called deposition window should be considered, as approaching the erosion velocity will result in decreased coating quality (if any) and deposition efficiency [78]. Figure 2.6 shows the deposition window for a ductile particle with a given size and impact temperature and demonstrates the concept of critical velocity and erosion velocity, where deposition efficiency increases or decreases, respectively. In the case of a brittle material, no deposition window is observed.

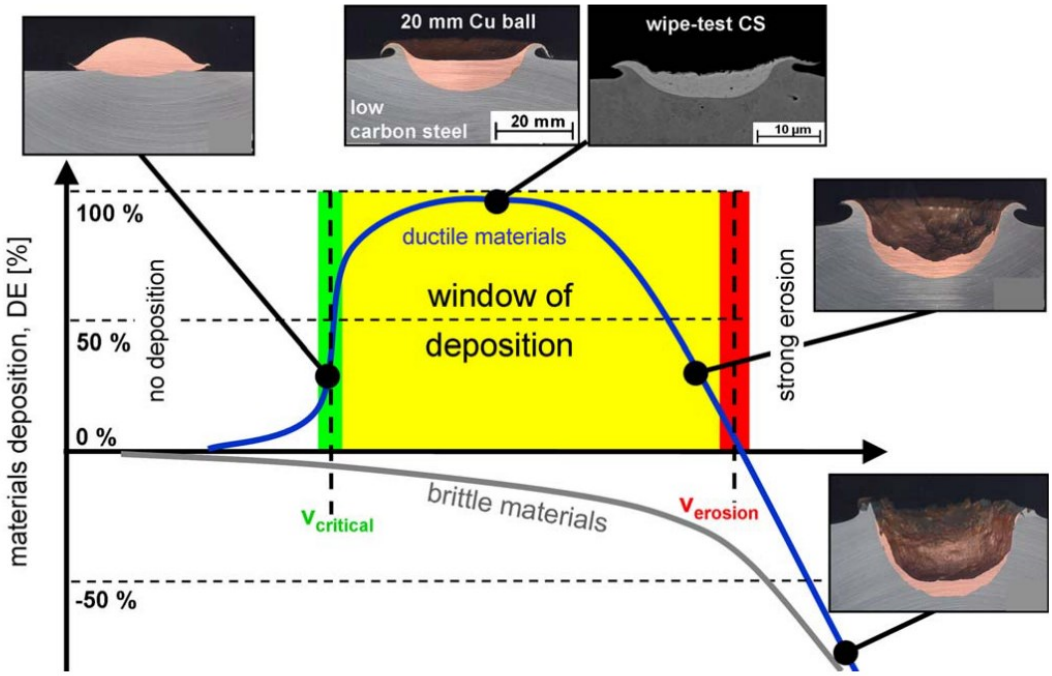

Figure 2.6 – Schematic demonstrating the "deposition window", for a set temperature and particle size, where DE increases significantly for ductile materials when reaching the critical velocity [78] (© 2009 Springer Nature)

It is important to note that the critical velocity exists for ductile materials, however, brittle materials will erode metal substrates at any velocity [78]. Also, since the critical velocity is affected by the materials used, it will differ for particle-substrate collisions compared to particle-particle collisions [84].

2.2.5 Deposition Efficiency (DE)

Deposition efficiency is an important metric to determine how much of the sprayed powder adhered to the substrate. It is determined by taking the weight gain of the substrate, and dividing it by the product of the mass feed rate and spray time over the substrate, such that [87]:

$$DE\ (\%) = \frac{weight\ increase\ of\ susbtrate\ (kg)}{mass\ feed\ rate\ (kg/s) \cdot spray\ time\ on\ substrate\ (s)} \qquad \text{(Eq. 2.18)}$$

DE is known to be a function of particle material, substrate material, and particle impact velocity [87], [89], [90]. It has also been shown that in low-pressure cold spray, the nozzle material affects the DE. It was hypothesized that nozzle materials with higher thermal diffusivity would transfer more heat to particles during nozzle-wall interactions [66]. Higher particle temperature is known to lower critical velocity in many cases, which results in increased DE [59], [60], [66].

Previously mentioned surface preparations techniques can be utilized not only to affect adhesion, but also deposition efficiency. The surface roughness created by grit blasting the substrate prior to spraying can influence the DE of the first few layers [33]. Other parameters known to influence the DE are particle preheating as well as substrate preheating. In both cases, the goal is to utilize thermal softening to improve deformation of either the particle or substrate during impact, improving with deposition [63], [74], [91].

It should be noted that DE is not a metric of coating quality, but rather a ratio of deposited vs. non-deposited powder. Spray parameters that resulted in high deposition efficiency could still create a coating with pores, weak adhesion, and/or poor mechanical properties for the desired application [78]. Figure 2.7 shows how DE generally increases with increasing particle velocity for different ductile materials (aluminum, copper, and nickel) even when using different propellant gases.

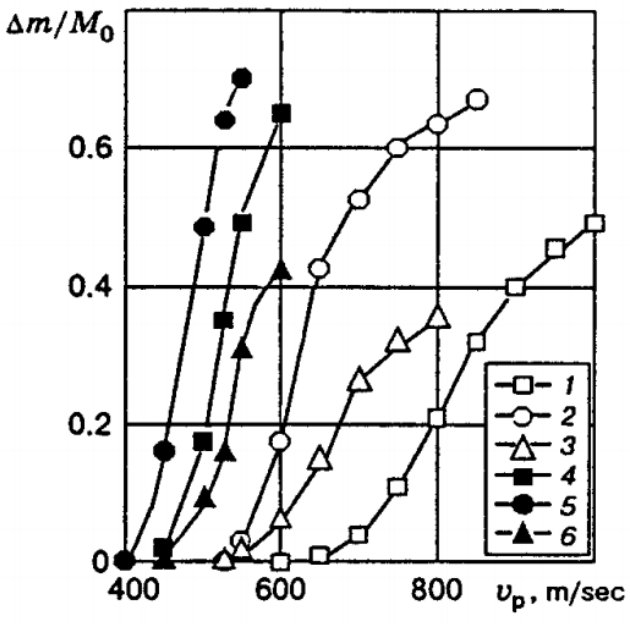

Figure 2.7 – Deposition efficiency vs. particle velocity for different materials; 1) aluminum, 2) copper, 3) nickel, deposited using an air-helium mixture at room temperature; 4) aluminum, 5) copper, 6) nickel, deposited using hot air ($\Delta T \leq 400$ K) [92] **(©1998 Springer Nature)**

2.3 NOZZLE MATERIALS AND MANUFACTURING

This subsection of the literature review reports current materials and manufacturing techniques utilized to produce nozzles in cold spray. However, as there is little information in the literature on this specific topic, this section will mostly present general information about manufacturing, with the CGDS-specific use of these techniques and materials supported by literature when possible.

2.3.1 Materials

The commercially available SST Series EP cold spray system from Centerline (Windsor) Ltd. (further detailed in Section 4.3 of this document) used in the University of Ottawa Cold Spray Lab is compatible with Centerline's UltiLife™ and UltiFlow™ modular nozzle systems. This system uses a converging section made of metal with an interchangeable diverging nozzle to form a complete converging-diverging setup.

The SST-UltiFlow nozzle is made of polybenzimidazole (PBI), also called Celazole®, which is utilized in this application due to its ability to withstand high operating

temperatures without clogging. *MacDonald et al.* have shown that eventual clogging occurs in low pressure cold spray for all tested nozzle materials (C110 copper, 304 stainless steel, glass-mica ceramic) during extended use, except in the polybenzimidazole polymer nozzle [66]. The SST-UltiLife nozzle is made from Tungsten carbide (WC), due to its hardness which allows for a longer operating life cycle and its ability to withstand high temperatures.

Metallic nozzles compatible with the SST Series EP system are also available, such as stainless-steel (SS) nozzles. While SS nozzles were not utilized in this work, it is worth mentioning them as they are not manufactured using the same process as the UltiLife™ and UltiFlow™ nozzles.

2.3.2 Manufacturing Techniques

Following are some manufacturing techniques that can be used to manufacture cold spray nozzles from the materials discussed in Section 2.3.1., depending on the nozzle geometry.

2.3.2.1 Hydroforming

Tube hydroforming can be used to form tubes or complex hollow parts. The metal tubing is initially manufactured in a die, then the interior is pressurized by a fluid such as water to form the desired shape through plastic deformation of the tubing [93].

In Centerline (Windsor) Limited's case, hydroforming is used to form the diverging part of the modular system in the case of SS nozzles. This produces a smooth gradient from the throat to the exit of the nozzle as the metal is "stretched" instead of machined. Figure 2.8 shows a schematic drawing of the SS nozzle cross-section.

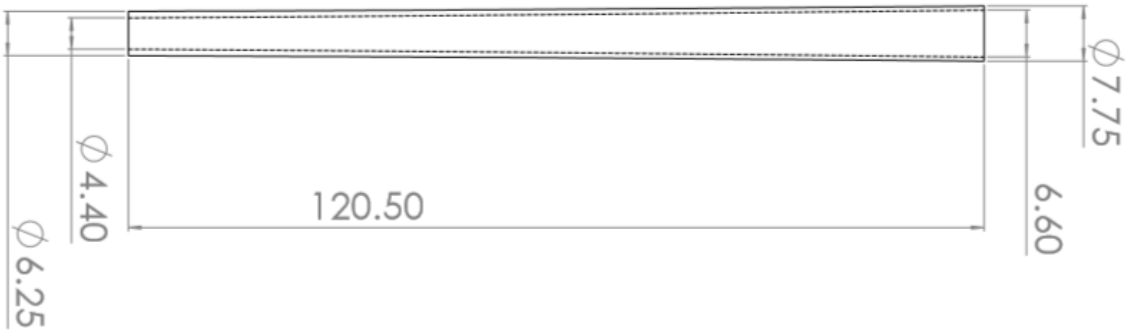

Figure 2.8 – Stainless steel nozzle profile

2.3.2.2 Powder Metallurgy

Powder metallurgy is a general term used to define the fabrication of objects from metallic powders. In the case of the UltiLife diverging nozzle from Centerline (Windsor) Ltd., the part is made of cemented carbides. Cemented carbides are made from hard particles, in this case WC, which is then mixed with a smaller amount of metal binder. For WC-based cemented carbides, the binder used is usually cobalt (Co) with a mixture of up to 20% Co by weight [94], [95].

Multiple manufacturing steps are required in order to produce the desired part. Figure 2.9 shows some general steps used in the production of a cemented carbide cutting tool [96]. Initially, the raw materials are turned into powders before the carbide and binder are weighed and mixed. After being milled to get a homogenous slurry, the powders are dried, and the blend composition is verified before compaction [96]. Depending on the geometry of the final part, the compaction process is done using either uniaxial die pressing, cold isostatic pressing, or extrusion [94]. Soft machining can be performed depending on the geometry, and then the green is sintered to create interparticle bonds which strengthen and densify the part [97]. Finally, the hardened part can be machined to exact dimensions as required [96].

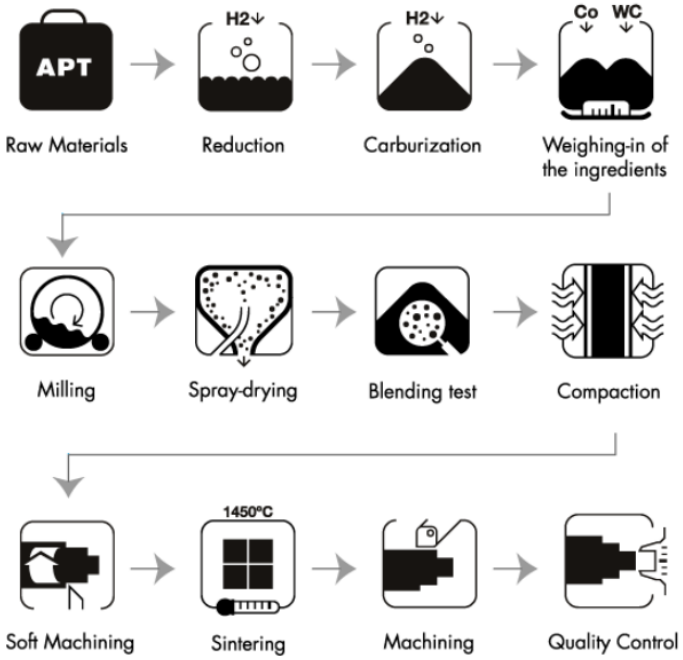

Figure 2.9 - Overview of cemented carbide manufacturing steps [96] **(© 2020 Hyperion Materials & Technologies Inc.)**

2.3.2.3 Machining

Machining is a subtractive manufacturing process, where excess material is removed from a raw or pre-shaped object to bring it down to the appropriate size and/or shape. Machining processes can be classified into a few categories; machining through cutting, abrasion, erosion, combined machining, and micromachining [98].

In the case of the PBI nozzle manufacturing, the relevant processes are part of the cutting family. The first process of interest is drilling, as the inside nozzle profile can be created by drilling from the nozzle exit using different drill sizes. Figure 2.10 shows an engineering drawing of the PBI polymer nozzle cross-section, where different drill sizes have been used at different depths to create a diverging shape within the nozzle. However, the drilling process is a rough operation with poor accuracy, and the surface finish is rough due to chipping during the drilling operation, drill feed marks, and drill taper [98]. Following the drilling operation, the inner surface can be improved through a finishing process such as reaming, which provides a much smoother surface finish while also being more dimensionally accurate than drilling [98], [99].

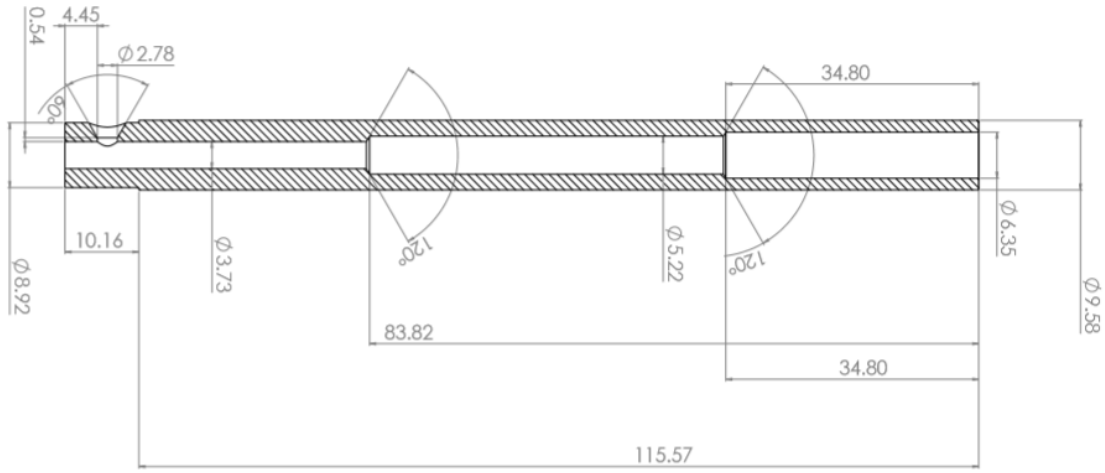

Figure 2.10 – Cross-section of PBI nozzle profile

3 RESEARCH OBJECTIVES

3.1 GENERAL OBJECTIVES

The aim of the industrial partner is to use CGDS to metallize extruded polymer profiles for use in thermal break window insulation. The metallization of polymer materials using CGDS has already been investigated [37]–[39], [100]–[103] and the industrial partner has shown that aluminum can successfully be deposited on their polyamide substrate. Therefore, the overall goal of this study is not to show the feasibility of metallizing the substrate, but rather to improve the uniformity of the coating through improved nozzle design in an effort to improve the cost effectiveness of their CGDS production line. This is done mainly by increasing the width of the coating produced by each nozzle, which in turn reduces the number of nozzles needed to metallize the surface of the extruded polymer profile in a single pass. This has a cascading effect as less cold spray equipment will be needed for each production line, such as nozzle assemblies, heaters, and powder feeders.

To achieve this main objective, the intermediary goals were to:

a. Simulate the two-phase flow inside the nozzle (gas and particles);
b. Use the simulation data to create a prototype iterating on the initial obround design, while simultaneously utilizing better materials for spraying aluminum powder;
c. Showing that the prototype nozzle works and improves on the original obround design to provide a wider coating of consistent thickness;
d. Producing satisfactory single-track coatings on the extruded polymer substrate provided by the industrial partner.

3.2 CFD MODELLING

In order to modify and improve the obround design provided by the industrial partner, CFD modelling was performed to study the characteristics of the flow within the nozzle. The goal of the model was to study the particle-gas and particle-wall interactions, which are of

particular interest when determining how to improve the particle distribution and positioning at the nozzle exit.

3.3 PROTOTYPING

The next objective was to create a prototype nozzle based on the data collected from the model, to iterate on the design initially provided by the industrial partner. This new prototype was to be constructed from PBI polymer as opposed to WC, so further modifications had to be made to accommodate the change in material and manufacturing methods available.

3.4 PROOF OF CONCEPT

Once the prototype nozzle was acquired, it was necessary to first ensure it could work with the nozzle assembly and could handle the pressure and temperature required during spray. Then, single-track coatings were produced on aluminum substrates. The goal was to prove that new design can produce wide coatings, and to evaluate if any further design changes should be considered.

3.5 PRODUCTION OF SINGLE-PASS COATINGS ON POLYMER SUBSTRATE

Following any design changes, the final objective was to use the prototype PBI nozzle to produce single-track coatings on the industrial partner's polymer material. The goal was to show that the design modifications have improved the coating, making it wider and flatter when compared to the initial obround WC prototype nozzle.

4 EXPERIMENTAL DETAILS

4.1 FEEDSTOCK MATERIAL

The feedstock material used for all tests is the commercially available SST-A5001 pure aluminum powder (Centerline (Windsor) Limited, Windsor, Ontario). This powder is gas-atomized and composed of irregularly shaped particles, as shown in Figure 4.1a, with an average size of approximately 26 µm. The complete size distribution is shown in Figure 4.1b. This powder was selected for this research as it is used by Technoform for their industrial application.

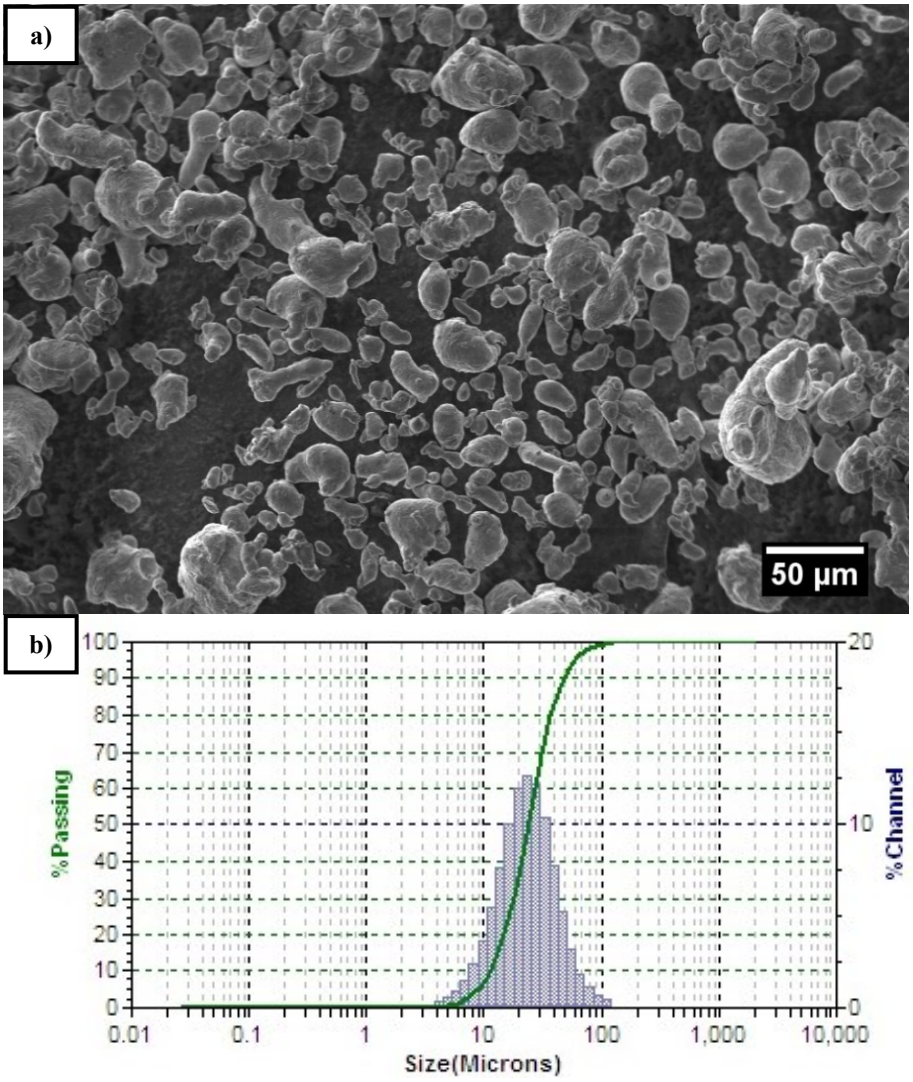

Figure 4.1 – SST A5001 pure aluminum powder from Centerline (Windsor) Ltd. a) SEM image of the powder, and b) size distribution of the powder

4.2 SUBSTRATES

Two materials were used as substrates in this study, an aluminum alloy and the polymer substrate used by the industrial partner.

Aluminum 6061-T6 was used initially with the original WC prototype to validate the computational model, and subsequently during the proof of concept stage to test the prototype PBI nozzle. It was chosen due to its availability and low cost, and for the abundance of literature on deposition for aluminum and its alloys [104]–[109]. Another advantage is that the DE for aluminum on aluminum deposition is higher than for aluminum on polymer. The coating is therefore easy to visualize, and powder waste is also reduced. The substrates, with an example shown in Figure 4.2, were 10 mm by 5 mm in size with a thickness of 3.175 mm (1/8”). The surface was either kept it its as-received state, or prepared by grinding it with 120 grit sandpaper. The surface was cleaned with ethanol prior to spraying.

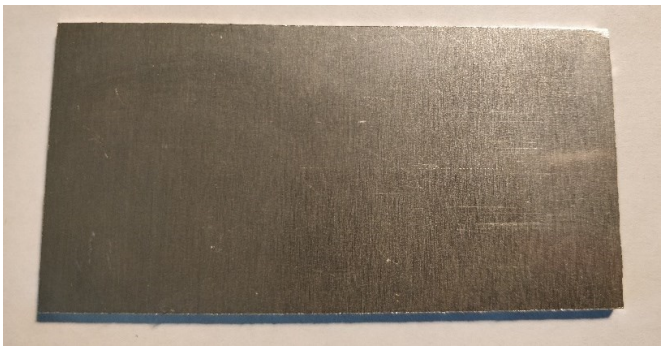

Figure 4.2 – Aluminum 6061-T6 substrate, as-received surface

The polymer substrate was provided by the industrial partner. The extruded pieces received were 21.25 mm in length, with a width of 3.25 mm and a maximum thickness of 1.4 mm as shown in Figure 4.3. The surface finish was unaltered and kept as-received to replicate the desired conditions. All substrates were cleaned with ethanol prior to spraying.

Figure 4.3 – Extruded Technoform polymer sample, as-received

4.3 CGDS SYSTEM

The commercially available SST Series EP cold spray system from Centerline (Windsor) Ltd. available at the University of Ottawa Cold Spray Lab was used for all experimental testing. Below are some details on essential components of this system.

4.3.1 Heater and Control Cabinet

The SST Series EP system is able to reach a maximum stagnation temperature of 650°C using a 15kW heater and can handle stagnation pressure of up to 3.45 MPa (500 psi).

The stagnation parameters can be set and monitored on a control cabinet, located beside the spray chamber. The desired process temperature can be set in increments of 25°C using the touchscreen, and the pressure is controlled via a regulator. The temperature and pressure sensors of the system are calibrated weekly using the calibration kit from Centerline (Windsor) Limited.

4.3.2 CGDS X-Y Traverse System

The movement of the gun is automated using a motorized, robotic traverse system. The gun's displacement, velocity, and acceleration on an X-Y plane can be programmed in assembly code. The system is limited by a traverse speed of 200 mm/s.

4.3.3 Nozzle Assembly

Two variations of the nozzle assembly were used in this research, the commercial version available from Centerline (Windsor) Ltd., and a modified dual injection variant. This variant was produced at our request, specifically for this research. Sections 4.3.3.1 and 4.3.3.2 describe both systems and their components.

4.3.3.1 Commercial System

The nozzle assembly utilized in this work consists of multiple detachable pieces and is part of the UltiLife™/UltiFlow™ lines of products, which are commercially produced by Centerline (Windsor) Ltd. (Windsor, ON, Canada). The parts are referred to as the nozzle holder, nozzle holder insert, powder feeding insert, and nozzle. A picture of the full assembly, including labels for each part, is shown in Figure 4.4.

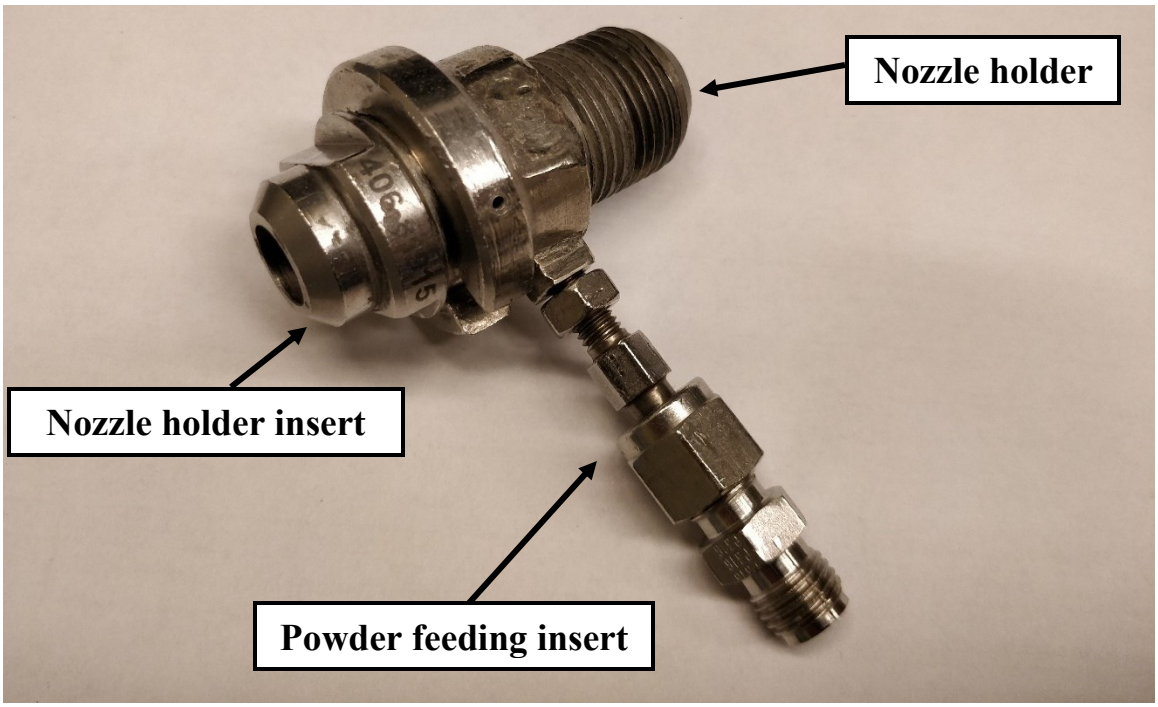

Figure 4.4 – Complete CGDS nozzle assembly

The nozzle holder contains the converging part of the main channel flow with a throat diameter of 2 mm. The threaded part of the holder screws into the CDGS gas heater to complete the CGDS system. The nozzle holder has a dedicated slot to align the powder feeding insert, and an inner ring to ensure the nozzle is properly aligned with the incoming gas flow. The nozzle holder is shown in Figure 4.5.

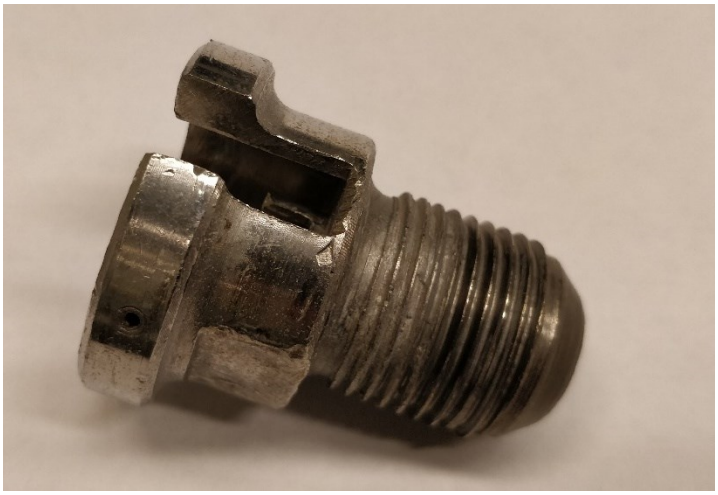

Figure 4.5 – Nozzle holder

The powder feeding insert is secured directly to the nozzle via a screw mechanism, with an additional nut to tighten the assembly. This insert, along with the nozzle, then slides firmly into place in the nozzle holder. To secure the full nozzle assembly, a spring and the nozzle holder insert are pushed along the length of nozzle. As the nozzle holder insert is turned and locked into place, the spring is compressed against it and the powder feeding insert, securing the nozzle into place. The two holders and the spring are shown in Figure 4.6.

Figure 4.6 – Powder feeding insert, spring, and nozzle holder insert

Commercially, this assembly system is paired with UltiLife™ or UltiFlow™ diverging nozzles. For reference, these commercial nozzles are 120 mm in length, with an inlet diameter of 3.7 mm and outlet diameter of 6.3 mm.

4.3.3.2 Dual Injection Variant

Due to the direction of this work towards a dual injection nozzle, the nozzle holder assembly had to be modified, along with the powder feeding insert, to accommodate these design changes. Centerline (Windsor) Ltd. designed and provided a dual injection variant to be used for this study. The dimensions of the parts remain the same as in the commercial variant. However, the nozzle holder has dual slots opposite to each other as opposed to the single slot, and the powder feeding inlet also has two inlet channels facing each other. Both pieces are shown in Figure 4.7.

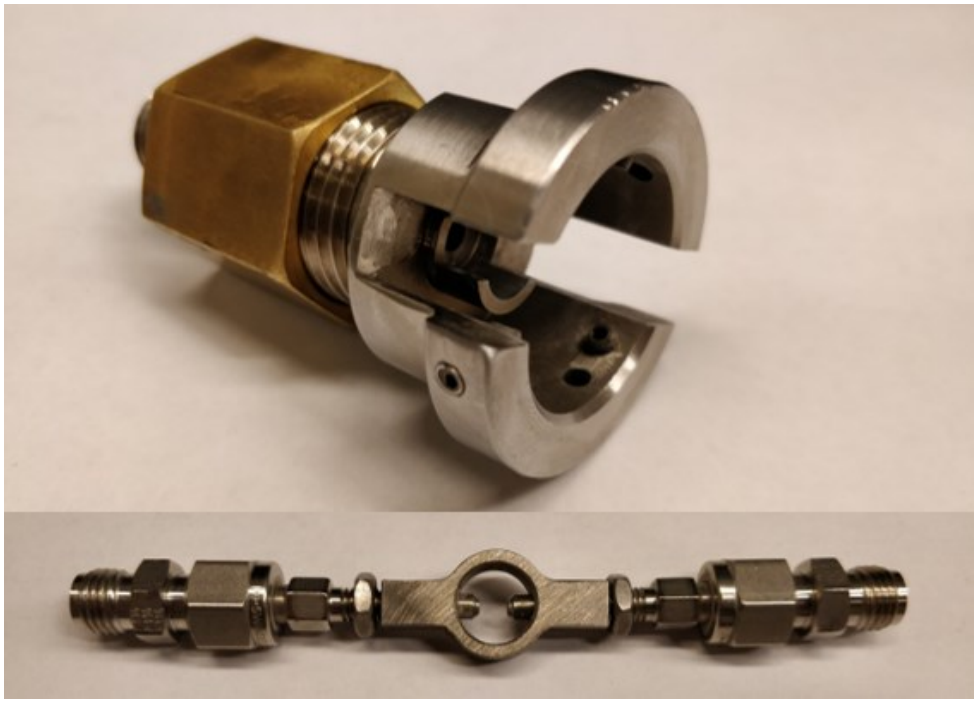

Figure 4.7 – Dual injection variants of the nozzle holder (top) and powder feeding insert (bottom)

This assembly was used in conjunction with the PBI obround prototype designed as part of this work. The obround prototype used is shown in Figure 5.20.

4.3.4 Powder Feeding Equipment

Two powder feeders were used in this study, as a second feeder was required when using the dual injection prototype. The powder feeder specifications are shown in the following subsections.

4.3.4.1 Primary Powder Feeder

The powder feeding system used to feed particles to the cold spray system is the AT-1200 HP, which is commercially available through Thermac Inc. (Appleton, Wisconsin, United States of America). This feeding system was dubbed the Primary Powder Feeder (PPF) as it was used for the single injection sprays early on, as well as for the dual injection sprays. It also served as the reference when measuring powder feed rates. Figure 4.8 shows the Thermac powder feeding unit, excluding the pressure canister which is mounted on the back of the unit. Refer to Figure 4.10 for pressure vessel location.

Figure 4.8 – Primary powder feeder unit, without pressure vessel

The feedstock is deposited in a pressure vessel with a perforated metal wheel at the bottom. Behind the wheel is a hole leading to a ball valve, which is connected to a tube going directly to the powder inlet on the nozzle. To deliver the feedstock to the main flow, the canister is pressurized, using nitrogen in this case, through an inlet on the side of the canister. The flow rate of the nitrogen is measured through a flowmeter with Standard Cubic Feet per Hour (SCFH) readings, and a digital pressure sensor is attached at the inlet of the canister to monitor the pressure inside. In this work, the canister was pressurized to approximately 69 kPa (10 psi) gauge pressure.

With the canister pressurized, the flow of powder is controlled by the perforated wheel. The powder is fed through the hole behind as a result of the rotating wheel and helped by the periodic tapping of the hammer attached to it. The feed rate can be adjusted by changing the speed of the wheel, as the powder feeder allows for a revolution-per-minute (RPM) input to be provided by the user. Different perforations sizes are also available for the wheel, which affects the number of holes and the feed rate. In this study, the small wheel

(320 holes) was used to feed the aluminum powder. As a comparison, the medium and large wheels have 240 and 120 holes, respectively. The small wheel is shown in Figure 4.9.

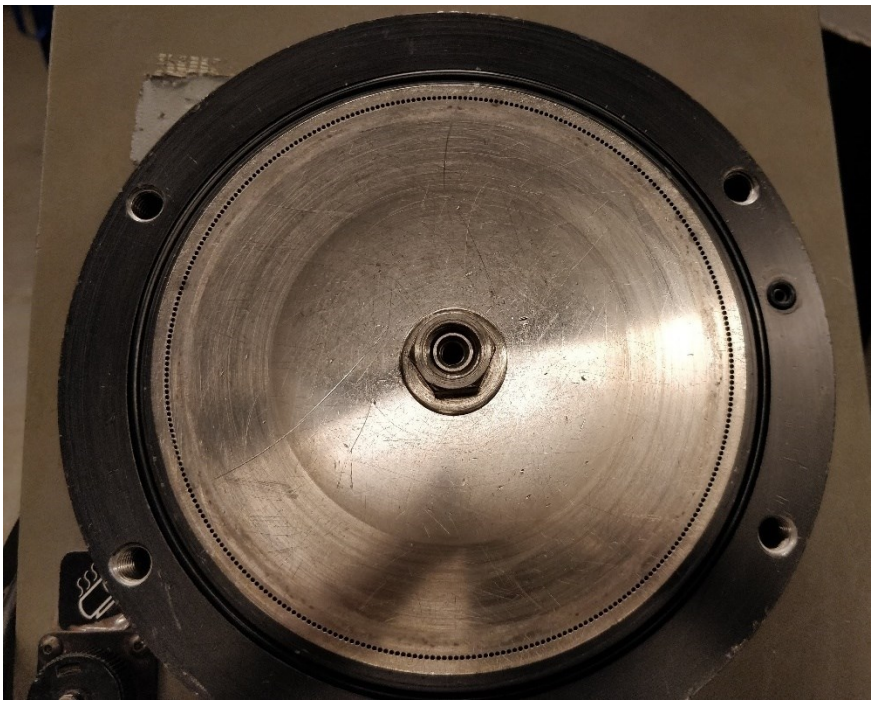

Figure 4.9 – Small perforated wheel (320 holes)

4.3.4.2 Secondary Powder Feeder

The secondary powder feeding unit is identical to the primary unit, the AT-1200 HP available commercially through Thermac Inc. (Appleton, Wisconsin, United States of America). This feeding system is referred to as the Secondary Powder Feeder (SPF) as it was only used for the dual injection sprays, and the feed rate was adjusted to match the reference feeding rate obtained from the primary powder feeder measurements.

The nitrogen flow rate is measured through a flowmeter, the same model as for the PPF, with SCFH readings. A digital pressure sensor is also attached to measure the pressure inside the canister. Like the PPF, the SPF's canister was pressurized to approximately 69 kPa (10 psi) gauge pressure during sprays. Figure 4.10 shows the feeding unit with the pressure canister attached, along with an alternate view showing the closed canister and pressure sensor.

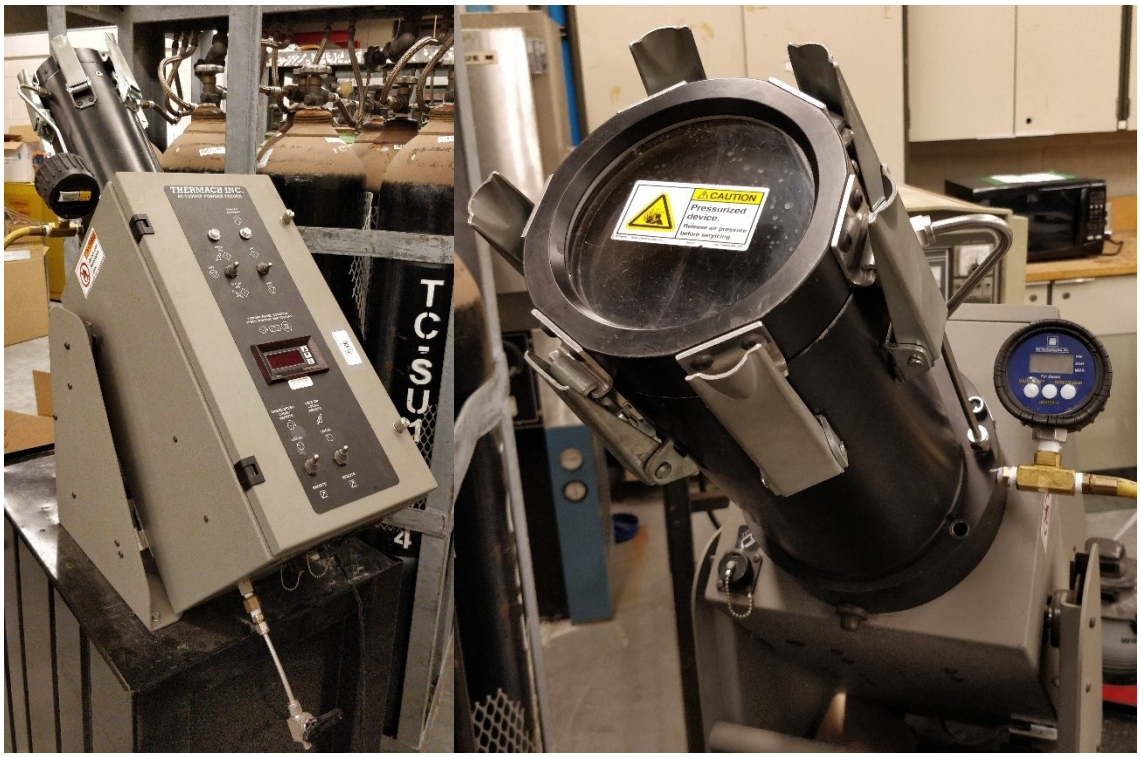

Figure 4.10 – Secondary powder feeder and alternate view showing the pressure vessel where the powder is contained

4.3.5 Spray Chamber

All the sprays were performed in an enclosed chamber, which is shown in Figure 4.11. The chamber is equipped with a system to suck the air and gas-particle mixture through a water filter. This filter is used to safely remove the micron-sized particles from the gas. With the particles removed, the remaining air and propellant gas are passed through a HEPA filter and then recirculated with the ambient air.

Figure 4.11 – CGDS chamber

4.3.6 Gas Delivery System

The gas used in this study was exclusively nitrogen, which was provided by bottle packs purchased from Linde (Mississauga, Ontario, Canada). The bottle packs consisted of 11 pre-assembled nitrogen canisters. The bottle packs used were initially pressurized at approximately 18 MPa (2600 psi).

4.4 CHARACTERIZATION EQUIPMENT AND PROCEDURES

This section of the document outlines the equipment used to produce and characterize samples taken from spray results. It also describes the procedures used in each step of the process.

4.4.1 Sample Preparation Tools

The samples to be examined under the optical digital microscope (Section 4.4.2) and the scanning electron microscope (Section 4.4.3) were prepared using the following equipment.

The samples were first cut to size using a Secotom-10 (Struers Ltd., Canada). A secondary cut was then performed using the Secotom-10 to cut across the coating, revealing the cross-section. The machine, shown in Figure 4.12, consists of a stationary blade rotating at a fixed speed, and a moving stage. The stage moves towards the blade at a fixed speed, allowing the blade to cut the sample at the desired speed. The machine uses water as a coolant/lubricant for the blade.

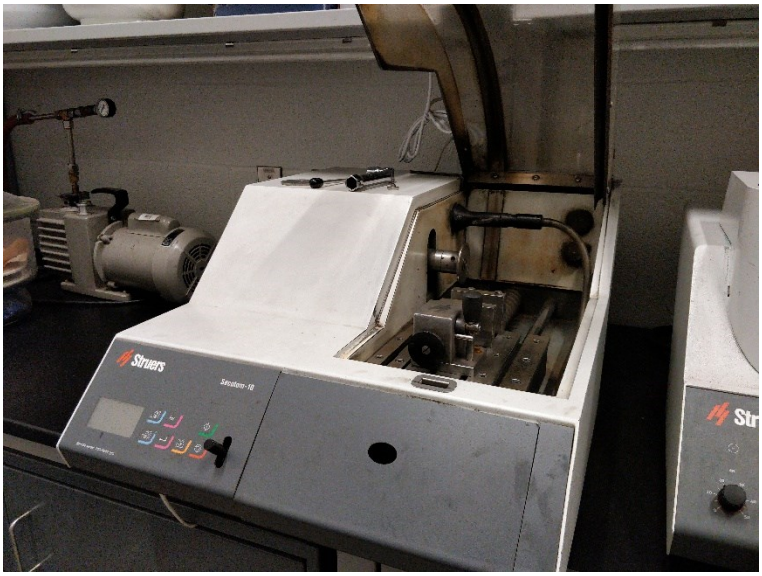

Figure 4.12 – Struers Secotom-10 cutting machine

The samples were cut using a silicon carbide blade, recommended for cutting non-ferrous materials. The manufacturer parameters show in Table 4.1 were followed for the cuts, but the cutting speed was reduced to 0.040 mm/s when cutting across the coatings to avoid delamination or excessive shearing of the material.

Table 4.1 – Struers Ltd. recommended cutting parameters

Parameter	Wheel Diameter [mm]	Wheel speed [rpm]	Cutting speed [mm/s]
Value	200	2200	0.1

The next step of the sample preparation procedure is the mounting process. The hot mounting process used here was performed using the LaboPress-3 (Struers Ltd., Canada). The samples were mounted using 30 ml of MultiFast Green (Struers Ltd., Canada)

thermosetting resin. The resin is first compacted and heated with a force of 20kN and temperature of 150°C for 6-8 minutes, then cooled for 2-3 minutes by water flowing through the machine. The LaboPress-3 is shown in Figure 4.13.

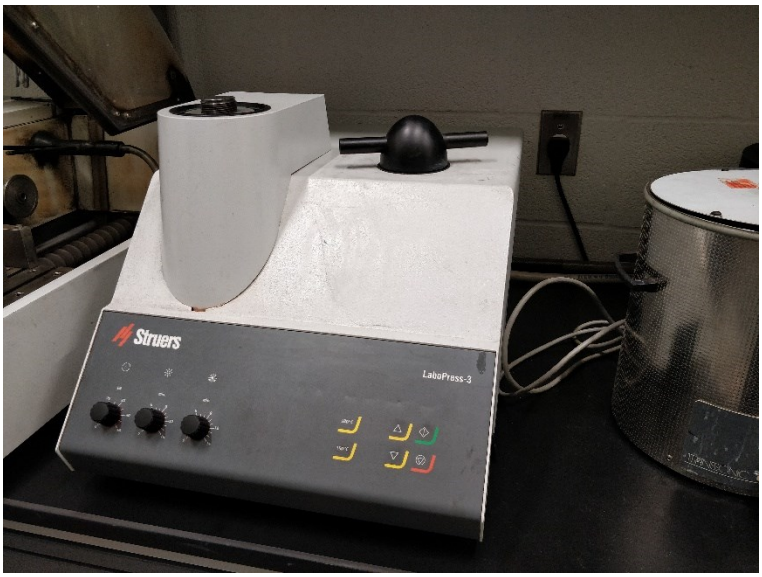

Figure 4.13 – Struers LaboPress-3 hot mounting machine

The mounted samples were then ground and polished with the TegraPol-31 (Struers Ltd., Canada), shown in Figure 4.14.

Figure 4.14 – Struers TegraPol-31 grinding and polishing machine

The polishing procedure used to produce surfaces adequate for microscope imaging is shown in Table 4.2.

Table 4.2 – Polishing procedure

Step	*Grounding/ Polishing surface*	*Suspension/ Lubricant*	*Suspension size [µm]*	*Process time*	*Force [N]*	*Disc rotation speed [RPM]*	*Sample holder speed [RPM]*
1	Piano 220	Water	N/A	1m50s	10	150	100
2	Largo	Largo	9	2m00s	15	150	0
3	Mol	Mol	3	4m00s	15	150	0
4	Chem	OP-S	0.05	3m00s	15	150	150
5	Chem	OP-S	0.05	1m00s	10	160	0

4.4.2 Optical Microscope

The samples were analyzed using a digital-optical microscope (VHX-2000E, Keyence, Canada). The microscope system, shown in Figure 4.15, uses the VH-Z100R (Keyence, Canada) zoom lens which has a maximum magnification of 1000x. The control pad controls multiple functions such as moving the stage in the XY plane, locking the stage position, controlling brightness, and changing between lighting modes. The built-in software allows for 2D or 3D imaging of the surface with progressive scanning, autofocus, image stitching, and depth composition.

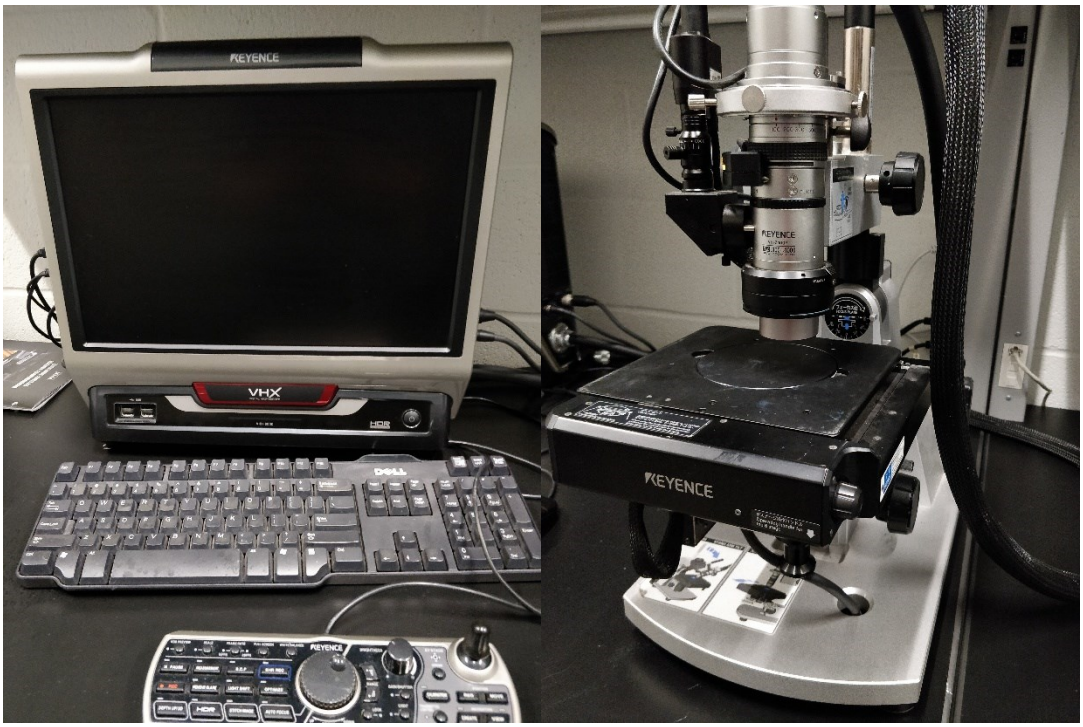

Figure 4.15 – Keyence VHX-2000E digital optical microscope and VH-Z100R zoom lens

4.4.3 Scanning Electron Microscope (SEM)

A scanning electron microscope (SEM) system was used to obtain images with a magnification that cannot be reached by the digital-optical microscope. The SEM used is an EVO-MA10 (Zeiss, United Kingdom) and was used to confirm that the coatings produced were adequately dense. This SEM system by Zeiss is equipped with a multitude of sensors allowing for a variety of imaging modes using the following detectors: back-scattered electron (BSE), secondary electron (SE), energy dispersive spectroscopy (EDS), electron backscatter diffraction (EBDS) and X-ray computed tomography (CT).

4.5 CFD MODELLING

In order to quickly and cost-effectively iterate on the prototype design, a computer model was developed. The particle model was validated using a single injection obround nozzle, made from tungsten carbide, which was being tested by Technoform Bautec Ibérica with the help of Centerline (Windsor) Ltd. The modelling was performed using commercially available Computational Fluid Dynamic (CFD) software, specifically the ANSYS Fluent

package (v16). The Fluent solver uses a finite volume method (FVM) for the discretization process.

4.5.1 Computational Domain

The nozzle geometry was drafted using commercially available Computer-Aided Design (CAD) software, SolidWorks. The computational domain, which is the interior of the nozzle, was extracted directly from the initial CAD model provided by Centerline (Windsor). The computational domain was then imported into the ANSYS geometry editor, DesignModeler. Minor changes were made to ensure the compatibility of the model with the meshing editor.

A full three-dimensional model was used as the domain is not axisymmetric along its length. The injection of particles at different angles did not allow for other simplifications such as simulating the flow in a quarter or half of the nozzle, so the full model was used for simulations. Figure 4.16 shows front and top view of the computational domain, as well as relevant dimensions.

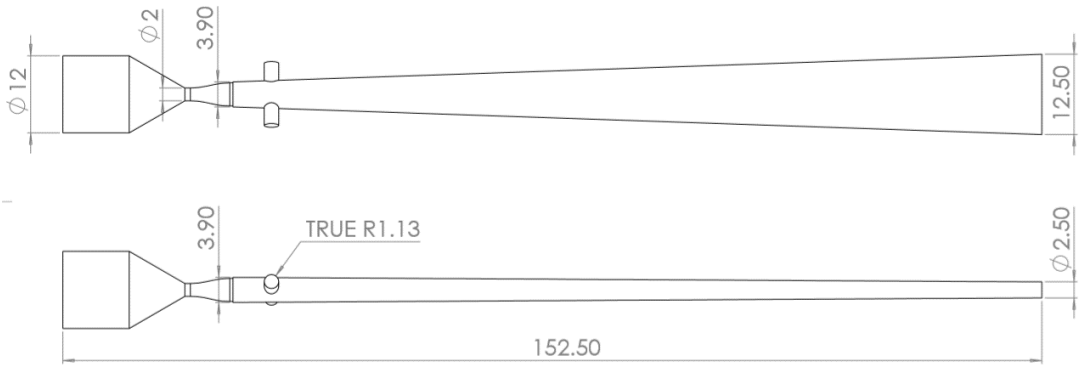

Figure 4.16 – Front and top view of the dual injection computational domain

Figure 4.17 shows the obround outlet of the nozzle computation domain, with dimensions of the flat wall and radius of the half circles on each side.

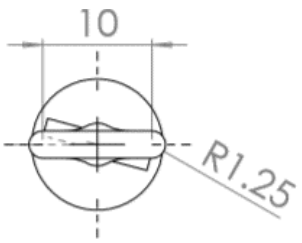

Figure 4.17 – Right view of the computational domain (gas outlet)

The domain flow is assumed to be steady state and compressible. The gas used in the simulation is nitrogen. The gas density is assumed to follow the ideal gas law, and its viscosity is assumed to change with temperature according to Sutherland's formula [18], [110]–[112].

The boundary conditions set in Fluent are based on the process parameters used by Technoform Bautec Ibérica in their spray tests on the polymeric substrate. The nozzle inlet was set as a pressure inlet, with a gauge pressure of 1.21 MPa (175 psi) and temperature of 573 K (300°C). The operating (ambient) pressure was kept at 101.325 kPa. The nozzle outlet was set as a pressure outlet, with a gauge pressure of 0 MPa and backflow total temperature of 300 K (27°C) to match ambient air conditions. The nozzle walls were set as stationary, with the no slip shear condition and no heat flux.

For the two powder inlets, flowmeters are utilized experimentally to deliver a constant gas flow rate. Therefore, the "mass flow inlet" boundary condition was used for the simulation, to match experimental conditions. Two mass flow rates were utilized for the powder inlet gas flow: 3.26×10^{-4} kg/s and 6.52×10^{-4}. The inlet temperature was set at 300 K (27°C) to match ambient conditions.

For the particle modeling, the Discrete Phase Model (DPM) was used to simulate their interactions with the flow. The inert particles were injected using the surface injection type. This injection distributes the particles across the surface of the powder inlet face. The "face normal direction" setting was used to ensure the initial velocity of the particles is normal to the injection face. It is assumed that upon reaching this point in the powder injection gas lines, the powder particles are travelling at the same velocity as the gas flow. The initial velocity of the particles is therefore taken from the converged solution of the gas flow. The initial temperature of the particles is set as 300 K (27°), the same as the boundary condition for the gas flow of the powder inlets, to match ambient conditions.

The high Mach number drag law was used for the drag coefficient between gas and particles. This drag law is based on the spherical drag law, which computes the drag coefficient using the following equation:

$$C_D = a_1 + \frac{a_2}{Re} + \frac{a_3}{Re} \quad \text{(Eq. 4.1)}$$

Where a_1, a_2 and a_3 are constants, given for a certain range of Reynolds numbers [113], [114]. The high Mach variation of this law includes corrections for high Mach numbers (greater than 0.4) and particle Reynolds numbers higher than 20 [113], [115]. This drag law was chosen due to the high relative velocity between particles and the main gas flow at the injection.

The turbulent dispersion of particles is predicted using a discrete random walk model. This model uses a stochastic method to determine the instantaneous gas velocity near each particle and predict its effect on the particle's trajectory. This is computed multiple times for each particle to simulate multiple trajectories that could be taken by the particle due to flow turbulence [113]. Since the flow turbulence is calculated with a Reynolds-Averaged Navier Stokes (RANS) model, which averages the fluctuations in the flow caused by turbulence, the use of a turbulent dispersion model is essential to model the trajectory of particles [116].

Particle collisions with the nozzle walls were considered to be elastic (coefficient of restitution = 1). In reality, some energy will be lost with each collision, which will reduce the particle velocity. However, as the real coefficient of restitution is unknown for these collisions, the interactions were assumed to be elastic as an approximation.

The diameter distribution was set as uniform for each injection and bins were created manually from 10 µm to 70 µm, in 10 µm increments, to account for the majority of particle diameters found in Centerline (Windsor) Ltd.'s pure aluminum powder (the full size distribution of the powder is shown in Figure 4.1b). A normal particle distribution could have been used. However, implementing this distribution would introduce a different number of particles for each particle size. Keeping the same number of particles for every size makes it easier to visualize and directly compare the distribution of different particle bins in this context, which is why bins were used.

4.5.2 Domain Meshing

The nozzle domain was meshed using the meshing module included in the ANSYS package. An unstructured three-dimensional tetrahedral mesh was used to mesh the nozzle, with an inflation layer along the nozzle walls to resolve the flow boundary layers. Figure 4.18 shows the tetrahedral mesh at the nozzle outlet.

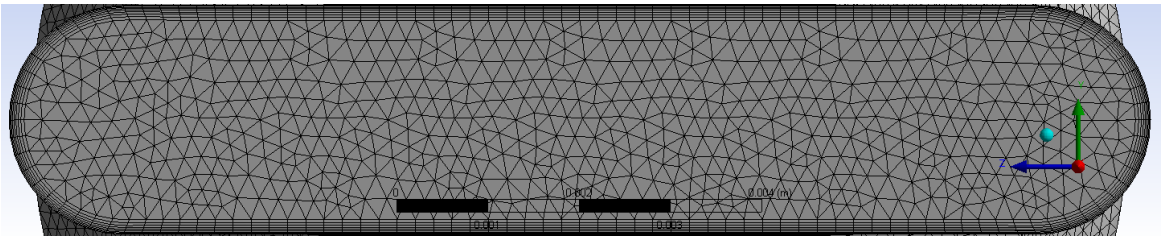

Figure 4.18 – Mesh at the nozzle outlet

Figure 4.19 provides a zoomed-in view of the mesh at the nozzle outlet to show the inflation layers used. The inflation layer used for this mesh is composed of eight layers of varying thicknesses.

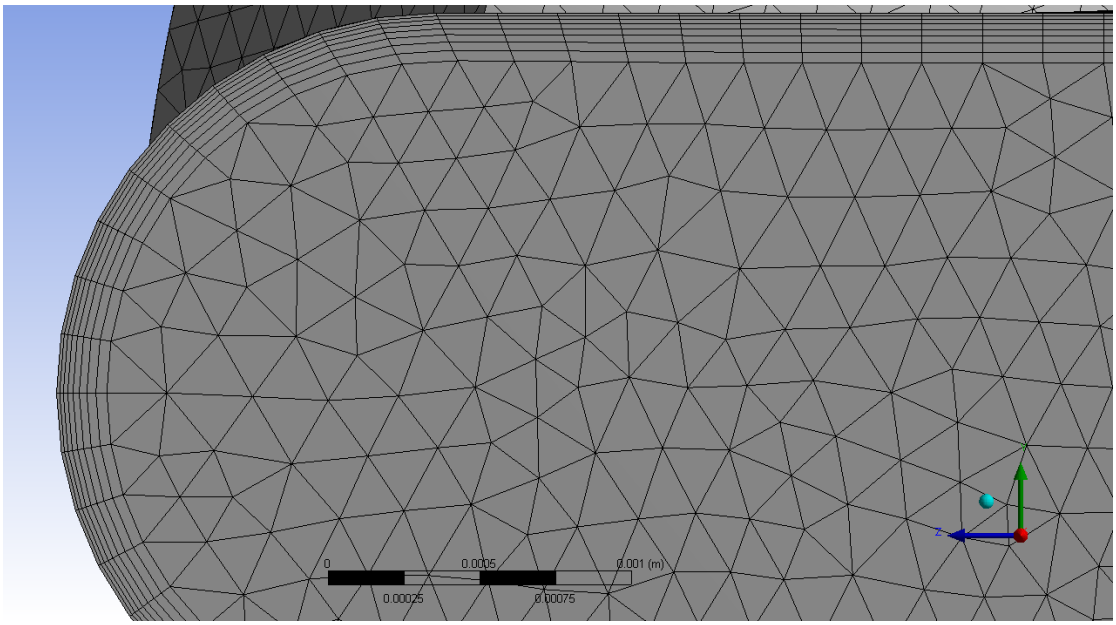

Figure 4.19 – Zoom of the mesh at the outlet, showing the multiple inflation layers

Figure 4.20 shows the mesh of the powder inlet, where particles are injected. Inflation layers are also used here along the walls. The surface injection used by the DPM determines the number of particles to inject based on the mesh size, so a finer mesh will generate more particles.

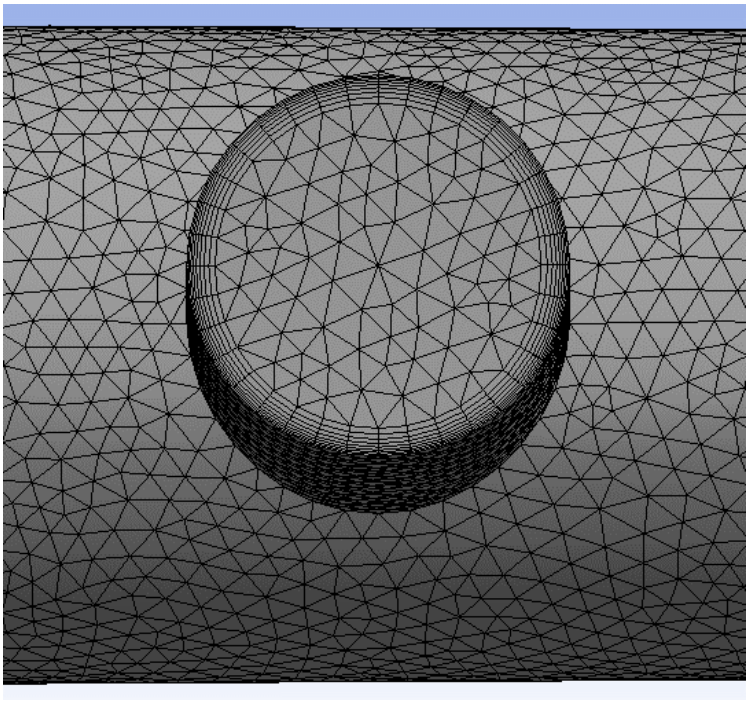

Figure 4.20 – Zoom of the powder inlet mesh

The mesh shown in Figure 4.18 - Figure 4.20 is composed of 1,195,360 elements. A mesh study, described in detail in Section 4.5.5, was performed to ensure that this mesh is adequate for the simulations.

4.5.3 Governing Equations

The CFD simulation uses the Navier-Stokes equations of continuity, momentum, and energy to resolve the flow. These equations can be expressed as follows, respectively:

$$\frac{\partial \rho}{\partial t} + \nabla \cdot (\rho \vec{u}) = S_m \qquad \text{(Eq. 4.2)}$$

$$\frac{\partial (\rho \vec{u})}{\partial t} + \vec{u} \cdot \nabla (\rho \vec{u}) = -\nabla P + \mu \nabla^2 \vec{u} + \frac{1}{3} \mu \nabla (\nabla \cdot \vec{u}) + \rho \vec{g} \qquad \text{(Eq. 4.3)}$$

$$\frac{\partial (\rho E)}{\partial t} + \nabla \cdot (\vec{u}[\rho E + P]) = \nabla \cdot \left(k_{eff} \nabla T - \sum_j h_{s_j} \vec{J}_j + \left[\bar{\bar{\tau}}_{eff} \cdot \vec{u} \right] \right) + S_h \qquad \text{(Eq. 4.4)}$$

Where ρ is the density of the fluid, t is time, $\vec{u}$ is the velocity vector, P is the static pressure, μ is the dynamic viscosity of the fluid, I is the unit tensor, $\vec{g}$ is the directional gravitational force and other body accelerations, E is the energy term, k_{eff} is the effective conductivity, ∇T is the temperature gradient, h_s is the enthalpy, $\vec{J}_j$ represents the diffusion of j, and $\bar{\bar{\tau}}_{eff} \cdot \vec{v}$ is the viscous dissipation term. S_m and S_h are the source terms for added mass and heat sources, respectively, which are null in this case and therefore eliminated. Gravitational forces are also considered to be negligible. The energy term, E, is comprised of multiple terms to consider internal energy and kinetic energy, as shown here:

$$E = h_s - \frac{P}{\rho} + \frac{v^2}{2} \qquad \text{(Eq. 4.5)}$$

For the turbulence model, the RANS-based RNG k-ε model was utilized. The standard k-ε model is a two-equation model which is economic, in terms of computational time required, and offers reasonable accuracy for many turbulent flow problems [117]. The RNG k-ε model was chosen however, as improvements to the standard model are made through the use of the renormalization group mathematical technique, making the RNG model more accurate and reliable compared to the standard model [112], [117].

For the simulations, the default SIMPLE scheme was used for the pressure-velocity coupling. The SIMPLE algorithm is based on the predictor-corrector approach, and couples velocity and pressure to obtain the pressure field and maintain mass conservation [117]. All parameters were calculated using a second order upwind scheme.

For FVMs using an unstructured (non-Cartesian) mesh, the flux calculation between cell faces includes additional terms relating to the gradients. Thus, the gradient operator must be approximated via a discretization method [118], [119]. In the case of turbulent flows modeled using a RANS method, the gradient operator is also needed for additional turbulence equations, increasing the importance of the gradient discretization [118], [119]. The most common gradient calculation methods are based on either the divergence theorem (DT), also known as Green-Gauss, or the least squares (LS) method [119].

Fluent offers three gradient discretization schemes, the Green Gauss cell-based method, Green-Gauss node-based method, and the least squares cell-based method. The first two are based on DT, as their name implies, and the latter is based on LS. In this case, the least squares cell-based method was used to calculate the gradient. This method was chosen as for an irregular, unstructured mesh, its accuracy is comparable to the Green-Gauss node-based method while still being less expensive in terms of computational requirements [117]. This method works by assuming that the gradient solution varies linearly between the centroids of each cell. To calculate the gradient, the solver takes the difference between centroid values for two adjacent cells, which is equal to the gradient between the centroids multiplied by the distance between centroids. This is repeated for all adjacent cells, which will yield a matrix equation with the gradient as the unknown, since centroid temperatures are known, as well as the distance between centroids [119], [120]. Taking temperature as an example, this can be written as

$$[d_{np}][T_n - T_p] = [(\nabla T)_p] \quad \text{(Eq. 4.6)}$$

Where subscript n denotes the adjacent cell's centroid, subscript p denotes the starting cell's centroid, and d_{np} is the distance between centroids. Depending on the number of faces (number of adjacent cells) n, the matrix size will change. For a non-square matrix, the solution is approximated using the LS method, which aims to reduce the error stemming from the approximation. The method is rewritten as

$$(\nabla T)_p = G^{-1} d^T (T_n - T_p) \quad \text{(Eq. 4.7)}$$

Where

$$G = (d_T d) \quad \text{(Eq. 4.8)}$$

Since the mesh is constant throughout the calculation and the factor G is only dependent on the geometry of the mesh, it only needs to be calculated once for the entire simulation,

making this method very efficient [119], [120]. Fluent also uses weighing factors to improve accuracy for thin elements [117]. The weighing factors therefore rely on the mesh geometry only, and are also only calculated once.

4.5.4 Convergence criteria

The convergence of the flow simulations was based on residual values. In this case, seven residual values were monitored: continuity, x-velocity, y-velocity, z-velocity, energy, k, and ε. The solution was considered to be converged once all residuals had decreased by three orders of magnitude or more.

4.5.5 Mesh Validation

A mesh study was performed to ensure results remained consistent for different element sizes. Four meshes were tested for the final prototype, with approximately 0.4, 1.2, 2 and 3 million elements. Overall, flow characteristics from all meshes were similar with a pronounced shockwave appearing approximately 125 mm along the nozzle length. Some details of diamond shocks inside the nozzle near the throat are lost with the coarser mesh, however this had no significant impact on particle trajectories at the nozzle outlet. Figure 4.21 shows a graph of the centerline gas velocity along the nozzle length for all tested mesh sizes. The graph shows that beyond 1.2 million elements, there is very little change in the velocity results at the centerline.

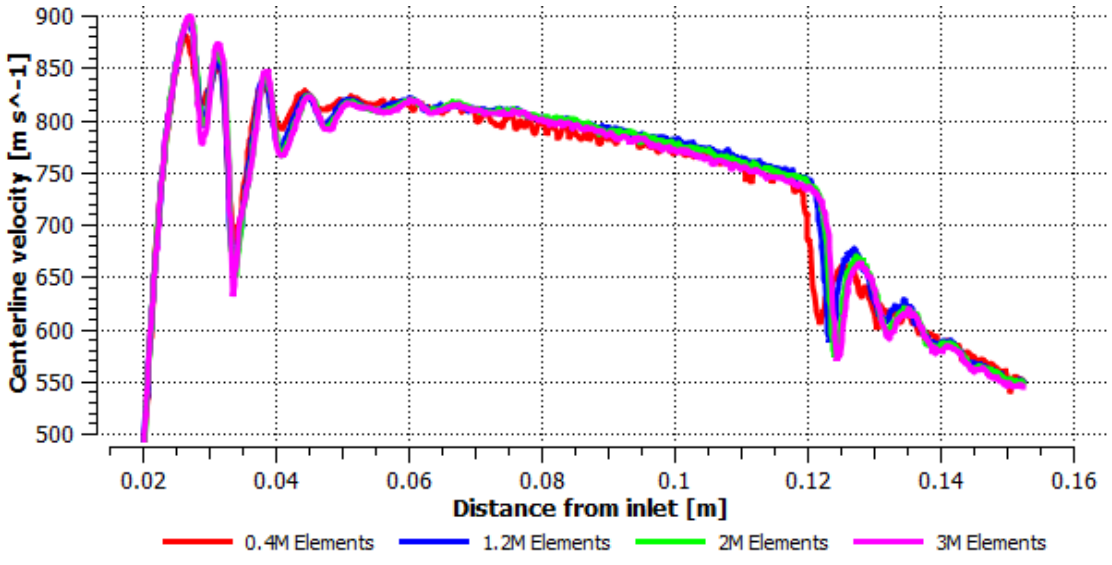

Figure 4.21 – Comparison of centerline velocity along the nozzle length for all mesh sizes. Values under 500 m/s were excluded for graph clarity.

Figure 4.22 shows the gas velocity contour at a cross-section of the nozzle for all mesh sizes tested. The cross-section is taken 40 mm downstream. A zone of lower velocity can be seen on each side of the flow, which corresponds to area near the gas inlets used for the powder injection. Note that the scale used for velocity is a global scale, in order for Figure 4.22 and Figure 4.23 to be compared directly.

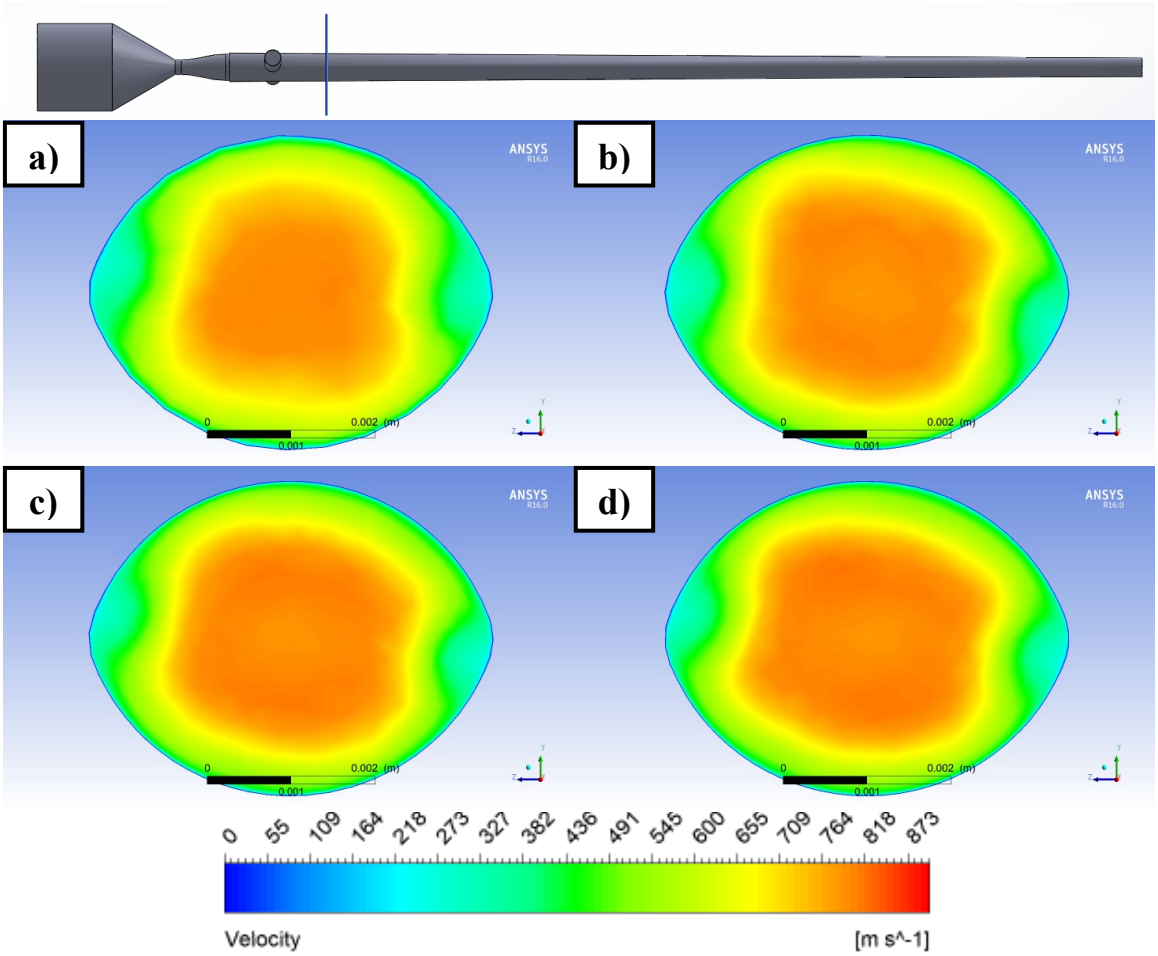

Figure 4.22 – Cross-section of the gas velocity profile 40 mm from the nozzle inlet for all mesh sizes; a) 0.4M elements, b) 1.2M elements, c) 2M elements, d) 3M elements

Figure 4.23 also shows a gas velocity contour, where the cross-section is now taken 120 mm downstream. This is an important point to observe as it is near the shockwave, where the flow conditions change drastically. Figure 4.23 shows that there is a noticeable difference in the velocity results when looking at the coarse mesh. The other meshes give similar velocity profiles, as they are in better agreement in predicting the shockwave position.

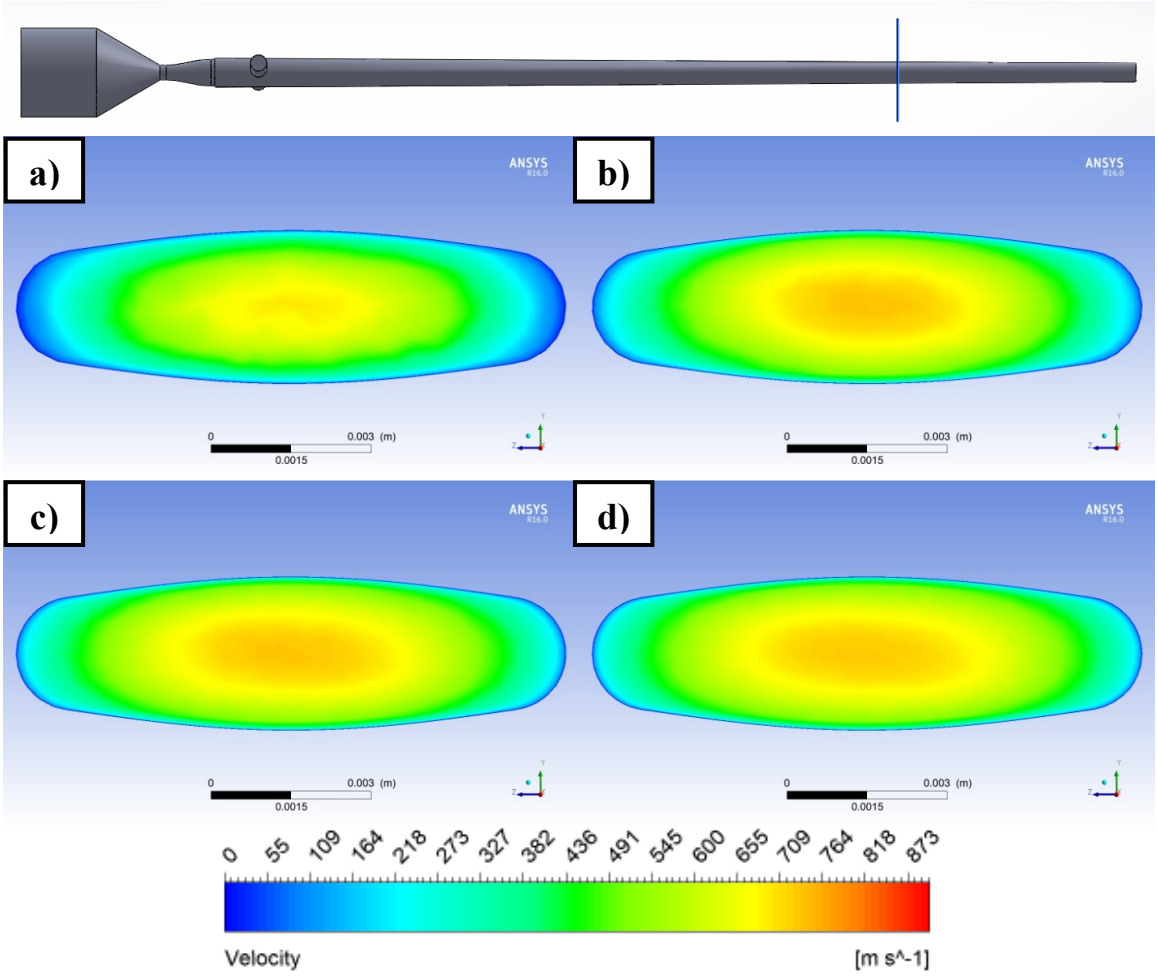

Figure 4.23 – Cross-section of the gas velocity profile 120 mm from the nozzle inlet for all mesh sizes; a) 0.4M elements, b) 1.2M elements, c) 2M elements, d) 3M elements

Particles were injected in the 0.4 million and 3 million element meshes initially, in order to compare particle distribution within the nozzle, and determine if the slight differences in the shockwave position and detail had an effect on them. Figure 4.24 shows a comparison of the particle distribution at the nozzle exit plane for the 0.4 million and 3 million element meshes. Only the particles with a diameter of 20 µm are shown, and display a similar trend for both meshes. The 3 million element mesh has significantly more particles displayed, due to the way the DPM surface type injection works in Fluent.

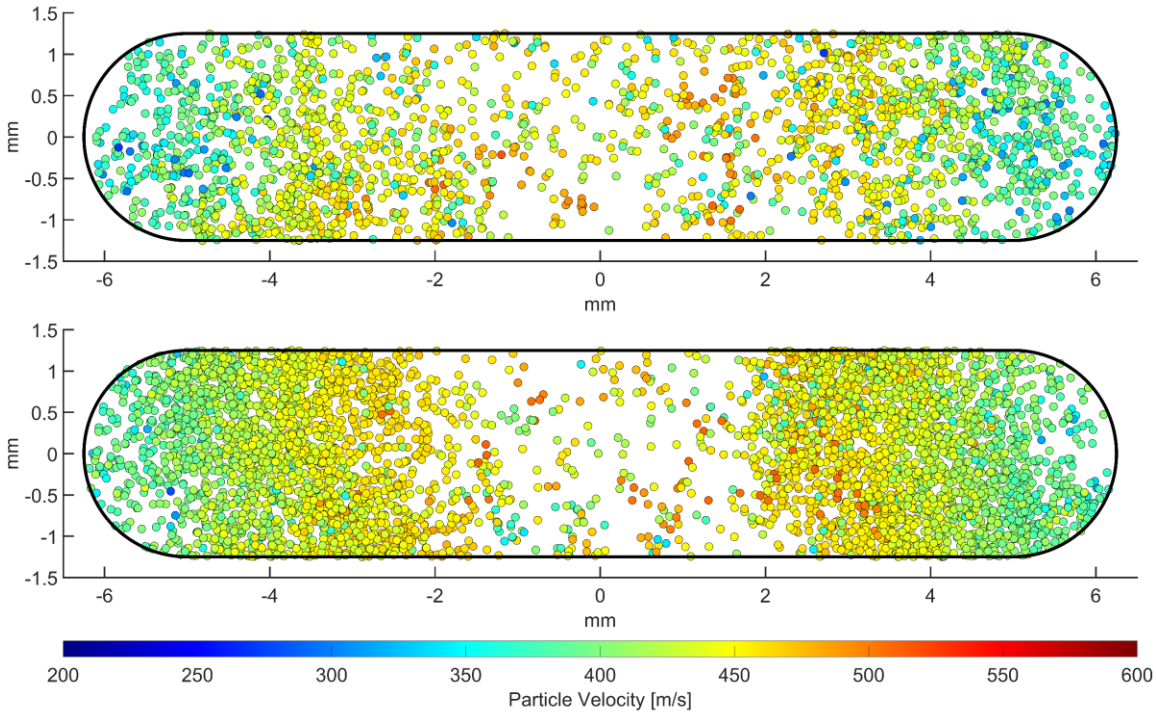

Figure 4.24 – Comparison of the 20 µm particle distribution at the nozzle exit plane for the 0.4 million element mesh (top) and the 3 million element mesh (bottom)

It is also worth noting that the computational time between meshes was significant. The 0.4 million element mesh converged in a few hours, while the 3 million element mesh took approximately a week. The 1.2 and 2 million element meshes took approximately 12 and 30 hours for a solution to converge, respectively. The simulations were performed using serial-processing on a stock Intel® Core™ i5-4690k processor.

Therefore, to maximize the accuracy of the flow characteristics and particle distribution results, as well as minimizing computing time, the 1.2 million element mesh was selected. The final mesh had 1,195,360 elements, with a minimum orthogonal quality of 0.15789 and a maximum aspect ratio of 66.441. The ANSYS documentation advises a minimum of 0.1 for orthogonal quality and maximum aspect ratio below 20. While the maximum aspect ratio in this case is over 20, it is worth noting that the average aspect ratio for this mesh is 10.713 and that the elements with a high ratio are not part of the bulk flow but rather close to the walls. The skewed cells were found in the thinnest layer of inflation, and resolving this issue required increasing the element count or increasing the size of the inflation layer, which caused stability issues in Fluent. With all the cells otherwise having an acceptable

orthogonal quality, it is was not expected that a few skewed cells would have a significant impact on the results.

The solution was therefore calculated using this mesh, with iterations running until all residuals had decreased by a minimum of three orders of magnitude. Other designs were also meshed as part of this study, but meshing parameters were all based on the ones used in the mesh study. Resulting meshes were comparable to this one in terms of element density, aspect ratio, and orthogonal quality.

5 RESULTS AND DISCUSSION

5.1 OBROUND WC NOZZLE PROTOTYPE

As mentioned in Section 2.1, Technoform had already done some cold spray testing with non-axisymmetric shapes in collaboration with Centerline (Windsor) Limited. The two companies settled on the obround profile for further testing and developed a tungsten carbide prototype compatible with Centerline's commercial system. The obround shape, also often called "stadium", is a 2D geometric shape that is defined as a rectangle capped off by semicircles on each end [121], [122]. The obround shape can be seen as an evolution of the previously tested rectangular shapes developed by *Alkhimov et al.* and at the NRC [40], [43]. A copy of the WC prototype was sent to the University of Ottawa for further testing in the uOttawa Cold Spray Lab. Figure 5.1 shows a top view of the WC nozzle prototype received from Technoform.

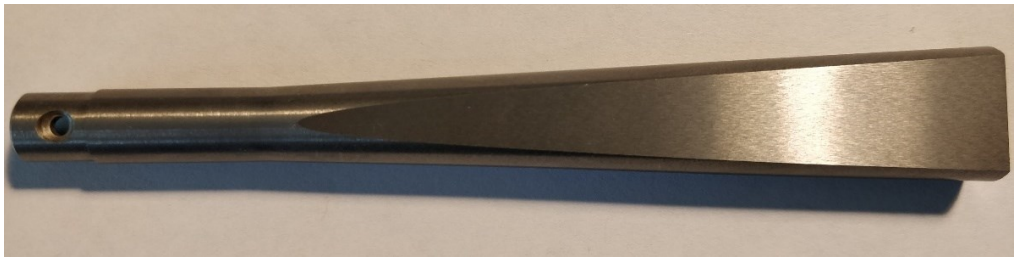

Figure 5.1 – Obround WC nozzle prototype, top view showing powder injection hole

Figure 5.2 provides a different angle of the WC prototype, which shows the obround nozzle outlet.

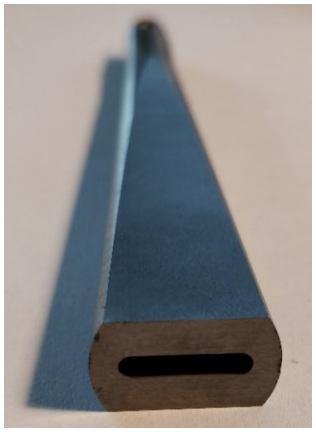

Figure 5.2 – Obround WC nozzle prototype, nozzle outlet view showing obround shape

Figure 5.3 shows the obround geometry of the outlet and its dimensions directly from the CAD model. Note that the horizontal dotted line is the reference plane from which powder inlet angles are measured. Thus, the powder inlet of WC prototype is at a 90° angle from the reference plane, as seen in Figure 5.1

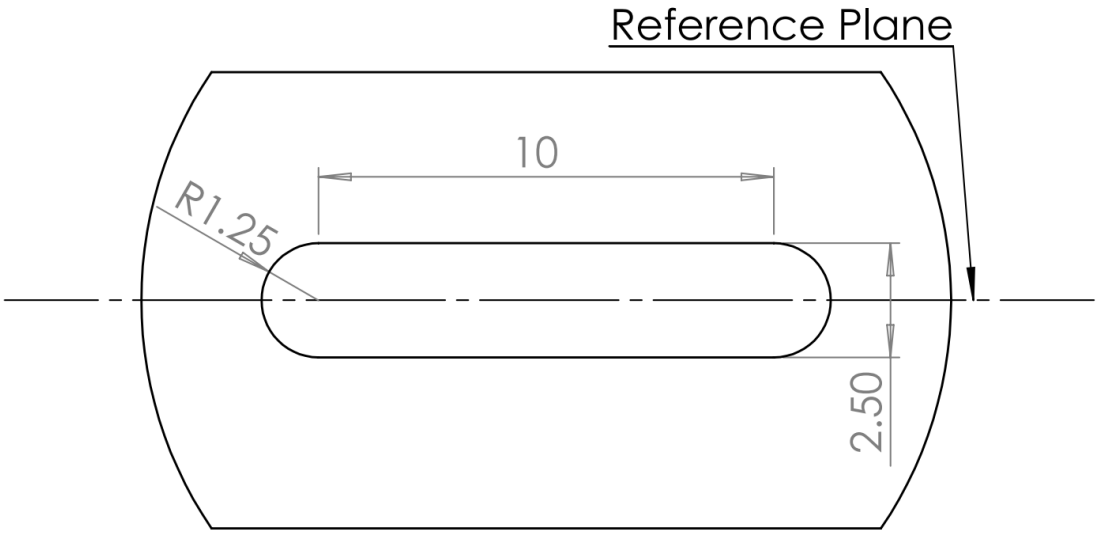

Figure 5.3 – Obround WC nozzle outlet geometry and horizontal reference plane for powder inlet angles

Initial tests were conducted by spraying the Centerline (Windsor) SST-A5001 pure aluminum powder on aluminum 6061-T6 substrates. A single-track coating was produced by spraying a single line with the nozzle, in order to measure the width of the deposition produced by the WC prototype. Table 5.1 shows the spray parameters used to obtain the aluminum deposit.

Table 5.1 – CGDS parameters for initial testing of the WC prototype (90° inlet)

Pressure [MPa]	*Temperature [°C]*	*Stand-off distance [mm]*	*Traverse speed [mm/s]*	*Powder feeding [g/min]*	*Number of passes*	*Injection gas flow rate [kg/s]*
2.07 (300 psi)	300	10	15	8.2	1	3.26×10^{-4} (30 SCFH)

The resulting coating from this spray, shown in Figure 5.4, is similar to Technoform's deposition results when spraying on the polymer substrate. The nozzle performance is poor in both cases, as particles are only deposited near the center of the nozzle. The deposition has an approximate width of 6.5 mm, as measured in Figure 5.4 using the 3D microscope. In theory, the nozzle is designed to produce an aluminum trace of 12.5 mm in width, which is equal to the width of the nozzle outlet. The second measurement on Figure 5.4 represents the width of the substrate that seems to have been impacted by particles, which is approximately 12.67 mm. This can be measured, as particles that have impacted the surface without adhering leave craters on the substrate surface. These craters are easily visible under the microscope, showing that particles have impacted the surface without adhering.

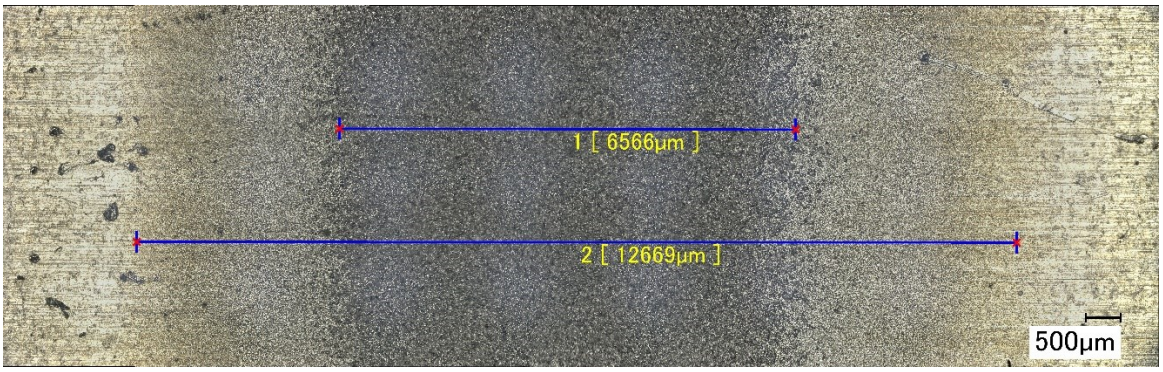

Figure 5.4 – Coating deposited with the WC prototype (90° inlet), using parameters from Table 5.1

5.2 Problem Assessment of WC Nozzle Prototype

To improve the design of the obround nozzle, and resolve the issues present with the WC nozzle prototype, the cause of the issues must first be understood. This section will investigate the two biggest problems with the WC prototype: the particle distribution at the exit of the nozzle, and the material the nozzle is made from.

5.2.1 Particle Distribution Problem

As explained in the previous section and shown in Figure 5.4, the WC prototype demonstrates poor performance in terms of coating width, despite the wide exit of the nozzle. To further investigate this issue, CFD was utilized to model the gas flow and

particle injection. The simulation results were used to determine how particles would interact with the flow and nozzle walls, as well as their distribution on the nozzle exit plane.

The test case simulated was based on Technoform spray parameters, with a stagnation pressure of 1.21 MPa (175 psi) and stagnation temperature of 350 °C for the main gas flow. Traverse speed and stand off distance were not taken into consideration as only the flow inside the nozzle was studied. Figure 5.5 shows the resulting flow velocity distribution within the nozzle.

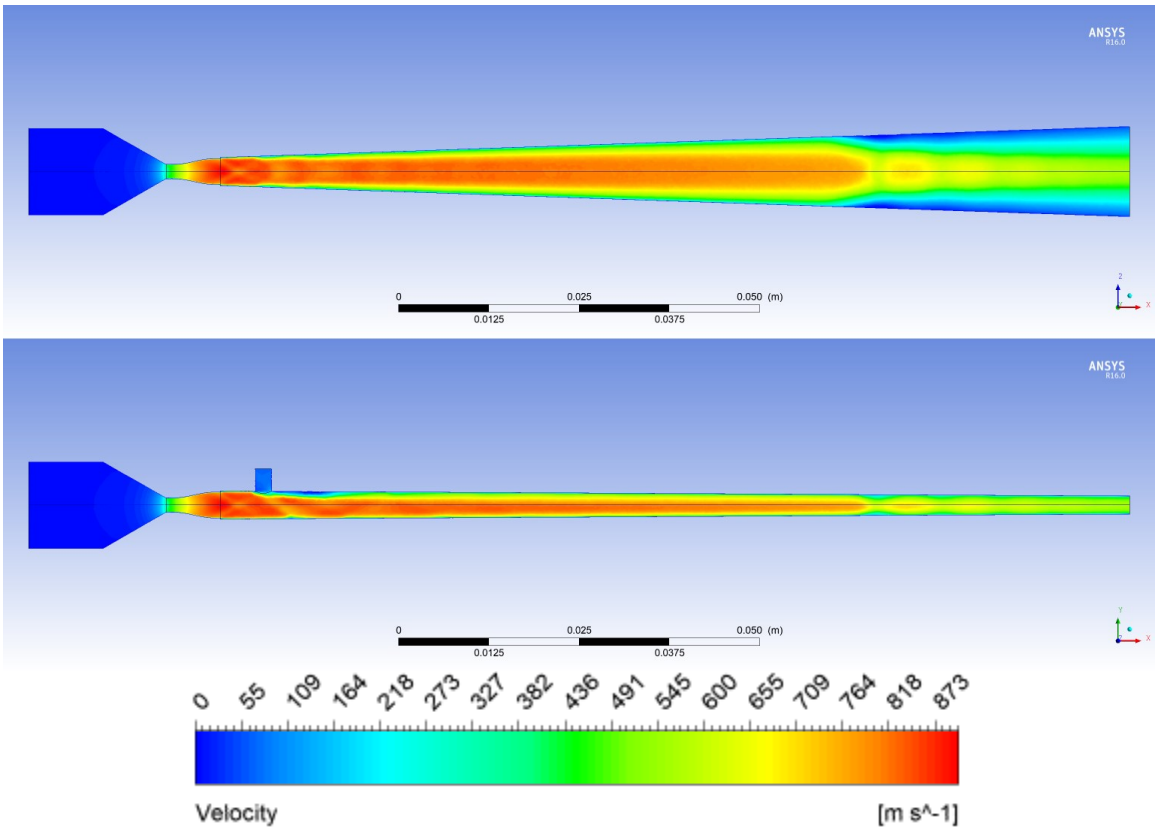

Figure 5.5 – WC nozzle velocity results, top view (top) and side view (bottom)

Figure 5.5 demonstrates that the flow accelerates through the converging-diverging nozzle as expected. The core of the flow is surrounded by a boundary layer, which is the region near the nozzle wall with a lower velocity. This is caused by the viscosity of the fluid. Oblique shocks form in the flow, before the powder injection inlet, due to a small step in the nozzle. These shockwaves dissipate as the flow accelerates, and are also disturbed by the secondary flow entering from the powder injection inlet. Note that there is also a shockwave which forms further downstream in the diverging portion of the nozzle. As the

fluid accelerates through the nozzle, its temperature and pressure decrease. In this case, due to the low inlet pressure, the pressure inside the nozzle drops below the ambient pressure. To satisfy the boundary condition at the nozzle outlet, a shockwave forms within the nozzle to increase the pressure in order for the outlet pressure and ambient pressure to match. The shockwave will also increase the gas temperature and reduce the gas velocity. It also causes flow separation due to the abrupt changes in flow velocity, combined with the geometry (angle of the walls) of the diverging nozzle. The flow within the nozzle is in good agreement with the 1D isentropic flow solution for a converging-diverging nozzle, and in line with other cold spray flow simulations [17], [18], [110]–[112].

With the flow simulated, the particles were injected in the powder inlet. Figure 5.6 shows the particle distribution and sizes on the exit plane of the nozzle. The injection point, which is located upstream of the nozzle, is indicated by a black arrow.

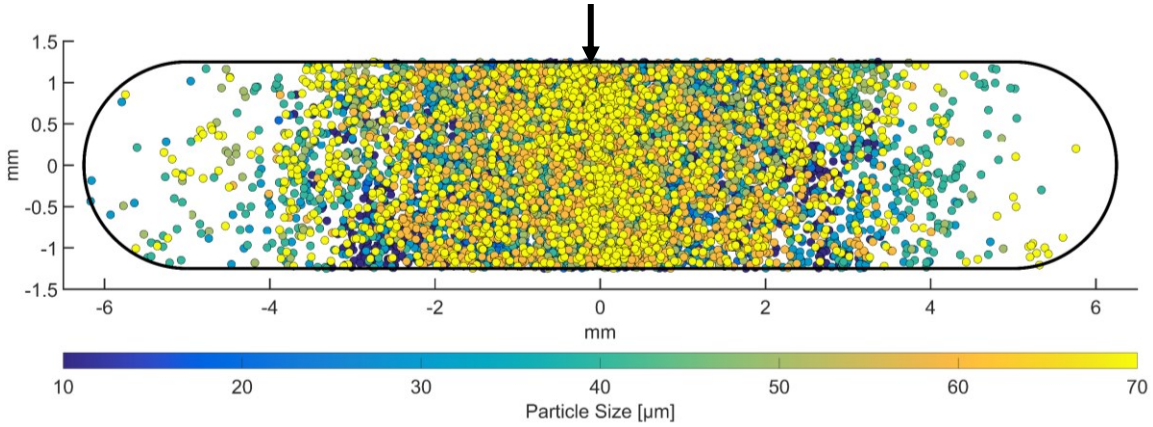

Figure 5.6 – Full particle distribution at WC nozzle outlet. Particle diameters range from 10 to 70 µm. The upstream inlet position is shown by a black arrow

The resulting particle distribution is in agreement with the spray results from both Technoform and uOttawa. The particles are mainly located in the center of the wide obround shape, with poor distribution on the edges. Poor deposition of the particles travelling near the rounded nozzle walls could also be aggravated by the lower gas velocity (and therefore lower particle velocity). Figure 5.7 shows the velocity of the gas flow at the exit plane of the nozzle, demonstrating that the velocity is lower near the nozzle walls due to boundary layer effects. The velocity is also reduced near the rounded walls due to the flow "detaching" from nozzle walls after the shockwave, as seen in Figure 5.5.

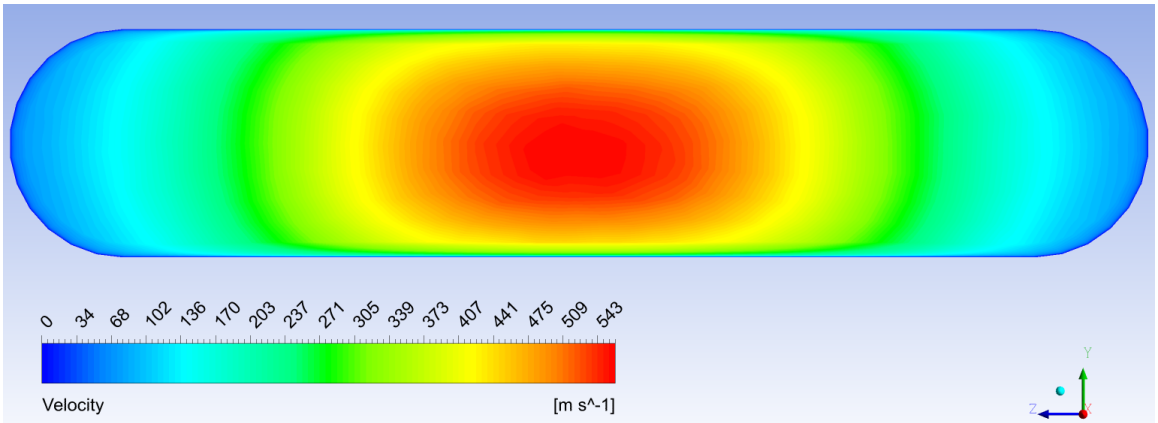

Figure 5.7 – Gas velocity at the exit plane of the WC nozzle

Figure 5.8 shows the particle distribution and velocity of particles with 20 and 50 µm diameters. Note the significant change in velocity between the two particle sizes.

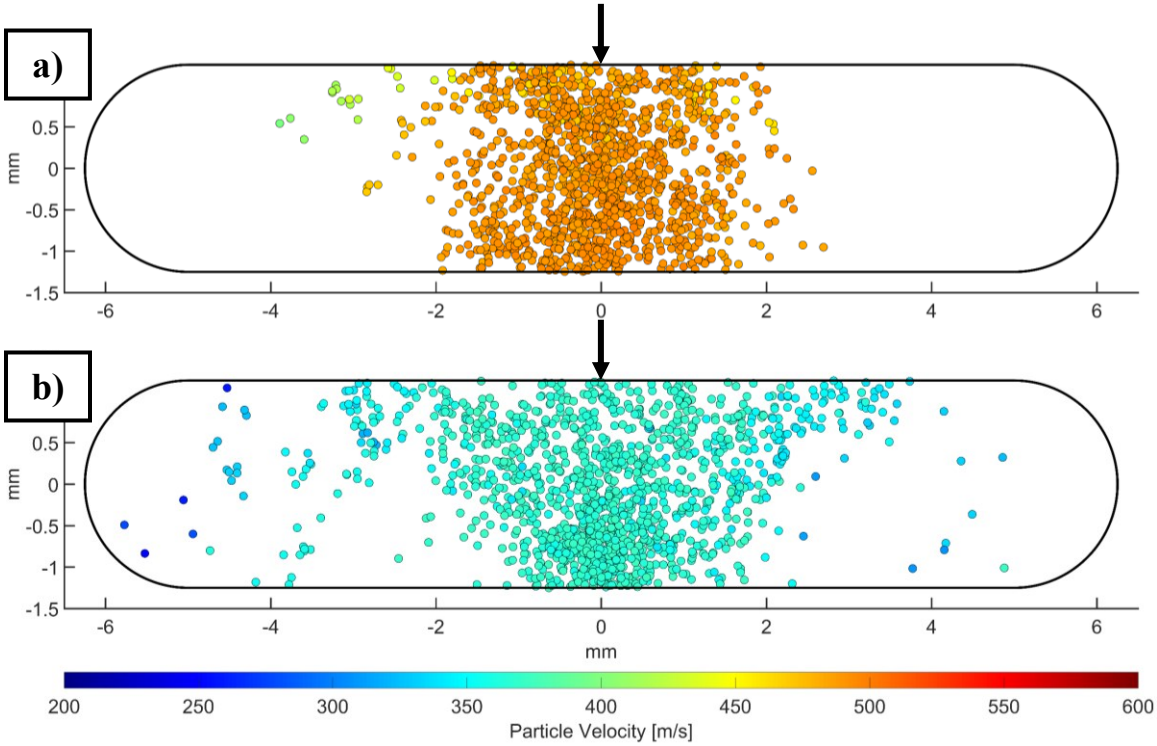

Figure 5.8 – WC nozzle particle velocity at the exit plane, showing slower particle velocity near the rounded walls for a) 20 µm particles and b) 50 µm particles

The difference in velocity at the nozzle exit plane is caused by the difference in particle size. Recall Equation 2.12, shown in Section 2.2.2, which describes the particle velocity as a result of the interactions with gas flow. When the particle diameter is increased, two factors are affected within this equation: the mass (m_P) and projected area (A_P) of the

particle. As the diameter of a spherical particle increases, its mass will increase faster than its projected area. This is because its mass is a function of the diameter cubed, while its projected area is a function of the diameter squared. The equation therefore demonstrates that for larger spherical particles, the acceleration decreases due to the increase in mass, despite the larger projected area. This is why the 50 μm diameter particles are travelling slower than the 20 μm diameter particles in Figure 5.8, despite both of them being at the same location in the nozzle. The change in diameter will also affect the particle Reynolds number, and thus the drag coefficient. However, the Reynolds number will rapidly decline as the particle accelerates and the relative velocity between it and the flow is reduced. This effect is therefore less significant on the particle velocity compared to the increase in mass.

5.2.2 Nozzle Material Problem

Another problem with the WC prototype is the material used for nozzle. While this nozzle is adequate for a prototype, it is limited with regards to the upper limit of operating pressure and temperature of the spray. As mentioned in Chapter 2, clogging is a common issue in the cold spray process, and is particularly common for feedstock materials such as aluminum. Polybenzimidazole is therefore preferable for the nozzle construction in order to reach higher temperatures and pressure. Higher temperatures are particularly likely to increase the frequency of clogging when using a non-polybenzimidazole nozzle in combination with aluminum feedstock [45]. Once the particle issue is addressed, this problem must also be resolved to improve the performance of the next prototype, as detailed in Section 5.4.

5.3 Optimization of Injection Location

Having validated that the model qualitatively matches the experimental results in terms of particle distribution, further simulations were performed to optimize the particle distribution at the exit plane. Figure 5.9 shows the behaviour of the particles as they travel inside the nozzle. It is clear that most particles remain in the center portion, with regards to the width of the nozzle. However, when looking at the side view, it can be seen that particles bounce repeatedly inside the nozzle until they exit.

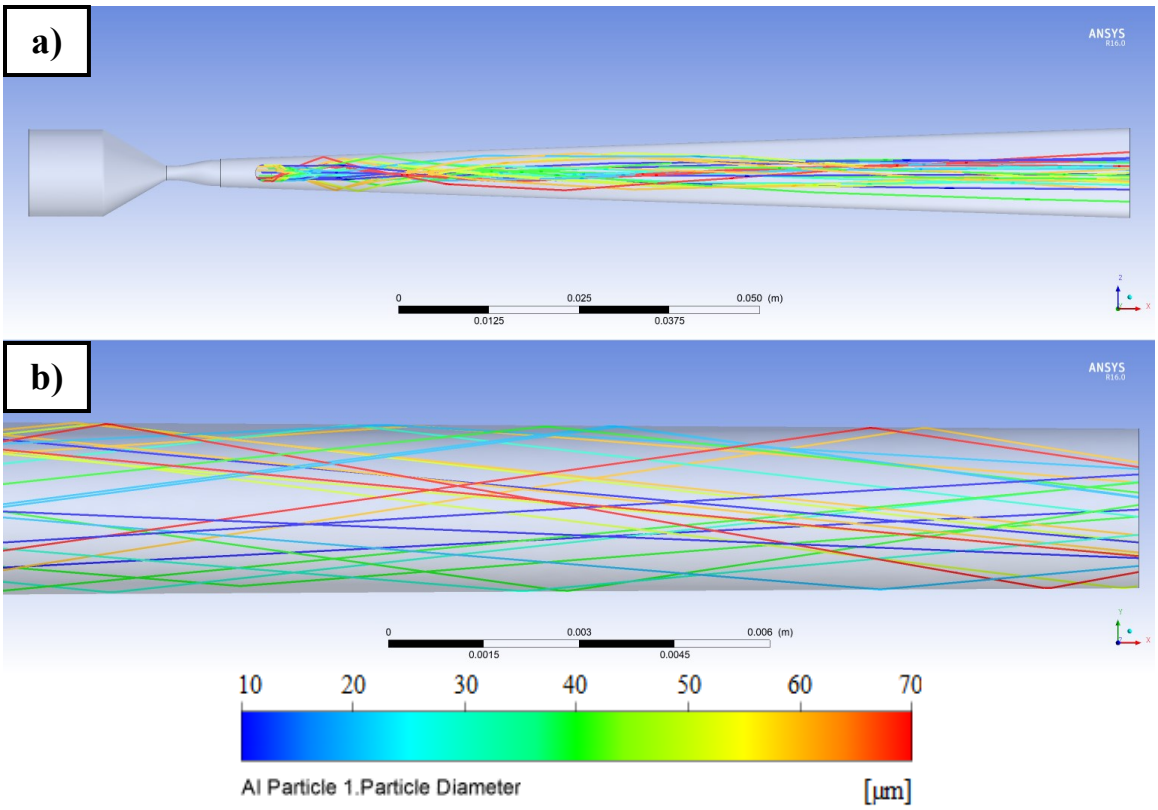

Figure 5.9 – Particle behaviour inside the nozzle for 25 particle tracks; a) top view, showing the particles remaining in the center portion of the nozzle and b) side view zoom, showing the particles bouncing against nozzle walls

Before opting for a complete redesign of the nozzle shape and profile, a simpler approach was taken. The issue with the particle distribution in the WC obround prototype is caused by particles bouncing back and forth in the same direction. As shown in Figure 5.9, the particles injected through the powder inlet have enough radial velocity to bounce repeatedly against the nozzle walls. However, due to the position of the powder inlet, the particles only bounce against the flat walls of the nozzle. This causes them to remain mostly in the middle portion of the nozzle and does not help to push them towards the two rounded edges of the obround nozzle.

However, it was hypothesized that relocating the injection point could take advantage of the radial velocity of the particles and particle-wall interactions to enhance their distribution when reaching the exit. To this end, the injection point was rotated by 90 degrees to make it flush with the horizontal plane (0° angle with the horizontal plane), with the aim of making the particles bounce in multiple directions within the obround shape.

This new inlet position is referred to as the 0° inlet. Figure 5.10 shows the new injection location in comparison to the original 90° injection point used on the WC prototype.

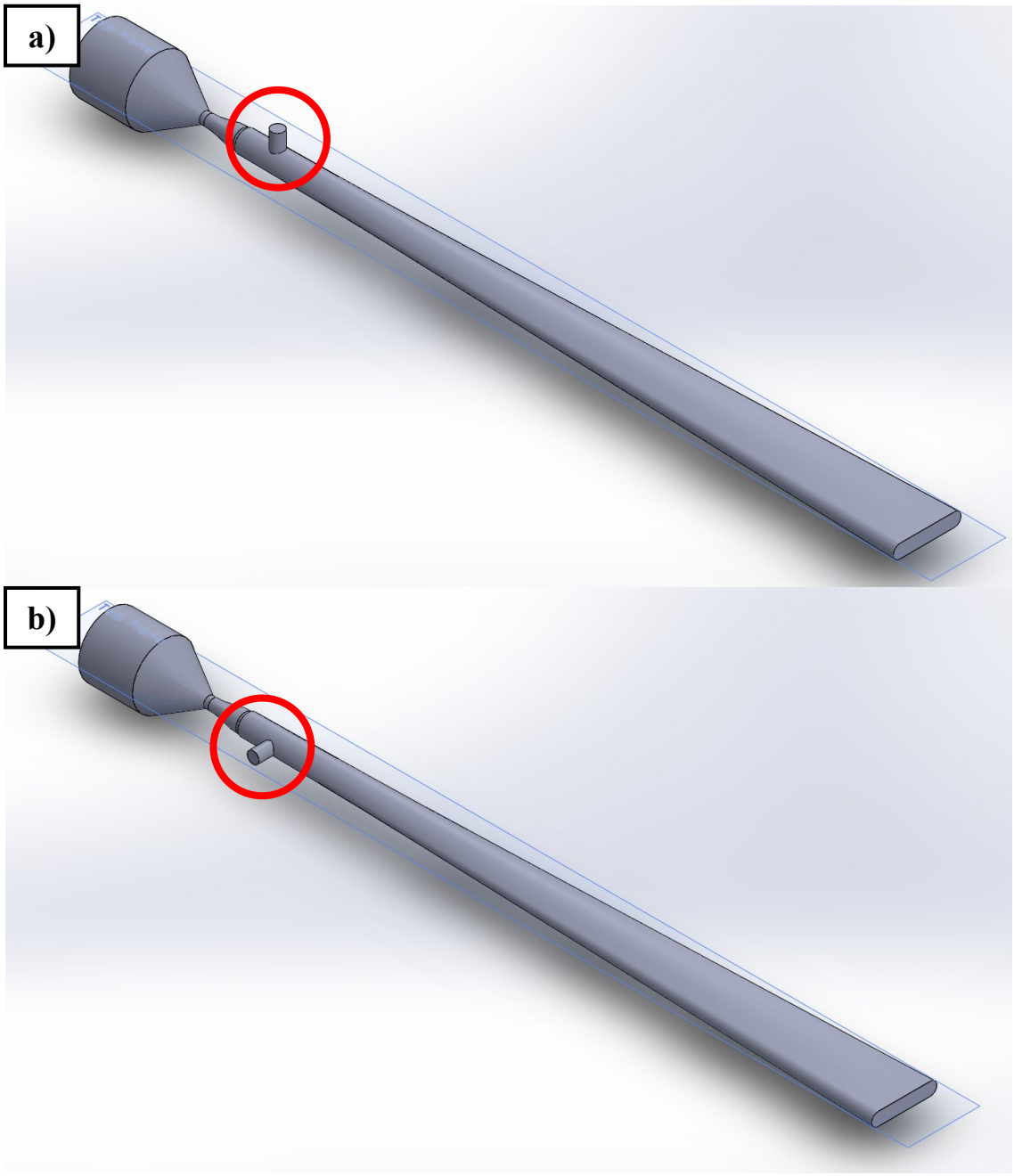

Figure 5.10 – Comparison of powder injection points, with reference plane visible, for a) original injection point (90°) vs. b) new injection point (0°)

To evaluate the effect of the new inlet position, a new simulation was performed. This new simulation uses the updated CAD model as the computational domain, which has the inlet at the 0° position as shown Figure 5.10b. Only the location of the powder inlet was

changed, all other dimensions are identical to the WC nozzle simulation which had the inlet at the 90° position. Figure 5.11 shows the resulting converged flow, which is comparable to the results previously obtained with the WC nozzle simulation (90° inlet). However, the powder inlet being placed on the side (0° angle) has a greater effect on the flow than in its previous position. As shown in Figure 5.11, the core of the flow is pushed closer to one of the nozzle walls (seen in the top view), and the effect is still observed in the wake of the shockwave.

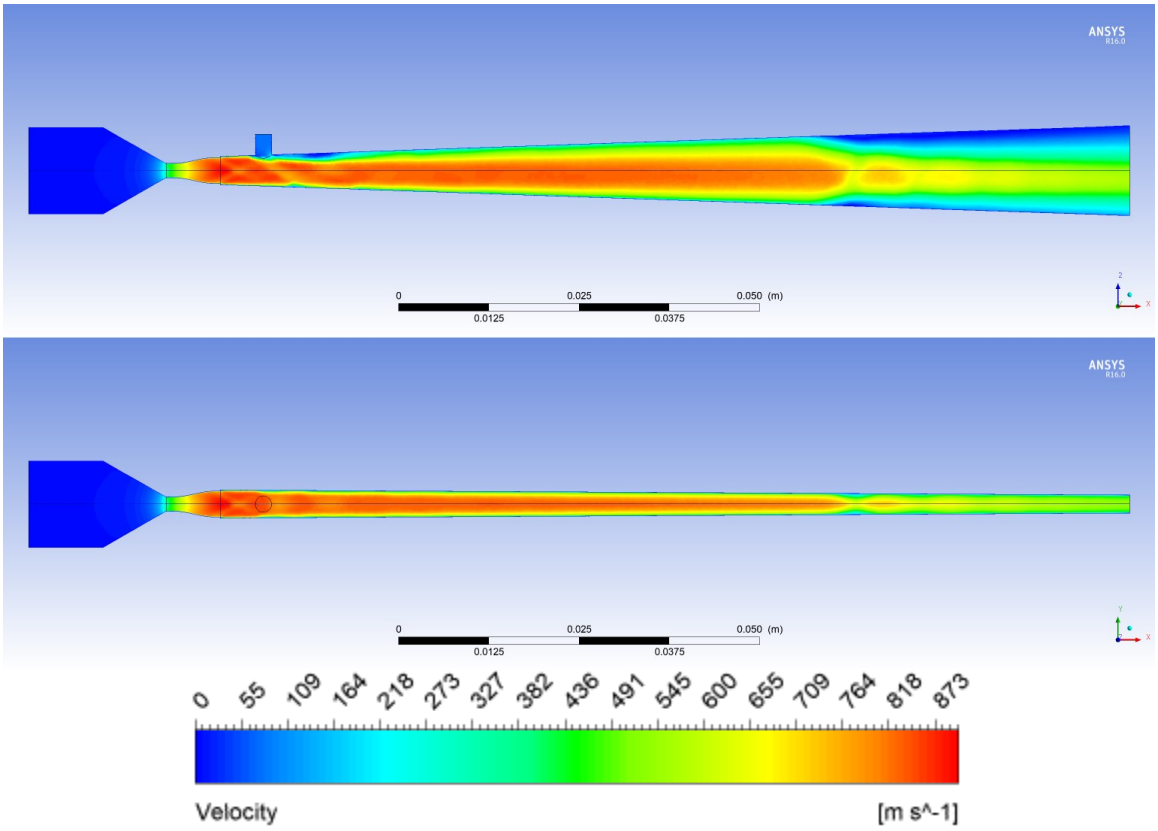

Figure 5.11 – 0° inlet velocity results, top view (top) and side view (bottom)

Particles were then injected through the 0° inlet using DPM and the same parameters as for the 90° inlet used in the previous simulation, for the WC nozzle. Figure 5.12 shows the resulting particle distribution for the full range of particle sizes. The injection point, which is upstream of the nozzle, is indicated by a black arrow.

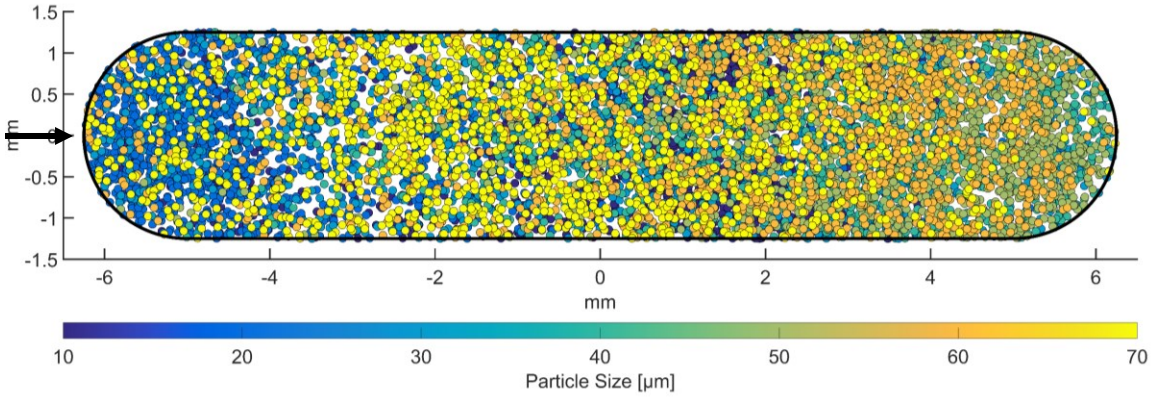

Figure 5.12 – Full particle distribution at nozzle exit plane when using a side (0°) injection location. Particle diameters range from 10 to 70 µm. The upstream inlet position is shown by a black arrow

When compared with the WC nozzle's original injection point (90°), the 0° injection clearly provides a much fuller particle coverage at the nozzle exit plane, with particles completely filling the nozzle. However, it can be seen in Figure 5.12 that the distribution is uneven with regards to particle sizes. When separating the result by particle sizes, the uneven distribution is clearly shown. For example, Figure 5.13a shows the location of 20 µm particles at the nozzle outlet, and demonstrates that most particles of this diameter are exiting the nozzle on the right side. Similarly, Figure 5.13b shows the distribution of 50 µm particles at the nozzle outlet. These are also poorly distributed, mostly exiting the nozzle on the left side.

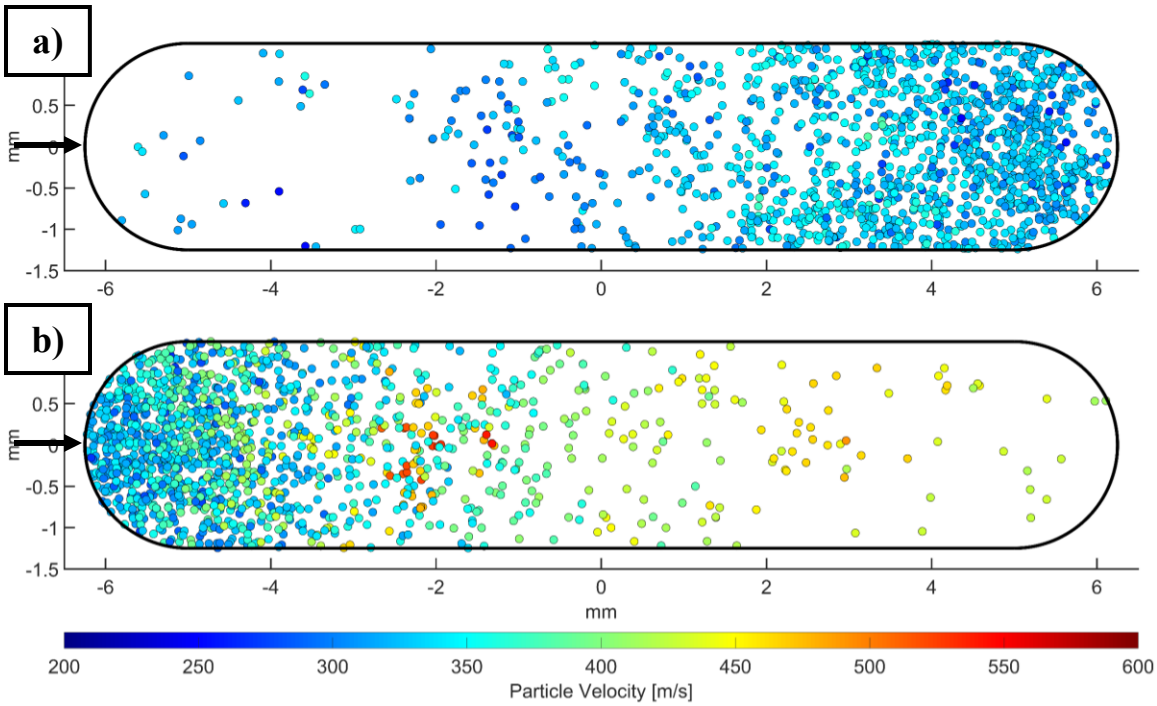

Figure 5.13 – Particle positions at the nozzle exit plane when using the 0° inlet position for a) 20 µm and b) 50 µm. The upstream inlet position is shown by a black arrow

Optimally, all particle sizes should be well distributed within the nozzle to ensure adequate adhesion to the substrate, as well as an even thickness across the width of the coating. Since the velocity of a particle at the nozzle exit can very significantly due to its size, and that the critical velocity for different particle sizes varies [59], [60], an even distribution at the nozzle exit for each particle diameter will increase the chances of obtaining a uniform coating thickness. From these results it is predicted that the 0° inlet position would produce a non-uniform coating. Despite the particles filling the nozzle exit (Figure 5.12), each particle size is only covering a part of the nozzle (Figure 5.13).

In order to resolve this issue, other injection angles were tested. Since the 0° powder inlet showed a significant difference in particle distribution compared to the original 90° inlet, it was hypothesized that other injections points could further promote the spreading of the particles within the nozzle through different interactions between the particles and nozzle walls. The angles tested were 15, 30, and 45 degrees with regards to the horizontal plane. Angles of 45 degrees and under were chosen as it was clear that the 0° inlet provided a

fuller distribution at the nozzle exit. Angles close to 0° should therefore provide a similar distribution.

Figure 5.14 shows the resulting gas velocity field when using the 15° powder inlet. As previously seen with the 0° inlet (Figure 5.11), the core of the flow is once again skewed due to the effect of the secondary flow entering from the powder inlet. Otherwise, the gas flow result is similar to the one obtained with the 0° inlet. The flow is accelerated as it passes through the converging-diverging nozzle, reaching velocities up to approximately 900 m/s. As the gas accelerates, its pressure and temperature decrease. Past the shockwave, the flow decelerates, and temperature rises. The pressure also rises as a result of the shockwave, so that the pressure at the nozzle exit will match the ambient pressure to satisfy the boundary condition.

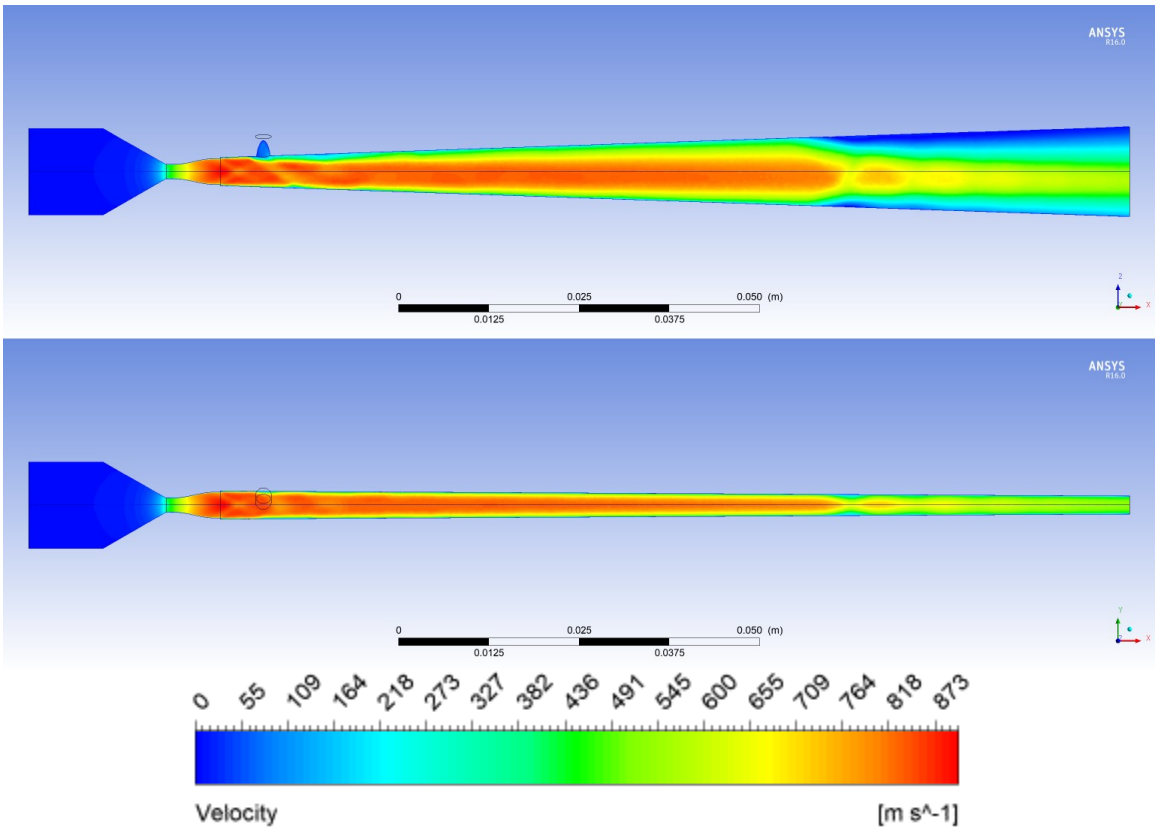

Figure 5.14 – 15° inlet, flow velocity results as seen from the top view (top) and side view (bottom)

Figure 5.15 shows the resulting gas flow for the 30° powder inlet. These results are nearly identical to the 15° inlet flow results (Figure 5.14), the 30° position does not have a

significant effect on the gas flow. Its effect on the flow is limited to the area near the powder inlet.

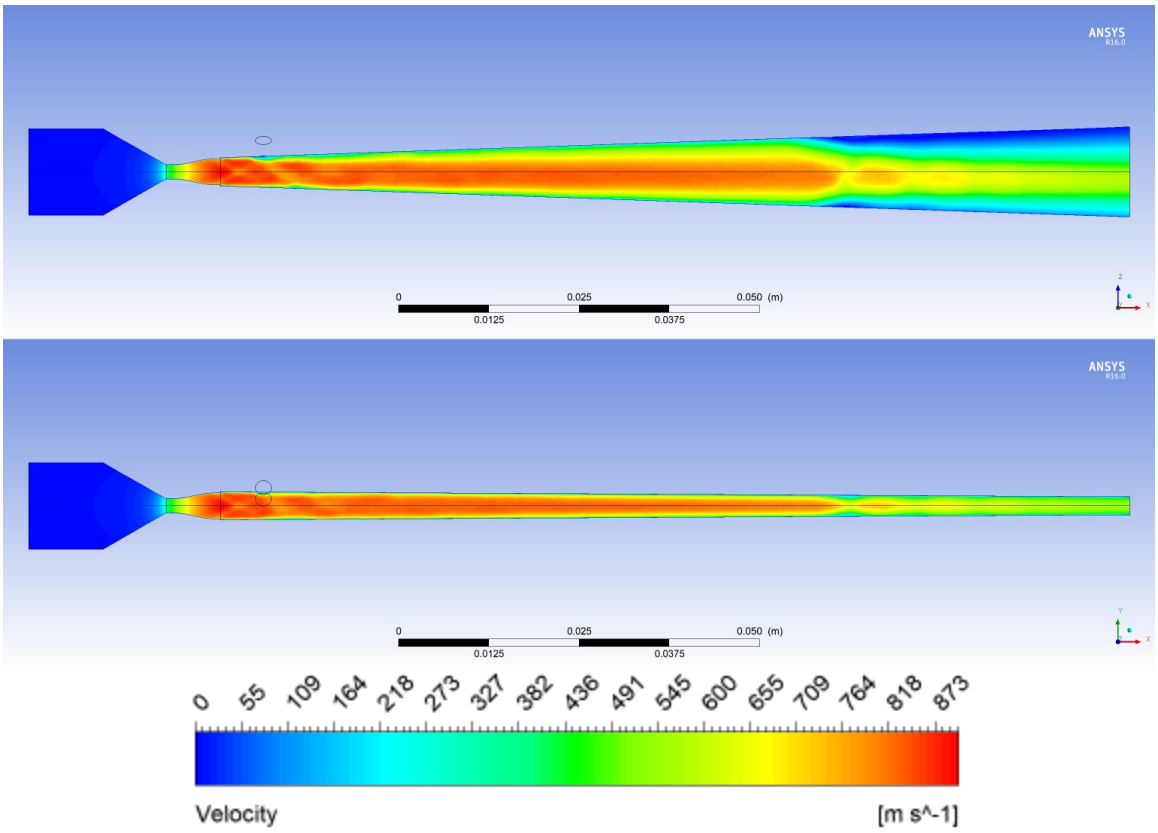

Figure 5.15 – 30° inlet, flow velocity results as seen from the top view (top) and side view (bottom)

Figure 5.16 shows the resulting gas flow for the 45° powder inlet. These results are once again nearly identical to the previous angles of 0, 15, and 30 degrees (Figure 5.11, Figure 5.14, and Figure 5.15, respectively). The effect of 45° position on the flow is limited to the area near the powder inlet.

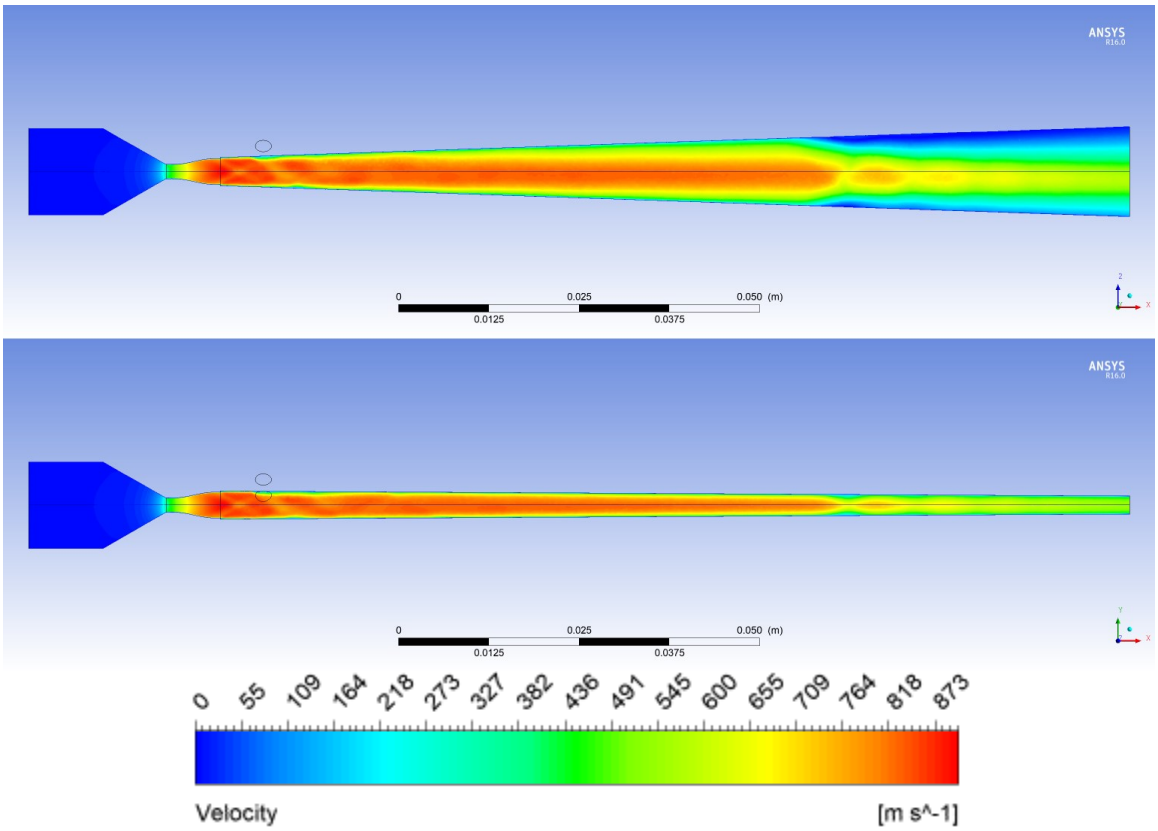

Figure 5.16 – 45° inlet, flow velocity results as seen from the top view (top) and side view (bottom)

Figure 5.17 shows the particle distribution at the exit plane for the three angled inlet cases (15, 30, and 45 degrees). When compared to Figure 5.12, which showed the distribution for the 0° inlet, it can be seen that the overall particle distribution gets pushed further towards the center of the nozzle as the injection angle increases.

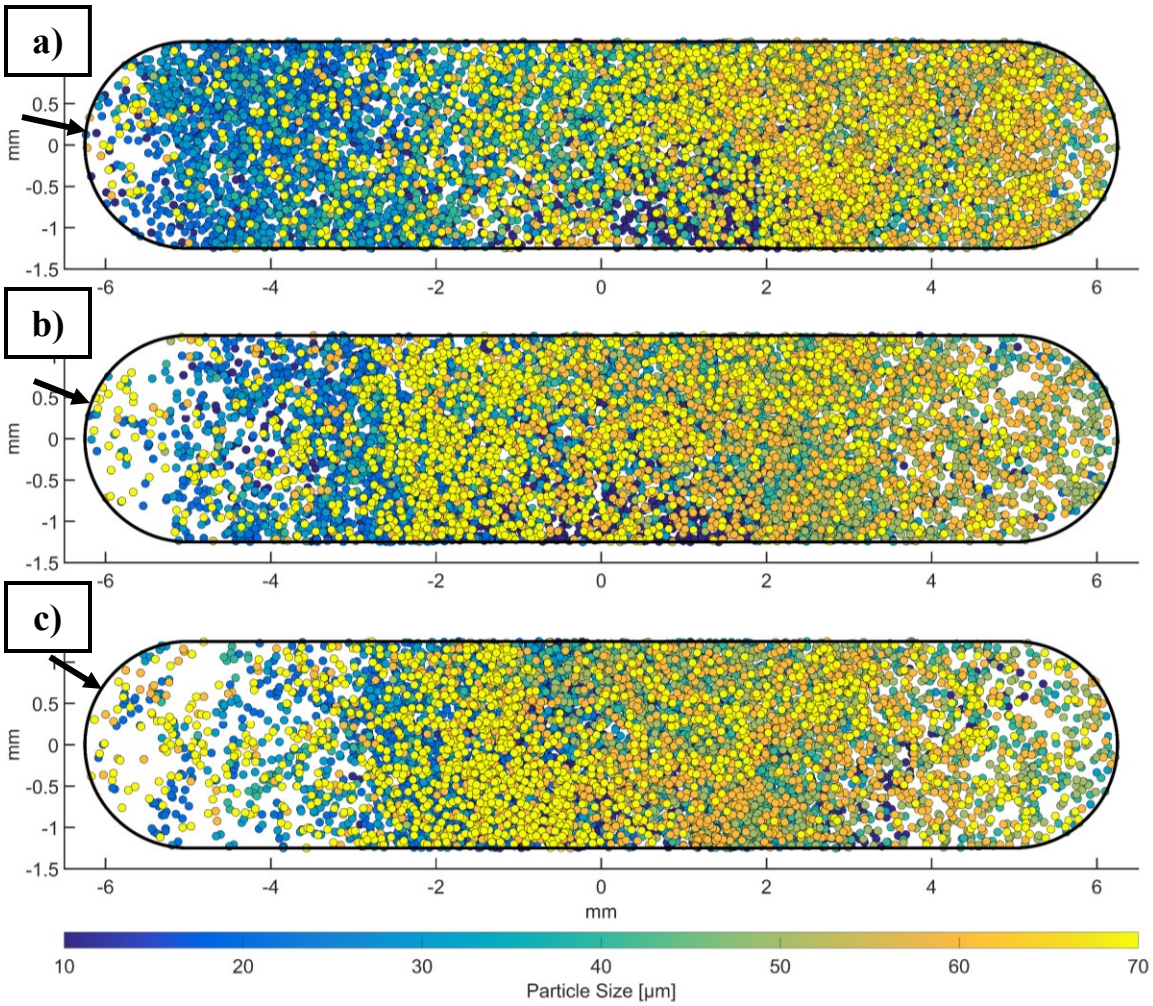

Figure 5.17 – Particle positions at the nozzle exit plane when using different angled inlets; a) 15°, b) 30°, c) 45°. The upstream inlet positions are shown by black arrows

However, as observed in Figure 5.17, the 15° inlet is the most favorable of these three inlets. The coverage of the outlet when using the 15° powder inlet is similar to the coverage provided by the 0° inlet (Figure 5.12). In other words, particles cover the entirety of the nozzle outlet.

When increasing the angle to 30° however, the left side of the outlet clearly shows less particles, as shown in Figure 5.17b. The right side of the nozzle is also less dense, showing that there are less particles in this section than in the 15° case.

When the angle is further increased to 45°, the effect is aggravated. Figure 5.17c clearly shows that the left side of the nozzle has a decreased number of particles compared to the 15° and 30° cases. The same thing is seen on the right side of the nozzle, although to a

lesser degree. This seems to indicate that as the angle is increased, the particle distribution is further pushed towards the center portion of the nozzle. For this reason, the 15° inlet is further discussed in this section as it seems to be the most promising of these angles. Note that the particle distribution results of each nozzle injection point, and for every particle diameter, are shown in Appendix B.

Figure 5.18 shows the position of 20 and 50 µm particle diameters at the nozzle exit plane for the 15° inlet, similarly to Figure 5.13 which showed the distributions for the 0° inlet. When comparing the two inlet positions, it is observed that the distribution is still skewed in the case of the 15° inlet when looking at the particle sizes separately, and the change in position has had little effect on the distribution at the outlet.

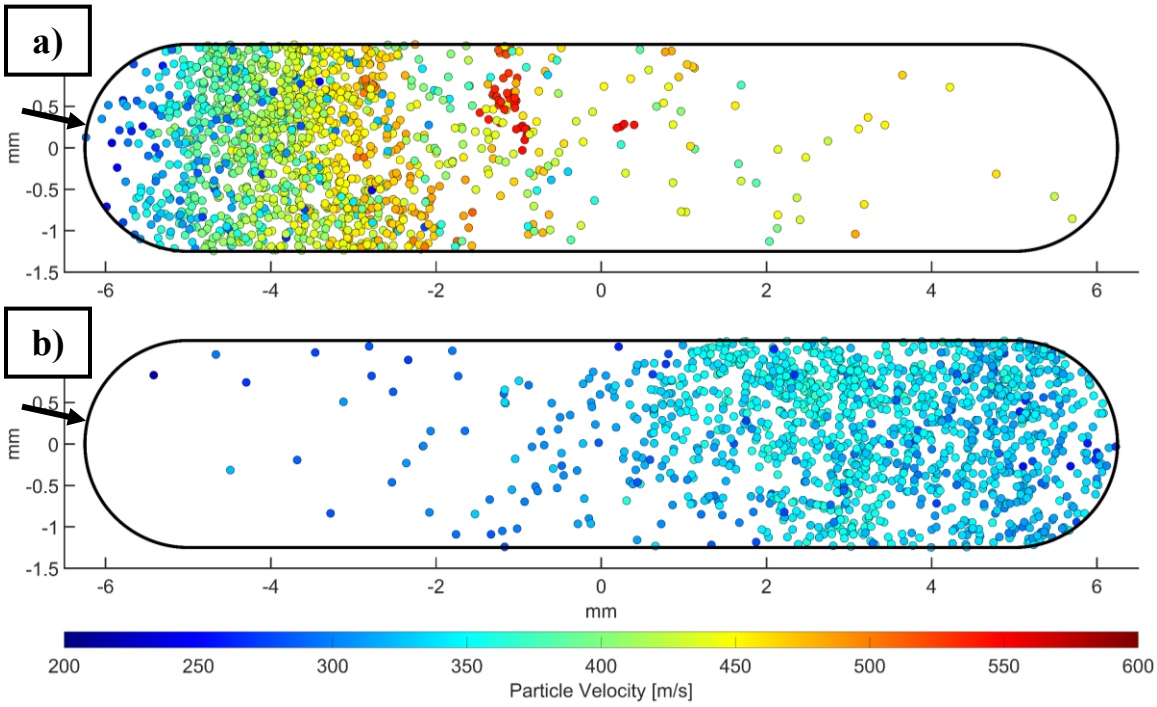

Figure 5.18 – Particle positions at the nozzle exit plane when using the 15° inlet position for a) 20 µm and b) 50 µm particles. The upstream inlet position is shown by a black arrow

Injecting at a 15° angle did not fully resolve the issue of particle distribution. While the overall particles cover the nozzle exit, individual sizes are still poorly distributed. The 15° inlet shows very little improvement in this regard compared to the 0° inlet. However, the new inlet positions did promote the bouncing of particles against multiple walls within the nozzle, as demonstrated by Figure 5.19. This is good, as the bouncing is what helps to

spread the particles within the nozzle, due to their different impact points with the walls. This figure shows the path and velocity of five 60 µm particles within the nozzle to demonstrate that the particle bounces multiple times against many walls of the nozzle. Note that the particle-wall interactions result in different positions for each particle despite having the same diameter.

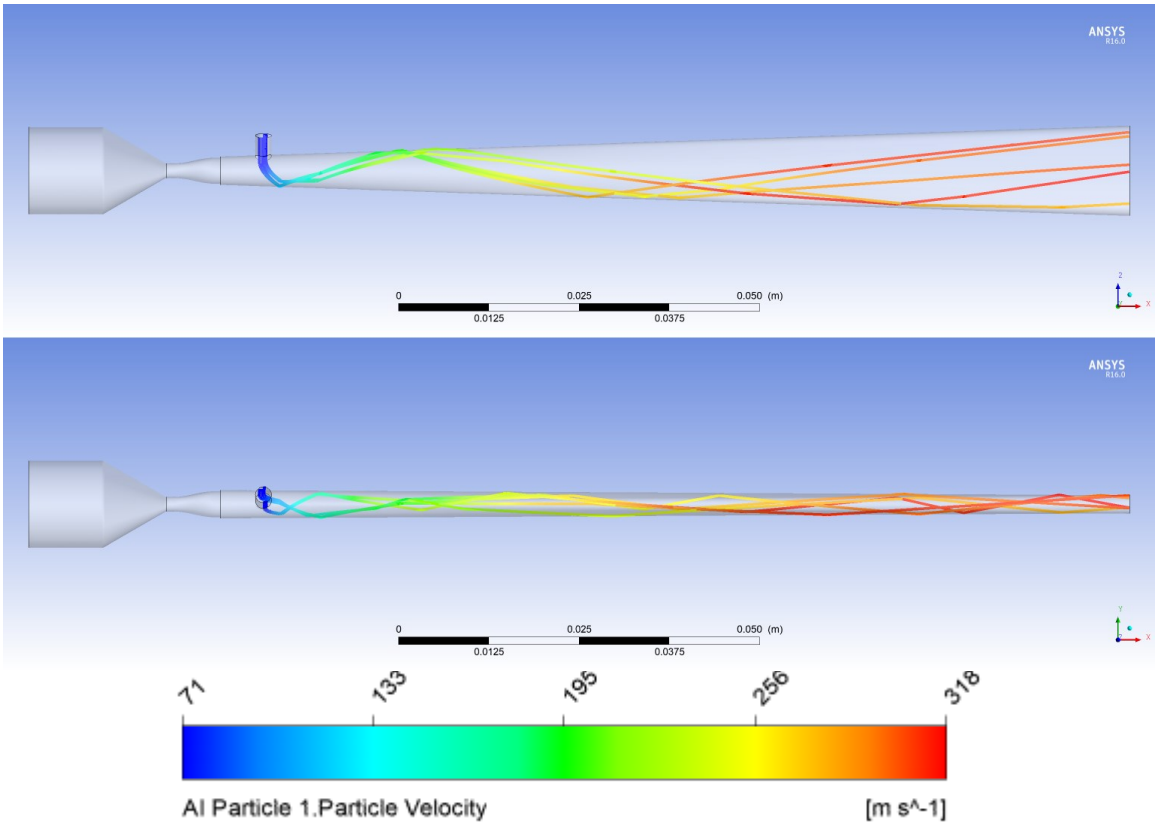

Figure 5.19 – Path and velocity of five 60 µm particles injected with the 15° inlet

The results have shown very little difference between the 0° and 15° inlets in terms of gas flow and particle distribution at the nozzle outlet. With this information, it is difficult to decide which inlet would produce a more uniform coating and should be used for a prototype. In theory, however, particles injected through a 0° inlet will only have a radial velocity in one axis (i.e. z-axis) when reaching the main flow, whereas particles injected through a 15° inlet will have a radial velocity in two axes (z-axis and y-axis). This should provide more bouncing against all nozzle walls as particles are pointed directly towards the flat nozzle wall. Since the interactions with nozzle walls help to distribute and redirect

particles, as demonstrated in Figure 5.19, the 15° inlet was selected for the prototype design.

5.4 PBI NOZZLE PROTOTYPING

As discussed in Section 5.2, the road to developing a new prototype nozzle consists of two pillars; the improvement of the powder distribution by optimizing injection location, and minimizing the impact of nozzle clogging through the use of different materials.

A first prototype was drafted through CAD software to implement the new 15° inlet position. This prototype has the powder inlet at the 15° position as it seemed to provide a fuller particle coverage at the nozzle outlet through the simulations shown previously. This aims to resolve the first issue found with the WC prototype, the particle distribution. The obround shape is identical as the one previously used by Technoform for the WC nozzle prototype, no changes were made to the dimensions or shape. The new nozzle prototype is shown in Figure 5.20.

Figure 5.20 – CAD model of the initial angled (15°) injection obround prototype

The aim was to make this new nozzle out of PBI to alleviate the clogging issue, thus addressing the second problem with the WC prototype. However, Centerline (Windsor) Ltd. was unable to manufacture the obround inner profile using the manufacturing equipment they currently have access to. After extensive research on manufacturing techniques, it seemed that the best way to produce this nozzle was through thermoset injection molding. However, the start-up costs for injection molding are high due to the cost of the mold. Furthermore, the minimum order needed for the manufacturer to consider retooling and producing the nozzle was on the order of thousand of units. At this point, it was clear that the design needed further iterations in order to be manufactured for a prototype run.

The design was modified in order to split the nozzle into two halves, which would allow the inside profile to be machined easily. However, the nozzle needs to be sealed appropriately once the two halves are assembled, to prevent the propellant gas from escaping through the micro-gaps between the two halves. To accomplish this, a supplemental part named the nozzle “sleeve” was designed. The aim was to assemble the two PBI halves, then press-fit them into the nozzle sleeve to effectively seal the nozzle. To maintain compatibility with the Centerline (Windsor) Ltd. commercial system, the PBI halves were thinned down so that the dimensions of the fully assembled nozzle would be identical to Centerline’s commercial nozzles and the WC prototype. This change did not affect the inner channel of the nozzle, which kept the exact dimensions of the WC prototype. Figure 5.21a shows the two PBI halves manufactured by Boedeker Plastics Inc (Texas, United States) in their as-received state before assembly. Figure 5.21b shows the aluminum sleeve that is used to seal the two nozzle halves.

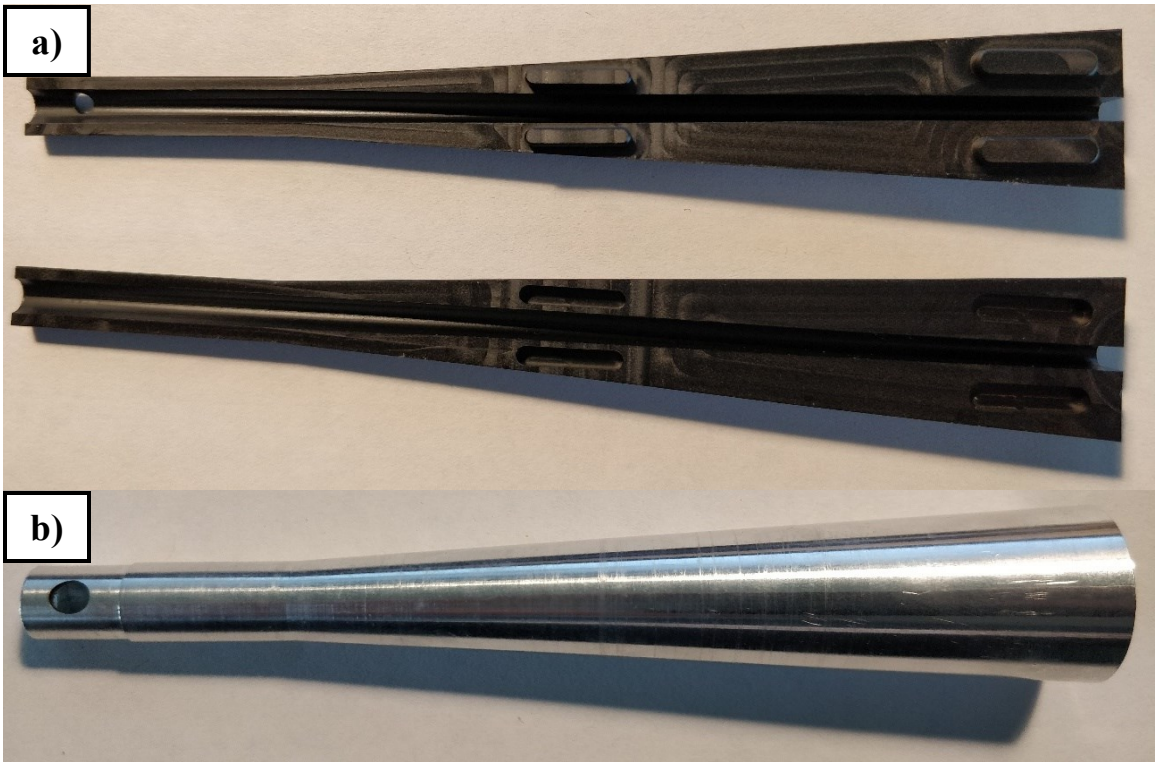

Figure 5.21 – Prototype parts for the 15° powder injection PBI nozzle, a) PBI nozzle halves, as-received, and b) aluminum sleeve, as-received

The pins and holes on the PBI halves are designed to align the two pieces, and the static friction holds them together until the sleeve is fitted. The assembled PBI piece was slowly pressed into the aluminum sleeve using a hydraulic press. Figure 5.22 shows the fully assembled prototype once assembled with the commercial nozzle holder from Centerline (Windsor) Ltd.

Figure 5.22 – Assembled PBI prototype nozzle, with Centerline (Windsor) Ltd. holder

5.5 ANGLED INLET EXPERIMENTAL RESULTS

Initial tests were performed with the PBI prototype to compare it to the WC prototype, considering the difference in nozzle material and injection point. The first spray was done using the same parameters as for the WC nozzle (Table 5.1), as shown in Table 5.2.

Table 5.2 – CGDS parameters for initial testing of the PBI prototype (15° inlet)

Pressure [MPa]	*Temperature [°C]*	*Stand-off distance [mm]*	*Traverse speed [mm/s]*	*Powder feeding [g/min]*	*Number of passes*	*Injection gas flow rate [kg/s]*
2.07 (300 psi)	300	10	15	8.2	1	3.26×10^{-4} (30 SCFH)

The resulting coating from this spray is shown in Figure 5.23. The single-pass coating width has been measured using the built-in measurement tool on the 3D digital microscope. When compared to the spray done with the WC nozzle (Figure 5.4) and identical parameters, it can be seen that the coating deposition is marginally wider, going from approximately 6.5 mm to 7.5 mm. The full particle impact width is also slightly wider, going from 12.67 mm to approximately 13.3 mm. However, the coating is not centered in this case. Figure 5.23 shows clearly that the deposited coating is skewed to the left of the image, and not centered with the region of the substrate that was impacted by particles. Please note that side-by-side images of all relevant spray comparisons are available in Appendix A for convenience.

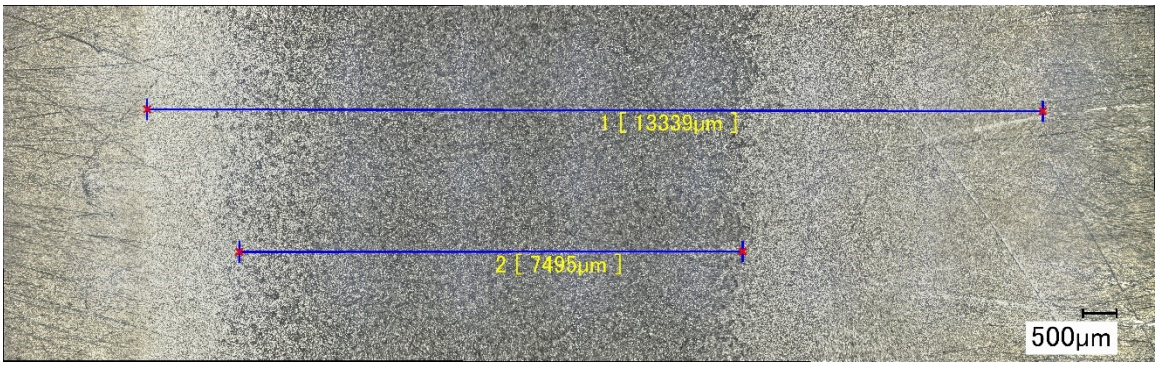

Figure 5.23 – Coating deposited with the initial PBI prototype (15° inlet), using parameters from Table 5.2

The skewed effect is most likely caused by the uneven particle size distribution created by injecting the particles at the 15° position. However, many particle impacts and craters are seen outside of the deposited aluminum coating, for a total width of 13.3 mm. As this is wider than the nozzle outlet width of 12.5 mm, it indicates that particles are covering the entire nozzle outlet, but the uneven size distribution predicted by the simulations causes an uneven deposition. As previously discussed, not all particles will be deposited due to their different impact velocities causes by lower gas velocities near the nozzle edges, and also due to different particle sizes. It is also worth noting that the substrate surface shows more craters outside of the deposited coating than in the case of the WC nozzle. This indicates that more particles have impacted the surface when using the PBI prototype, which shows that particles are covering the full nozzle exit as predicted by the simulations.

Another contributing factor to the uneven coating could be the new nozzle material. *MacDonald et al.* have previously shown that nozzle material can have a significant effect on deposition efficiency [66]. They have hypothesized that the thermal diffusivity of the nozzle material affects the deposition efficiency. The change in deposition efficiency was attributed to the fact that a nozzle with a lower thermal diffusivity will transfer less heat to the particles, thus resulting in a lower particle temperature at the moment of impact with the substrate [66]. If the particle temperature is low, there is less thermal softening and therefore less deformation on impact. When particles deform poorly, they do not adhere well to the substrate, hence the low deposition efficiency. The thermal diffusivity of the PBI polymer (0.023 mm^2/s) is lower than that of the WC ceramic (21 mm^2/s). Thus, it is possible that the deposition efficiency is lowered in part due to the PBI nozzle walls.

To compensate for the lower deposition efficiency of the PBI nozzle, a second set of coatings was deposited. For these coatings, the sprays would consist of multiple passes over the same section of the substrate instead of a single pass. This was done to see the full potential width of the coatings, when more particles have been deposited as a result of the multiple passes. Identical parameters were used for the PBI and WC nozzles. These parameters are shown in Table 5.3. The values for the pressure, temperature, and stand-off distance are taken from Technoform's process parameters. Traverse speed, powder feed rate, and number of passes were adjusted accordingly to obtain a thick coating. Note that the powder feed rate here as been reduced by approximately half compared to previous parameters (Table 5.1 and Table 5.2), to avoid producing excessively thick coatings.

Table 5.3 – CGDS parameters for comparison of thick coatings produced by the WC (90° inlet) and PBI (15° inlet) prototypes

Pressure [MPa]	*Temperature [°C]*	*Stand-off distance [mm]*	*Traverse speed [mm/s]*	*Powder feeding [g/min]*	*Number of passes*	*Injection gas flow rate [kg/s]*
1.21 (175 psi)	300	15	5	4.5	5	3.26×10^{-4} (30 SCFH)

Three-dimensional profiles of the resulting coatings are shown in Figure 5.24a and Figure 5.24b for the WC and PBI nozzles, respectively. It can be seen that the PBI nozzle seems to be skewed once again. It also produced a much thinner coating when compared to the WC nozzle. This is again indicative of the difference in deposition efficiency due to the nozzle material.

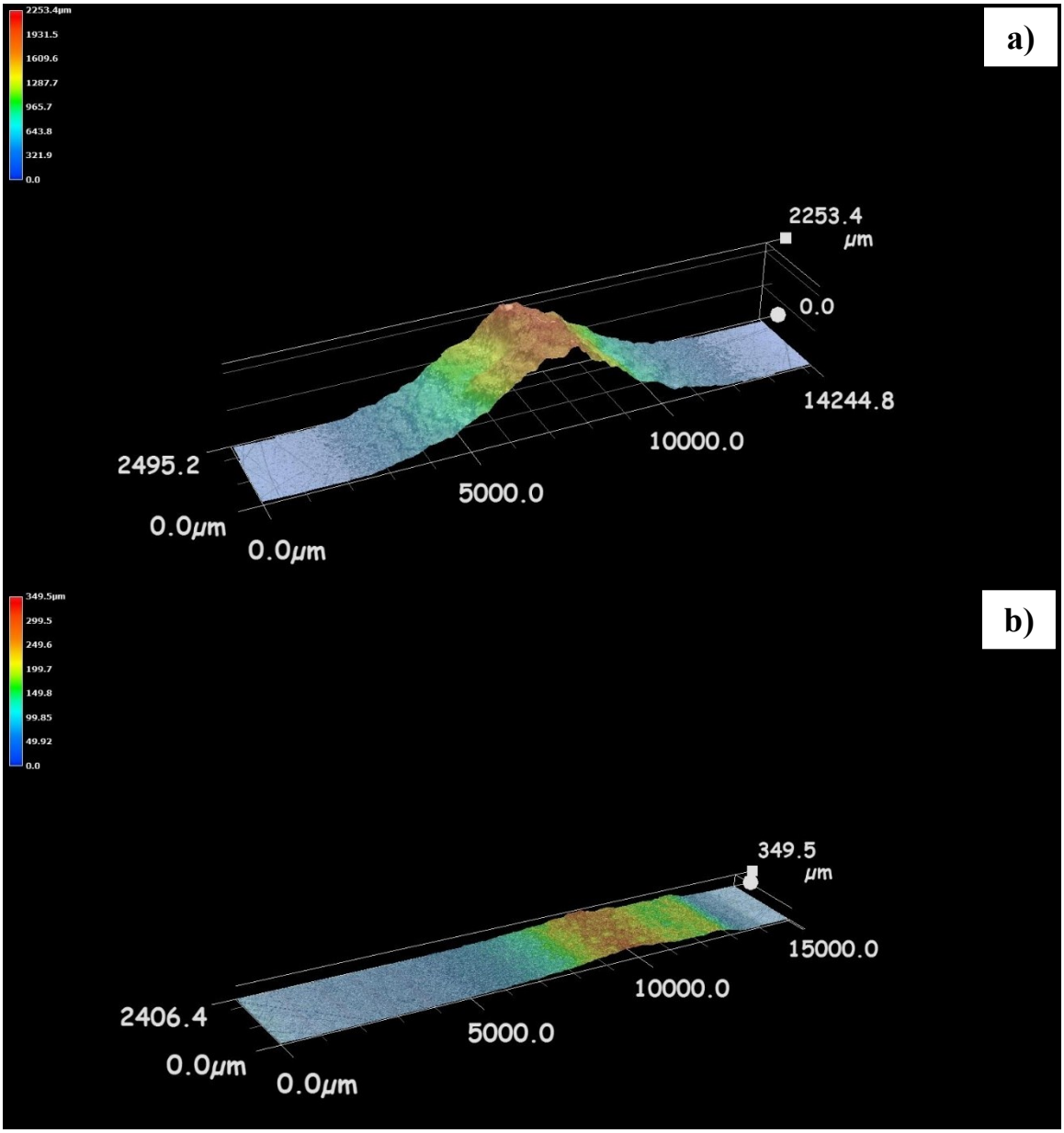

Figure 5.24 – 3D profile of multi-pass coatings deposited using parameters from Table 5.3, a) WC nozzle (90° inlet), and b) PBI nozzle (15° inlet)

However, due to the PBI material used in the new prototype, the process temperature can be increased. As previously stated, the PBI reduces the clogging potential [46], [66], so the temperature can be increased without worrying about the nozzle clogging quickly. Therefore, another coating was produced with the PBI nozzle but with increased temperature to counteract the lower deposition efficiency of the PBI material. The new parameters are shown in Table 5.4.

Table 5.4 – Revised CGDS parameters for thick coatings produced by the PBI prototype (15° inlet)

Pressure [MPa]	*Temperature [°C]*	*Stand-off distance [mm]*	*Traverse speed [mm/s]*	*Powder feeding [g/min]*	*Number of passes*	*Injection gas flow rate [kg/s]*
1.21 (175 psi)	500	15	5	4.5	5	3.26×10^{-4} (30 SCFH)

The increased temperature significantly increased the thickness of the coating produced by the PBI nozzle when compared to the previous trial. The thickness obtained when using 500°C with the PBI nozzle is comparable to the thickness previously obtained with the WC nozzle at 300°C. However, the thick coating is still skewed to one side in the case of the PBI nozzle, as shown by the three-dimensional profile in Figure 5.25, which is not desirable as it does not fulfill Technoform's requirements.

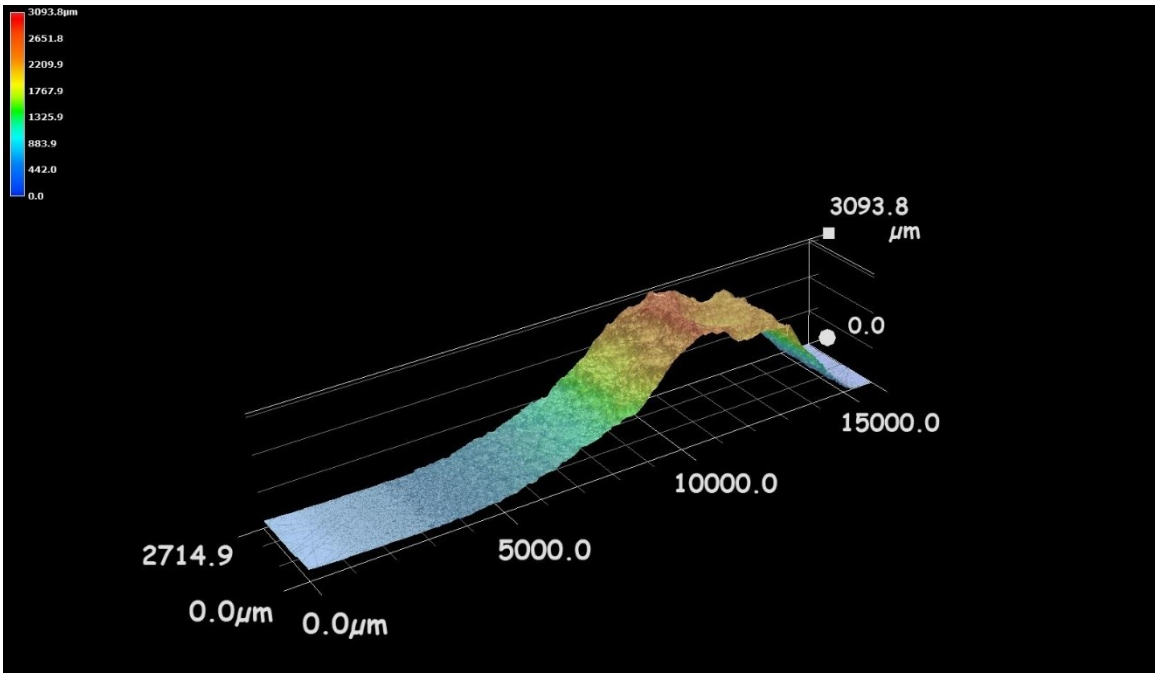

Figure 5.25 – 3D profile of multi-pass coating deposited using the PBI prototype (15° inlet) and parameters from Table 5.4

Simulations have showed that multiple particle sizes were situated only in one half the nozzle when reaching the outlet. The experimental tests showed that this results in a deposited coating that is skewed; it is not centered with the nozzle outlet, but rather slightly offset to one side.

If the 15° inlet was moved to be positioned on the other side of the nozzle, the same pattern should be expected as the nozzle geometry is otherwise symmetrical. This should therefore result in the opposite particle distribution. Particles that were previously on the left-hand side of the nozzle when reaching the outlet should now be on the right-hand side, and vice versa. When spraying, the deposited coating should then be skewed in the opposite direction as it was previously.

Figure 5.26 shows the predicted 50 µm particle distribution at the nozzle outlet for a nozzle with dual 15° powder inlets. This figure was obtained by mirroring the 50 µm particle distribution of the 15° inlet, shown previously in Figure 5.18b. It is not the result of CFD modelling, only a mirrored image of previous results. It represents the potential distribution of 50 µm particles that could be obtained by adding a second 15° powder inlet. The positioning of this second inlet is shown by the orange arrow in Figure 5.26. The predicted

50 µm particle distribution at the outlet resulting from the second inlet are shown by the faint particles on the left side of the figure.

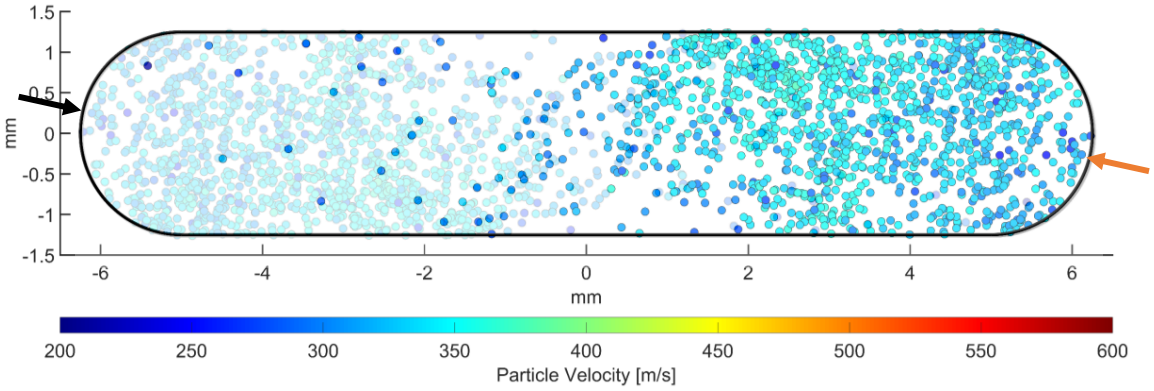

Figure 5.26 – Predicted 50 µm particle distribution resulting from adding a second 15° powder inlet. The original 15° inlet position is shown by a black arrow, and the new position is shown by an orange arrow

5.6 DUAL INJECTION SIMULATIONS

The dual injection approach was first tested through modeling. While Figure 5.26 showed a prediction of the outcome, it was simply a mirrored image. A full simulation was performed to take into account any differences in the flow that could occur from adding a second powder inlet, and to simulate both particle injections with the random walk model.

A new CAD model was created with a mirrored 15° inlet, as show in Figure 5.27. The new inlet is identical to the one previously used, and the boundary conditions used are also the same.

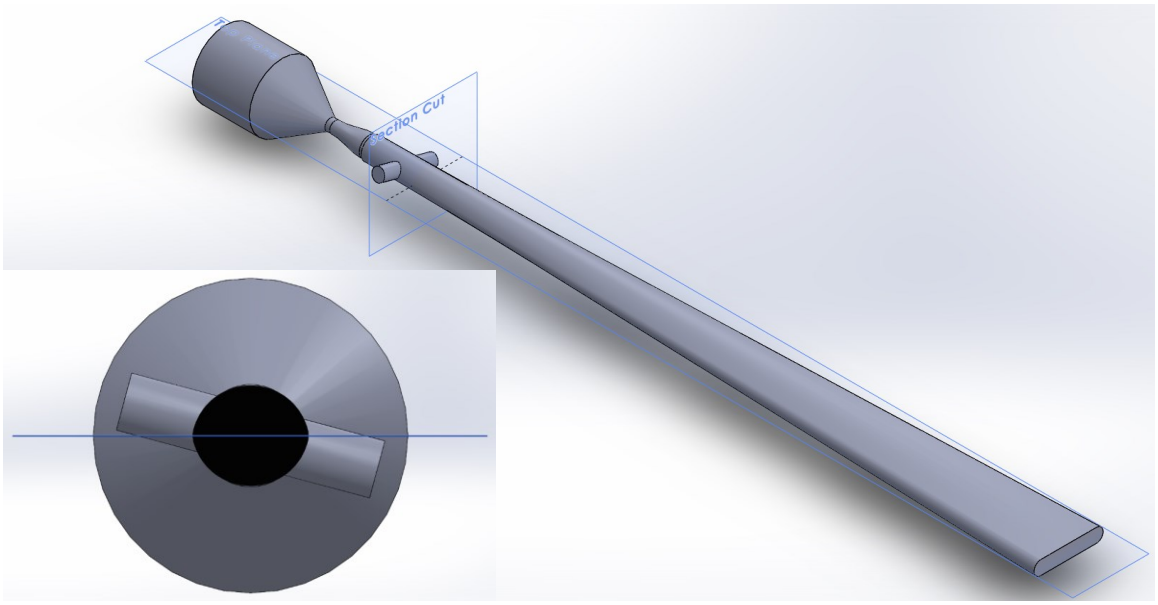

Figure 5.27 – Dual inlet CAD model with cross-sectional view, showing the 15 ° powder inlet positions

The velocity field of the converged flow is shown in Figure 5.28. When compared to the single 15° inlet, it can be seen that the addition of the second powder inlet resolves the skewed gas flow and brings the core back to the middle of the nozzle. This is expected since both secondary flows from the powder inlets will enter the main gas flow opposite of each other, effectively cancelling each other's radial velocity. Otherwise, the gas flow behaves as expected. It accelerates as it goes through the converging-diverging nozzle, reaching supersonic velocities in the diverging section. The shockwave forms as seen I the previous simulations, and the flow slows past this shockwave. The shockwave position has not been significantly affected by the addition of a second powder inlet.

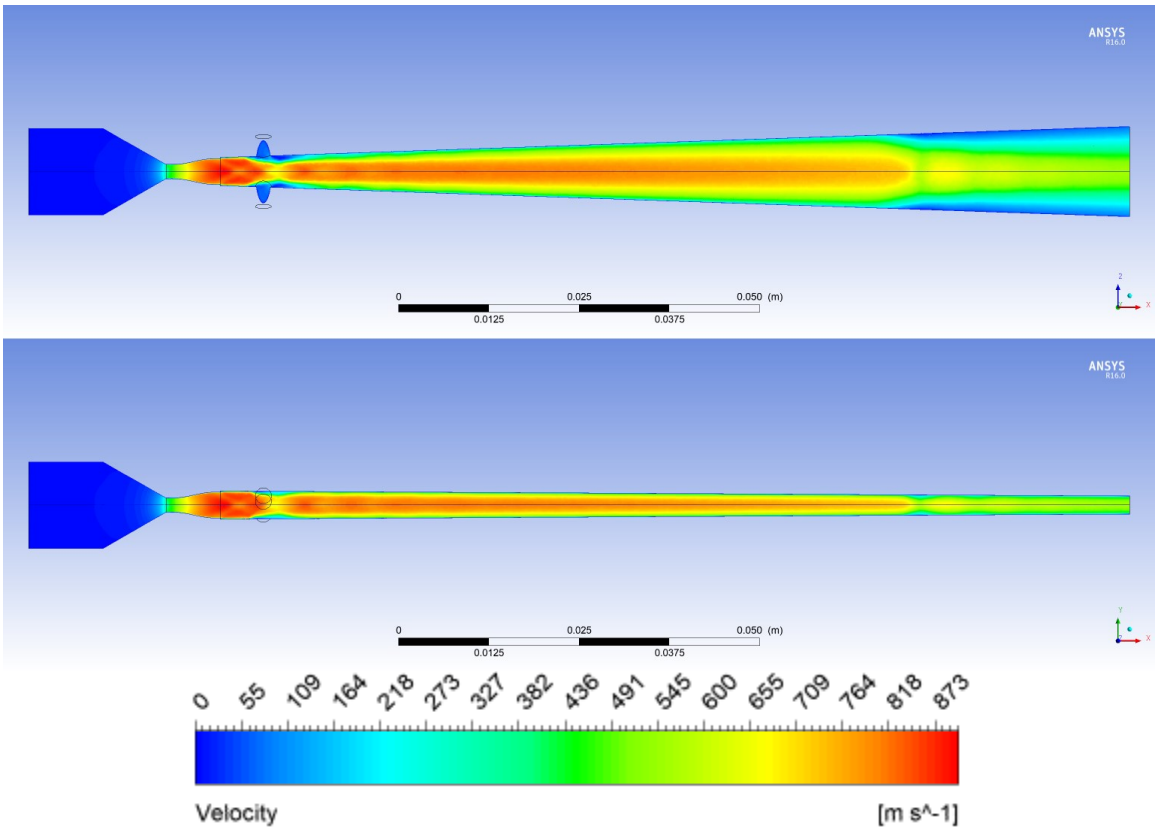

Figure 5.28 – Dual inlet velocity results, top view (top) and side view (bottom)

Figure 5.29 shows the resulting particle distributions of the 20 and 50 µm diameter particles at the nozzle outlet. In the case of the 20 µm particles, there is a noticeable gap in particles in the center of the nozzle. Due to their smaller size, these particles quickly lose their initial velocity which is in the radial direction. They lose the momentum needed to bounce against the nozzle walls multiple times, as they quickly accelerate in the axial direction due to the very high velocities of the main flow. In this case, the result is that this particle size is at the edges of the nozzle when reaching the exit, resulting in the lack of particles at the center. This effect was also previously seen by *Varadaraajan et al.* when using multiple radial injection points in a rectangular nozzle, where the center of the nozzle contained very few particles at the nozzle exit [42].

For the 50 µm particles in Figure 5.29b, the coverage is fairly even, with some regions showing slightly less particles. The result is similar to what was predicted previously in Figure 5.26. This demonstrates that the slight changes in the gas flow have not significantly

affected the particle distribution at the outlet. Distribution results for the other particle sizes are shown in Appendix B.

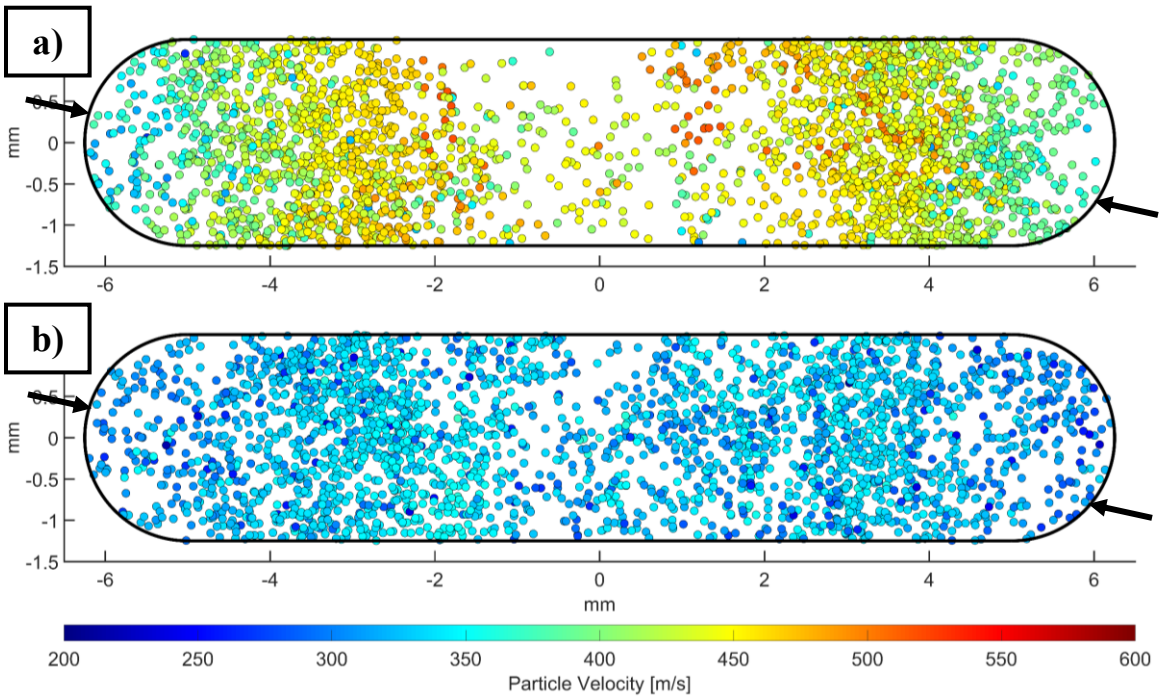

Figure 5.29 – Particle positions at the nozzle exit plane for the dual 15° inlets for a) 20 µm and b) 50 µm particles. The upstream inlet positions are shown by a black arrow

The overall distribution results were promising, showing that coverage for individual particle sizes has been improved compared to the single 15° injection. Despite the gap at the center of the nozzle for 20 µm particles, it was decided that the prototype should be modified following the dual 15° inlet design. By modifying the current PBI prototype, experimental results for a dual injection nozzle can be obtained quickly to determine if the deposition width is improved by adding the second 15° powder inlet.

5.7 Modified PBI Prototype

To modify the nozzle prototype for dual injection, a new powder injection hole was carefully drilled into the side of the nozzle through the aluminum and PBI layers. As the PBI is press fit into the nozzle, this was done in a single operation instead of attempting to disassemble the nozzle. A second powder inlet hole was successfully drilled across from the original 15° inlet. Figure 5.30 shows the new 15° inlet on the PBI prototype.

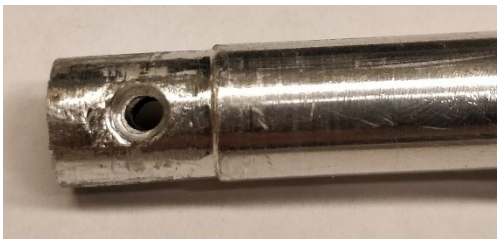

Figure 5.30 – Second powder inlet on the obround PBI nozzle prototype

In order to spray with the modified nozzle, a dual injection holder was also necessary. A dual injection variant of the commercially available nozzle holder was manufactured and provided by Centerline (Windsor) Limited. Images of these parts are displayed in Section 4.3.3.2. for reference. Figure 5.31 shows the complete assembly of the nozzle and nozzle holder, ready to be attached to the spray system.

Figure 5.31 – Complete dual injection nozzle assembly

Tests were performed to evaluate the dual injection performance. The spray parameters used for this test, shown in Table 5.5, are the same as for the previous sprays performed with the single 15° inlet. These parameters use the same pressure as Technoform, but have an increased temperature (from 300°C to 500°C) since the PBI nozzle can handle it without

clogging. The higher process temperature also increases the deposition efficiency as demonstrated earlier by the coatings in Figure 5.24b and Figure 5.25.

Before spraying with both injections simultaneously, each injection inlet on the prototype was tested individually to ensure everything was working. This also allows for a direct comparison between single and dual injection coatings. When using a single injection the feed rate was doubled, to obtain an equivalent total feed rate (~7.9 g/min) with the dual injection sprays, as shown in Table 5.5. Both powder feeders were connected to the nozzle to avoid gas leakage through the unused powder inlet. During the spray, one of the feeders is feeding powder while the other remains connected without feeding.

Table 5.5 – CGDS parameters for single injection testing on the dual injection PBI prototype (15° inlets)

Pressure [MPa]	*Temperature [°C]*	*Stand-off distance [mm]*	*Traverse speed [mm/s]*	*Powder feeding [g/min]*	*Number of passes*	*Injection gas flow rate [kg/s]*
1.21 (175 psi)	500	15	5	7.9	5	3.26×10^{-4} (30 SCFH)

Three-dimensional profiles of the resulting coating surfaces are shown in Figure 5.32. Figure 5.32a shows the profile resulting from the spray when injecting powder in the PPF only. The resulting profile is similar to the one obtained prior to the dual injection modification (Figure 5.25), which was expected.

Figure 5.32b shows the profile resulting from powder injection using the SPF only. The profile displays as similar trend as the one produced when only the PPF was used. The coating is skewed in the other direction, as predicted, since the injection inlet is on the opposite side of the nozzle.

While both coatings are similar, there are some discrepancies. The coating produced when feeding from the SPF is slightly different, it is not as thick and has a smoother slope. However, the SPF was connected to the second inlet hole, which was shown in Figure 5.30, and is not exactly the same as the original inlet on the single injection PBI prototype. The

differences between coatings where attributed to the differences between the two inlet points on the nozzle, since both powder feeders (PPF and SPF) had the same powder feed rate and gas flow rate. The powder feeders also had their connections switched to ensure that the difference was caused by the inlet points on the nozzle, and not the feeders themselves.

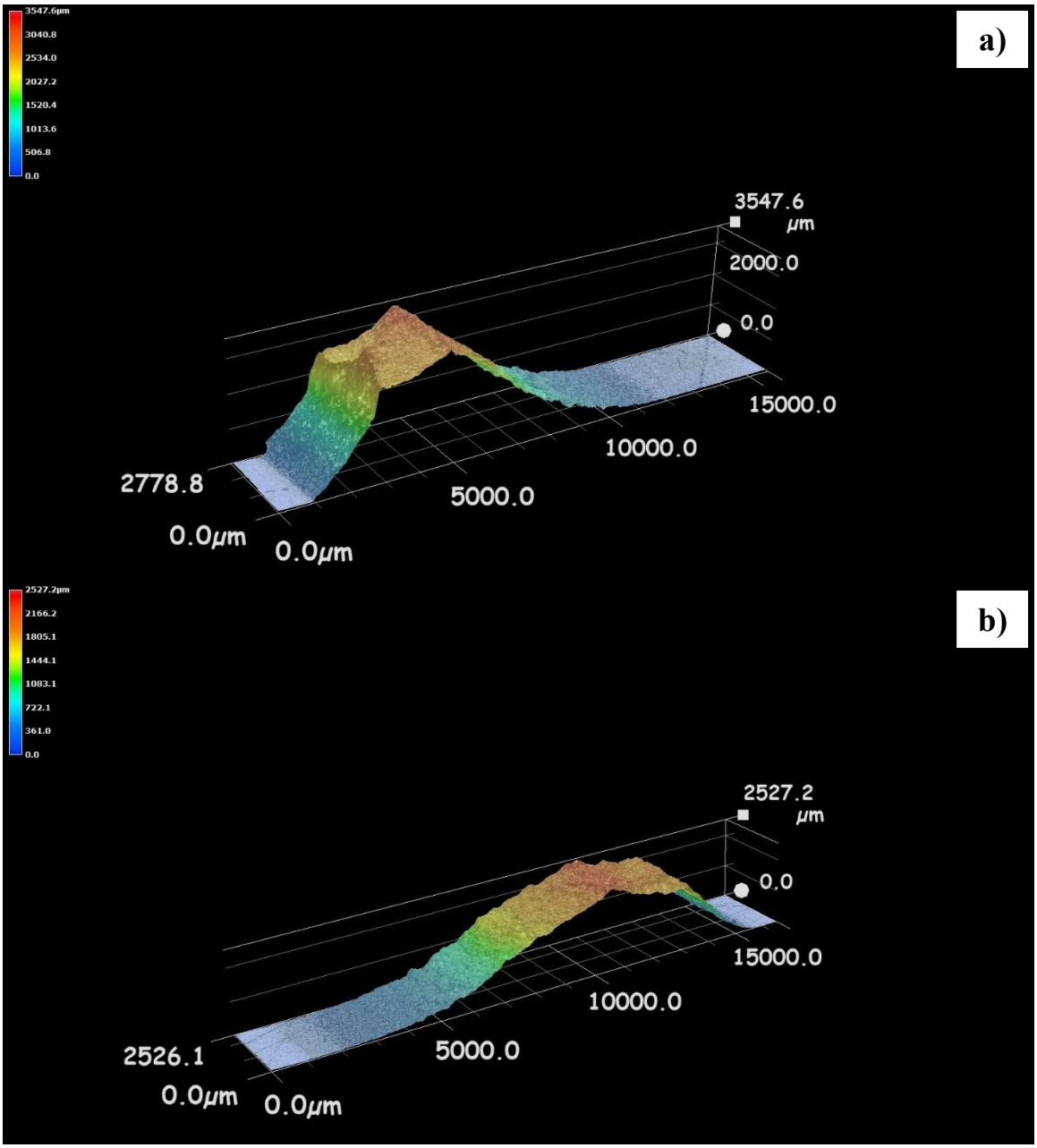

Figure 5.32 – 3D profile of coatings produced with the dual injection PBI nozzle when using only one injection (Table 5.5), a) Primary Powder Feeder (PPF) and b) Secondary Powder Feeder (SPF)

The next coating was produced using both injections with the parameters outlined in Table 5.6. These are the same as the parameters used for the single injection tests, from Table 5.5. However, both the PPF and SPF are used at the same time, and therefore each have a lower individual feed rate. The total feed rate during the spray is approximately the same as before (~7.9 g/min).

Table 5.6 – CGDS parameters for testing of the dual injection PBI prototype (15° inlets)

Pressure [MPa]	*Temperature [°C]*	*Stand-off distance [mm]*	*Traverse speed [mm/s]*	*Primary powder feeding [g/min]*	*Secondary powder feeding [g/min]*	*Number of passes*	*Injection gas flow rate [kg/s]*
1.21 (175 psi)	500	15	5	4.2	3.7	5	3.26×10^{-4} (30 SCFH)

Figure 5.33 shows the three-dimensional profile of the coating that resulted from the spray. The dual injection produced a peak that was more centered when compared to the single injection coatings. When compared to the 3D profile produced by the WC nozzle, shown in Figure 5.24a, the coating produced by the dual injection PBI nozzle is wider. Due to the increased width, the slope of the peak is also smoother and provides a flatter coating overall.

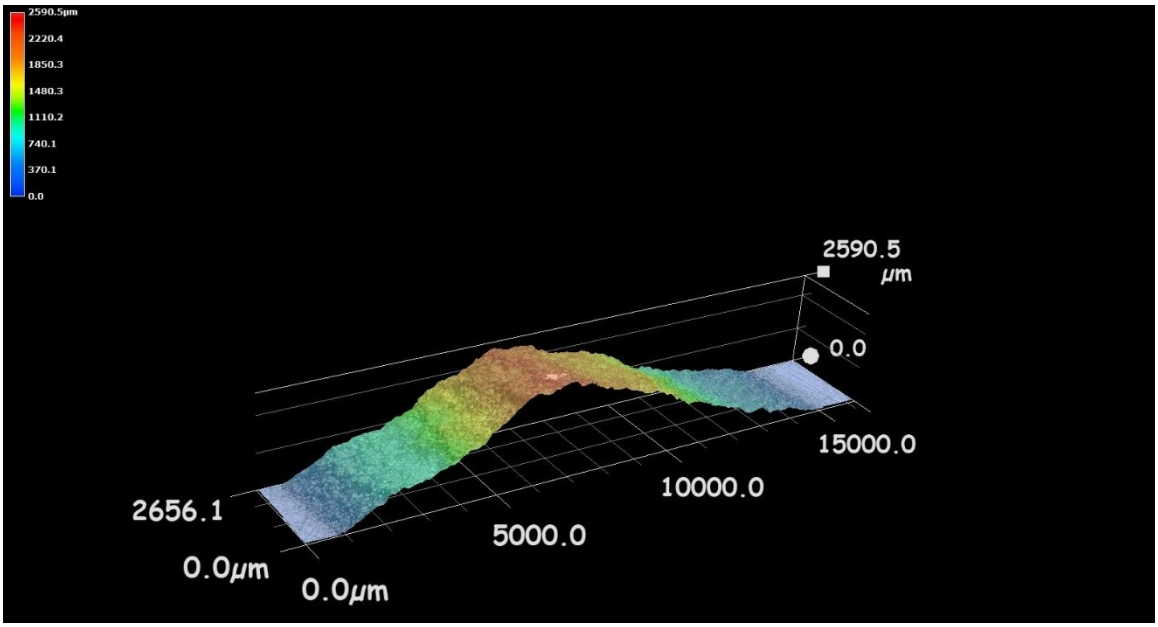

Figure 5.33 – 3D profile of coating produced with the dual injection PBI nozzle, using parameters from Table 5.6

More tests were performed to evaluate the performance of the dual injection nozzle over a single pass and for thinner coatings, which are more in line with Technoform's requirements. The initial test was therefore performed using their pressure parameters again, with the increased temperature of 500°C. The full parameters are shown in Table 5.7.

Table 5.7 – CGDS parameters to produce thin, single-pass coatings with the dual injection PBI prototype (15° inlets)

Pressure [MPa]	*Temperature [°C]*	*Stand-off distance [mm]*	*Traverse speed [mm/s]*	*Primary powder feeding [g/min]*	*Secondary powder feeding [g/min]*	*Number of passes*	*Injection gas flow rate [kg/s]*
1.21 (175 psi)	500	15	5	3.7	3.8	1	3.26×10^{-4} (30 SCFH)

The top view of the resulting coating is shown in Figure 5.34. The deposited aluminum coating was measured to be approximately 10.6 mm wide, while the total width of the substrate that was impacted by particles is approximately 13.6 mm in this case.

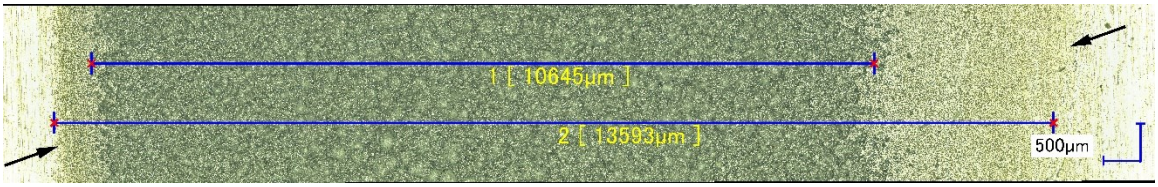

Figure 5.34 – Top view of the single-pass coating produce by the dual injection nozzle, using parameters from Table 5.7

Previous single-pass coatings produced as part of this work had a width of approximately 6.5 mm (Figure 5.4) and 7.5mm (Figure 5.23), and were produced by the WC prototype and the single injection PBI prototype, respectively. The dual injection nozzle produced a coating approximately 3 millimeters wider in this case. A direct comparison of these three figures is shown in Appendix A for convenience.

However, the dual injection coating produced is still skewed to one side. This is not in line with the thicker coating profile shown in Figure 5.33, which seemed to be more centered. This indicates that some particles which were depositing in the multi-pass spray are not depositing when passing over the substrate only once.

To alleviate this issue and try to improve the width of deposition, different parameters were tested. Technoform's parameters are based on deposition on their polyamide substrate, where low pressure is required to avoid eroding the plastic material. In this case, the pressure can be increased as the substrate is metal. Therefore, the pressure was increased to the maximum that the Centerline (Windsor) Ltd. system can handle in an effort to improve the coating. The optimized parameters used for aluminum on aluminum deposition are shown in Table 5.8.

Table 5.8 – Optimised CGDS parameters to produce thin, single-pass coatings with the dual injection PBI prototype (15° inlets)

Pressure [MPa]	*Temperature [°C]*	*Stand-off distance [mm]*	*Traverse speed [mm/s]*	*Primary powder feeding [g/min]*	*Secondary powder feeding [g/min]*	*Number of passes*	*Injection gas flow rate [kg/s]*
3.45 (500 psi)	500	15	5	3.7	3.8	1	3.26×10^{-4} (30 SCFH)

The improved parameters resulted in a significant increase in the coating width, up to a total width of approximately 14.1 mm, as shown in Figure 5.35. This is an increase of almost 4 mm compared to the previous dual injection coating (Figure 5.34), and an increase of nearly 8 mm compared to the original WC prototype (Figure 5.4).

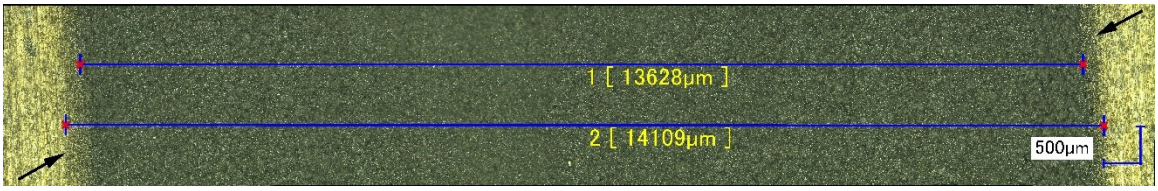

Figure 5.35 – Top view of coating produced with the dual injection PBI nozzle, using parameters from Table 5.8

Being a promising coating for Technoform's needs, this sample was cut, mounted, and polished according to the procedures outlined in Section 4.4 to obtain images of the cross-section. An image of the full cross-section is shown in Figure 5.36 along with a zoom on the right edge of the coating. Note that the black line between the coating and substrate is delamination that was caused by the grinding/polishing procedure. The coating did not delaminate in any way during the cutting stage of sample preparation.

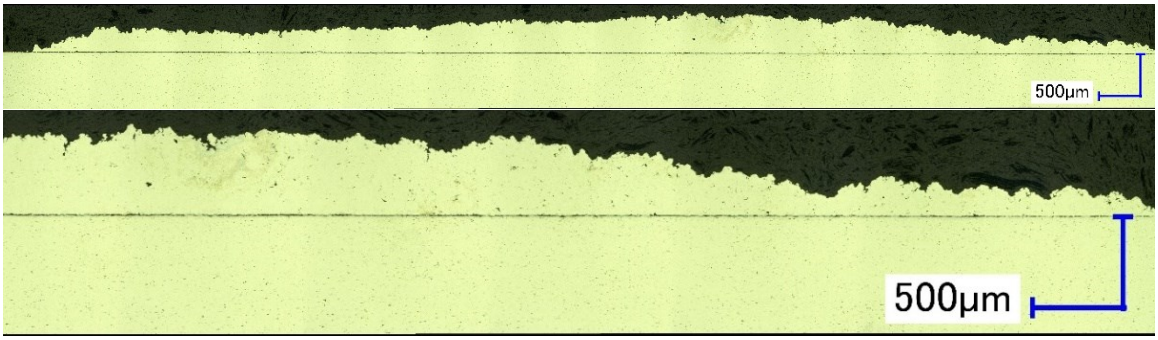

Figure 5.36 – Cross-sectional views of the aluminum coating produced with the dual injection PBI nozzle, using parameters from Table 5.8

The cross-section of the sample reveals that the coating is dense, however the thickness still varies across the width of the coating. Using ImageJ, multiple points of the coating were measured. The thickness varies from 504 µm at the thickest point, to 99 µm at one of the thinnest points seen on the right edge of the coating.

In an effort to obtain a more even coating, the gas flow rate of the powder inlets was experimented with. It was hypothesized that changing the injection gas flow rate would

affect the radial velocity of the particles as they enter the main gas flow, which would result in a different distribution at the nozzle outlet. This can be simulated before being tested experimentally, to evaluate if the gas flow rate does affect the particle position and distribution within the nozzle.

5.8 Optimization of Injection Gas Flow Rate

All sprays up to this point were performed using a fixed gas flow rate for the powder inlets, which carries the feedstock particles to the nozzle. The assumption is that the particles reach the main flow in the nozzle at approximately the same velocity as the carrier gas in the secondary lines. By increasing or decreasing the gas flow rate, assuming that the nitrogen behaves as an ideal gas and that its density remains relatively constant, the velocity of the gas should change according to the ideal gas law, as shown by Equation 5.1.

$$\dot{m} = \rho V A \qquad \text{(Eq. 5.1)}$$

The powder line has a constant cross-sectional area, so the velocity of the gas, and consequently the particles, should increase if the gas mass flow rate is increased. The change in particle velocity should affect their distribution at the nozzle exit. This would be caused by different particle-wall interactions due to the change in momentum of the particles as they enter the main flow.

To test this hypothesis, the dual injection simulation was modified to account for a higher mass flow rate at the particle inlet. The gas mass flow rate was changed from 3.26×10^{-4} kg/s (30 SCFH) to 6.52×10^{-4} kg/s (60 SCFH), as it is the maximum value that can be reached by the flowmeter in the lab. The resulting flow is similar, as shown in Figure 5.37, however the velocity is increased significantly from approximately 67 m/s to 85 m/s within the powder inlet.

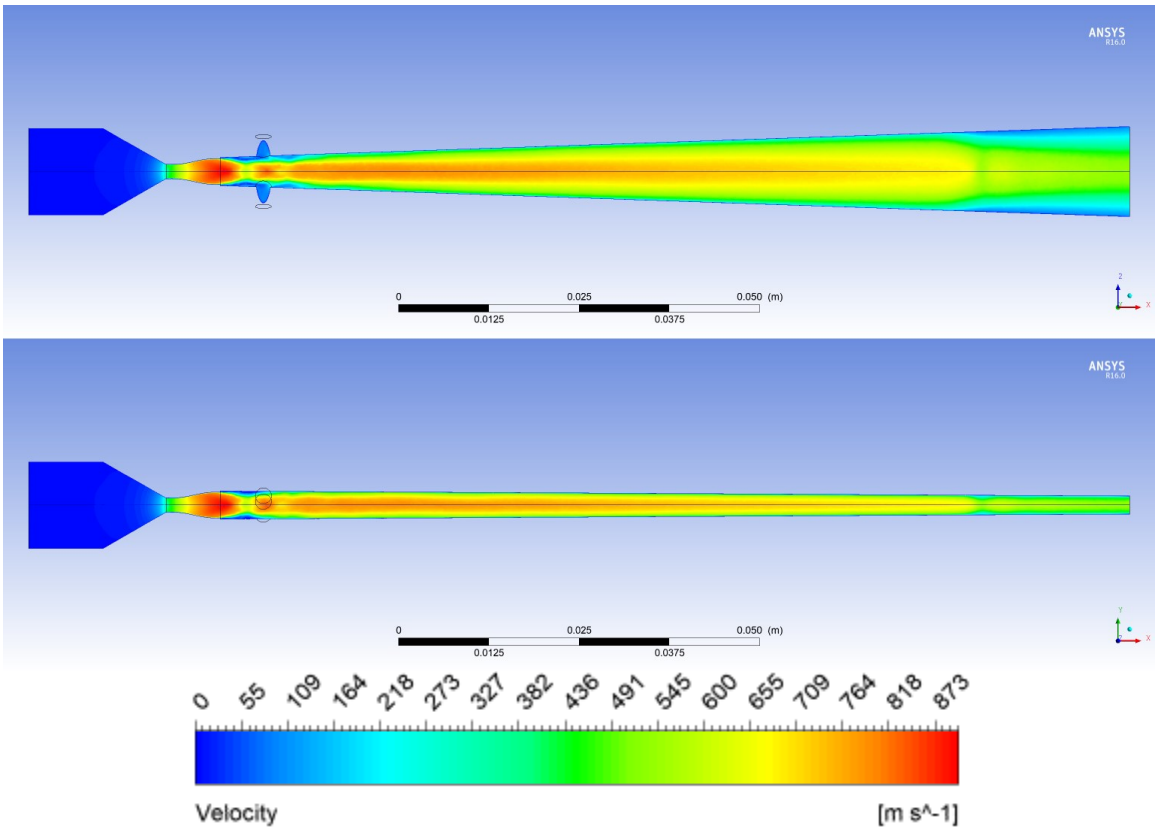

Figure 5.37 - Dual inlet velocity results for the 6.52x10^{-4} kg/s (60 SCFH) mass flow rate boundary condition at both powder inlets, top view (top) and side view (bottom)

Particles were injected as done in the previous simulations to evaluate the effect of the new gas mass flow rate on their position. Figure 5.38 shows a comparison of the distribution of 20 µm particles for the 3.26x10^{-4} kg/s (30 SCFH) and 6.52x10^{-4} kg/s (60 SCFH) powder inlet gas flow rates. The change in gas flow rate has shown to have a significant effect on the particle distribution at the nozzle outlet.

The lack of 20 µm particles in the center of the outlet that was present when using 3.26x10^{-4} kg/s (30 SCFH) is gone when doubling the flow rate to 6.52x10^{-4} kg/s (60 SCFH). The distribution of the 20 µm particles across the width of the nozzle is improved significantly. This is attributed to the increased radial velocity of the particles as they reach the main flow of the nozzle. With the added velocity caused by the increased gas flow rate, the 20 µm particles have enough momentum to cause additional impacts with the nozzle walls, helping to distribute them further. Visually, Figure 5.38 also shows that the velocity of the particles is more even, which should result in a more even coating deposition.

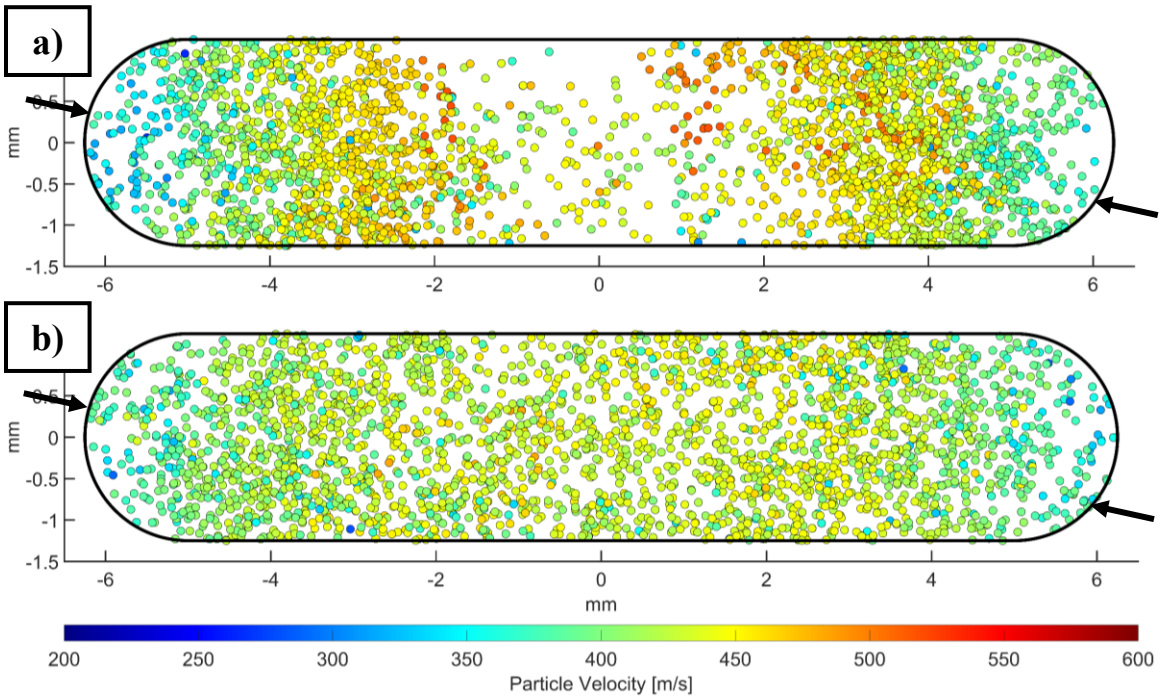

Figure 5.38 – Comparison of particle positions (20 µm diameter) at the nozzle exit plane when using a) 3.26x10^{-4} kg/s (30 SCFH) and b) 6.52x10^{-4} kg/s (60 SCFH) mass flow rates for each powder inlet. The upstream inlet positions are shown by black arrows

Figure 5.39 shows a comparison of the distribution of 50 µm particles for the 3.26x10^{-4} kg/s (30 SCFH) and 6.52x10^{-4} kg/s (60 SCFH) powder inlet gas flow rates. While the improvement in distribution is not as significant as it was for the 20 µm particles, it is still noticeable. The particle coverage is more even when using the increased 6.52x10^{-4} kg/s (60 SCFH) gas flow rate. The slight gap in particles seen at the rounded edges and the center of the outlet also look to have improved. Visually, Figure 5.39 also shows that the velocity of the 50 µm is more even across the nozzle width when using 6.52x10^{-4} kg/s (60 SCFH) as opposed to 3.26x10^{-4} kg/s (30 SCFH).

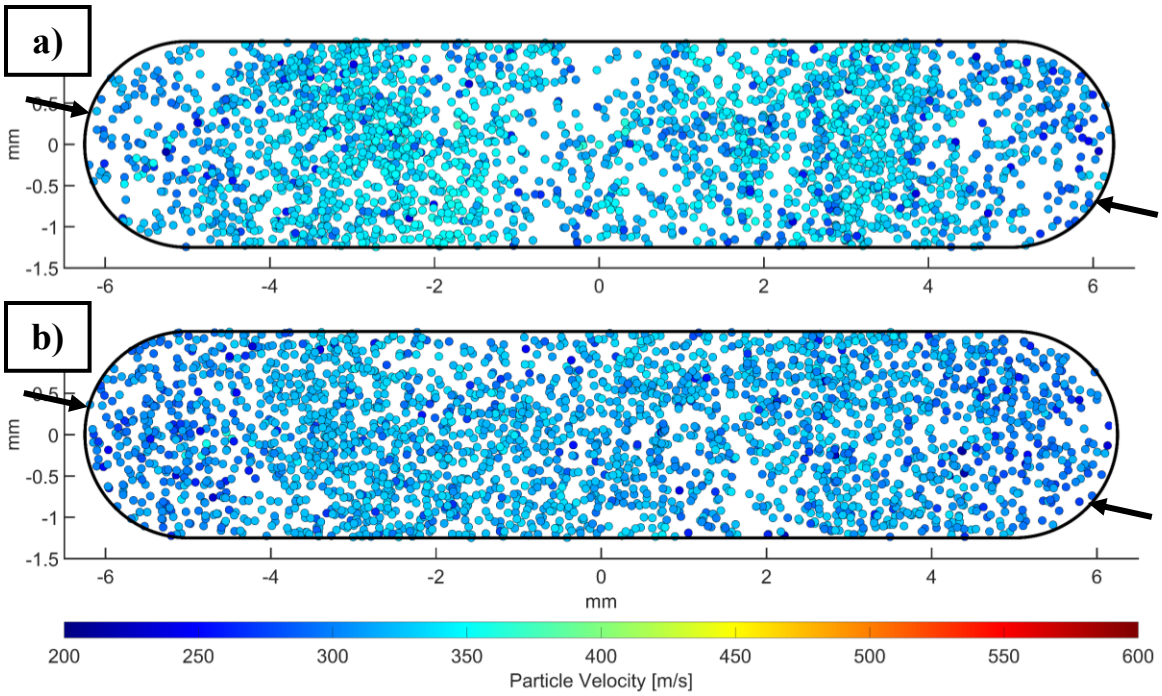

Figure 5.39 – Comparison of particle positions (50 µm diameter) at the nozzle exit plane when using a) 3.26×10^{-4} kg/s (30 SCFH) and b) 6.52×10^{-4} kg/s (60 SCFH) mass flow rates for each powder inlet. The upstream inlet positions are shown by black arrows

5.9 Experimental Comparison of Injection Gas Flow Rates

As it is evident from Figure 5.38 and Figure 5.39 that the change in mass flow rate has an effect on the position and distribution of the particles at the nozzle outlet, experimental tests were performed to test the impact of this effect on actual coatings. Additional gas flow rates were tested to evaluate their effects as well. These were done experimentally as opposed to computationally, as it is faster than re-simulating the entire gas flow for each new powder injection gas flow rates.

The chosen flow rates were 1.63×10^{-4}, 3.26×10^{-4}, 4.89×10^{-4}, and 6.52×10^{-4} kg/s. As previously mentioned, 3.26×10^{-4} kg/s (30 SCFH) had been used in the experimental tests prior to this section. The maximum gas flow rate that the flowmeter can provide in this case is 6.52×10^{-4} kg/s (60 SCFH), so 1.63×10^{-4} kg/s (15 SCFH) and 4.89×10^{-4} kg/s (45 SCFH) were selected as intermediary flow rates to have additional data points when

evaluating the effect on the deposited coating. Table 5.9 shows the parameters used for the sprays when testing the different gas flow rates.

Table 5.9 – Optimised CGDS parameters for the dual injection PBI prototype (15° inlets), with new gas flow rates for the powder injection inlets

Pressure [MPa]	*Temperature [°C]*	*Stand-off distance [mm]*	*Traverse speed [mm/s]*	*Primary powder feeding [g/min]*	*Secondary powder feeding [g/min]*	*Number of passes*	*Injection gas flow rates [kg/s]*
3.45 (500 psi)	500	15	5	3.7	3.8	1	1.63×10^{-4} 4.89×10^{-4} 6.52×10^{-4} (15/45/60 SCFH)

The results of these sprays are shown in Figure 5.40 and Figure 5.41, which show top and cross-sectional views of the coatings, respectively. Comparing the width of each coating, as measured from the top view in Figure 5.40, leads to the conclusion that varying the powder injection gas flow rate has little effect on the total deposition width. The width of the coating deposition varies from 13.63 to 13.77 mm, as demonstrated in Figure 5.40.

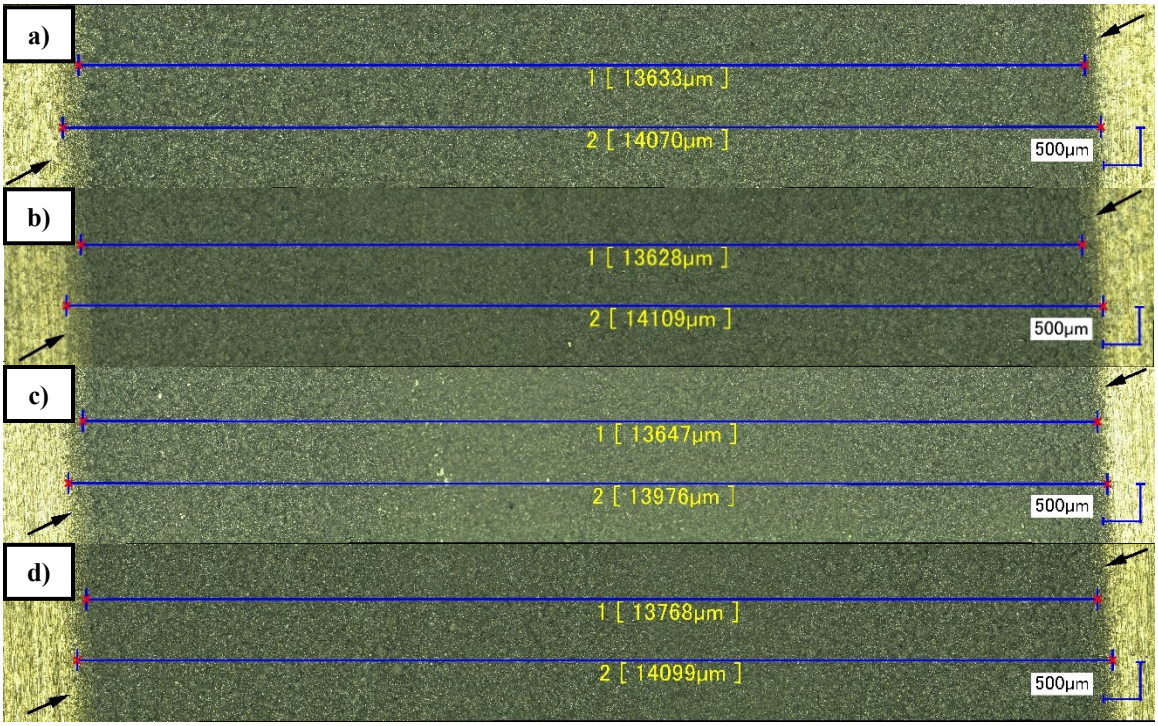

Figure 5.40 – Top view of sprays deposited using parameters from Table 5.8 and Table 5.9 for comparison of coating width; a) 1.63x10^{-4} kg/s (15 SCFH), b) 3.26x10^{-4} kg/s (30 SCFH), c) 4.89x10^{-4} kg/s (45 SCFH), and d) 6.52x10^{-4} kg/s (60 SCFH)

However, by looking at the cross-sectional profiles of each spray shown in Figure 5.41, it can be seen that changing the powder injection gas flow rate has an effect on the profile of the coating. The peak thickness and minimum thickness of each coating cross-sectional cut was measured. The 1.63x10^{-4} kg/s (15 SCFH) case has a peak thickness of 277 µm and lowest point of 69 µm. The 3.26x10^{-4} kg/s (30 SCFH), as seen previously, has a peak thickness of 504 µm and lowest point of 99 µm. The 4.89x10^{-4} kg/s (45 SCFH) case has a peak thickness of 465 µm and minimum thickness of 140 µm. And finally, the 6.52x10^{-4} kg/s (60 SCFH) case has a peak thickness of 282 µm and minimum thickness of 95 µm.

Therefore, the 6.52x10^{-4} kg/s (60 SCFH) case has the smallest variance between its peak and lowest point. It can also be seen visually, through the cross-sections, that this coating has a more even thickness across the entire width. It should be noted however that this coating is the thinnest of all four. Technoform only requires a thin layer of aluminum, at least a single particle in thickness, therefore this is still an adequate thickness for the purposes of this work.

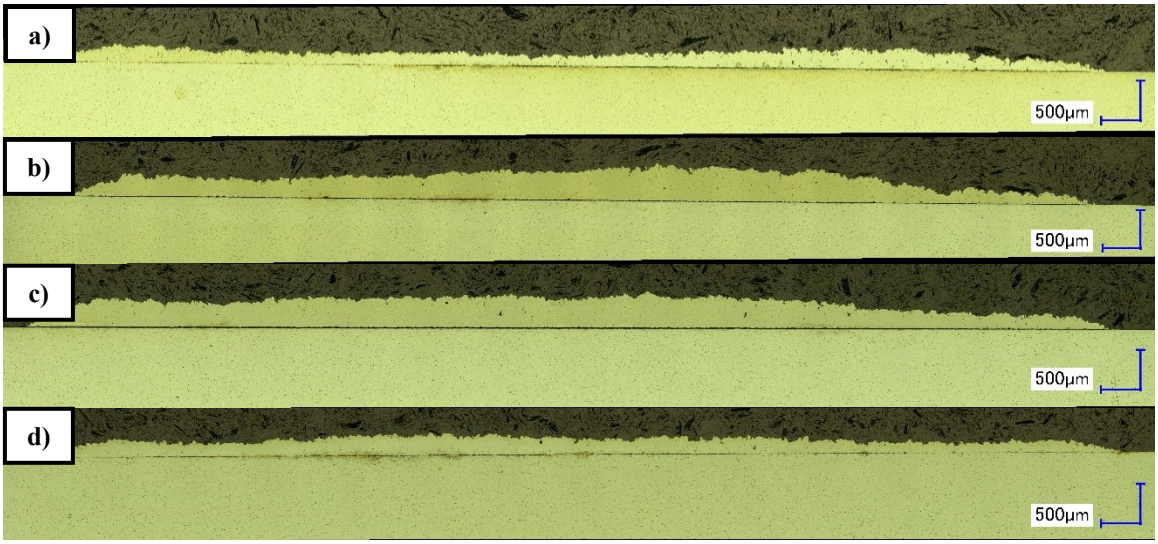

Figure 5.41 – Side view of sprays deposited using parameters from Table 5.8 and Table 5.9 for comparison of coating thickness; a) $1.63x10^{-4}$ kg/s (15 SCFH), b) $3.26x10^{-4}$ kg/s (30 SCFH), c) $4.89x10^{-4}$ kg/s (45 SCFH), and d) $6.52x10^{-4}$ kg/s (60 SCFH)

5.10 Experimental Results on Polyamide Substrate

Multiple coatings have been deposited onto aluminum 6061-T6 substrates with the PBI and WC obround nozzles using different parameters. Through iterative changes, the process was improved to obtain wider and flatter coatings for deposition on 6061-T6 substrates. To evaluate the performance of the dual injection PBI nozzle for its intended purpose, coatings need to be produced on the polyamide substrate used by Technoform.

The coatings sprayed on the polyamide substrate used revised parameters from Technoform, where they have increased the temperature to 350°C (previously 300°C), as they noted an increase in DE when using the higher temperature. The full revised parameters are shown in Table 5.10.

Table 5.10 – Revised Technoform CGDS parameters for polyamide substrates, used with the dual injection PBI prototype (15° inlets)

Pressure [MPa]	*Temperature [°C]*	*Stand-off distance [mm]*	*Traverse speed [mm/s]*	*Primary powder feeding [g/min]*	*Secondary powder feeding [g/min]*	*Number of passes*	*Injection gas flow rate [kg/s]*
1.21 (175 psi)	350	15	40	3.7	3.9	1	3.26×10^{-4} (30 SCFH)

The traverse speed was increased compared to the speed previously used for the aluminum substrates (5 mm/s) to avoid melting the thermoplastic material. The feed rates were kept as consistent as possible, at around 3.8 g/min per feeder. The initial spray was done at 3.26×10^{-4} kg/s (30 SCFH), despite the previous results showing that 6.52×10^{-4} kg/s (60 SCFH) provides improvements to the coating which are desirable for Technoform. This was done to obtain a baseline coating using the dual injection nozzle, before testing the increased gas mass flow rate for the powder injection.

Figure 5.42 shows the resulting deposition from the spray on polyamide using the revised Technoform parameters and the dual injection PBI nozzle, as seen through a 3D microscope.

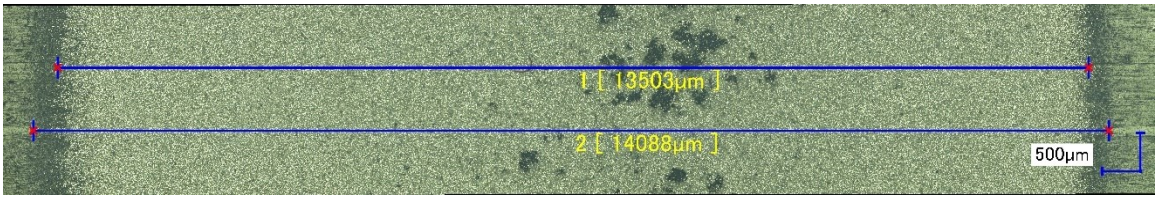

Figure 5.42 – Initial coating on polyamide substrate produced by the PBI dual injection nozzle, using parameters from Table 5.10

The coating produced using the parameters from Table 5.10 is approximately 13.5 mm wide, which is slightly wider than the nozzle outlet. This is a promising result for the coating width compared to what was observed for the WC nozzle on aluminum substrate. However, as clearly seen in Figure 5.42, there are several black spots in the middle of the coating. These are large enough to be clearly visible to the naked eye, as seen in Figure

5.43. These are areas where the aluminum particles either did not deposit on the polyamide substrate and instead eroded the surface, were adhered particles were removed by subsequent impacts. Either of these scenarios could lead to the discrepancy in coverage, which is not desirable.

Figure 5.43 shows a photograph of some aluminum coatings deposited on the polymer substrate. The rightmost coating is the spray result when using the parameters from Table 5.10. As previously discussed, there are black spots in the center of the coating which are clearly visible. Parameters were therefore modified for the next experiment with the aim of resolving the coverage issue in the middle of the coating, while maintaining its width. The coating in the center of the image is the result of this spray, keeping the same parameters other than the injection flow rate which is increased to 6.52×10^{-4} kg/s (60 SCFH). The coating on the left of the image keeps the increased injection flow rate of 6.52×10^{-4} kg/s (60 SCFH), but with a lower traverse speed (20 mm/s). The lower traverse speed caused the black spots to reappear in the coating. Particles most likely detached from the substrate due to subsequent particle impacts. These impacts were more frequent when producing this coating due to the lower traverse speed.

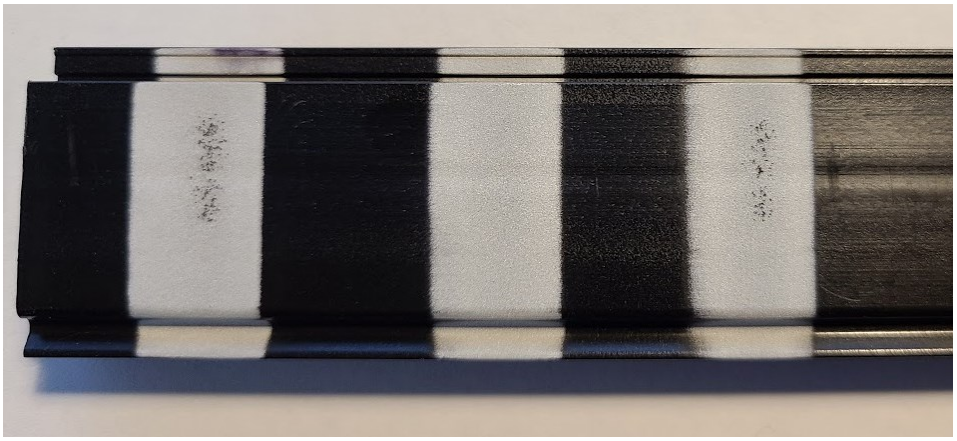

Figure 5.43 – Photograph of pure aluminum coatings on polyamide substrate, sprayed with the dual 15° injection PBI prototype

The full parameters used to produce the coating in the center of Figure 5.43 are shown in Table 5.11. As mentioned, these parameters are the same as the ones from Table 5.10 other than the increased gas flow rate in the powder inlets. The flow rate was increased to 6.52×10^{-4} kg/s (60 SCFH) to reflect the results shown in Section 5.8 and 5.9, which showed

that this flow rate provided a more even particle distribution at the nozzle outlet and a flatter coating thickness. Considering the thickness of the coating produced on the polyamide in Figure 5.42, which is on the order of a few particles at most, a more even deposition could solve the coverage issue. The coating results of the spray using the increased gas flow rate is shown in Figure 5.44.

Table 5.11 – Revised Technoform CGDS parameters for polyamide substrates, with optimised powder inlet mass flow rate used with the dual injection PBI prototype (15° inlets)

Pressure [MPa]	*Temperature [°C]*	*Stand-off distance [mm]*	*Traverse speed [mm/s]*	*Primary powder feeding [g/min]*	*Secondary powder feeding [g/min]*	*Number of passes*	*Injection gas flow rate [kg/s]*
1.21 (175 psi)	350	15	40	3.7	3.9	1	6.52×10^{-4} (60 SCFH)

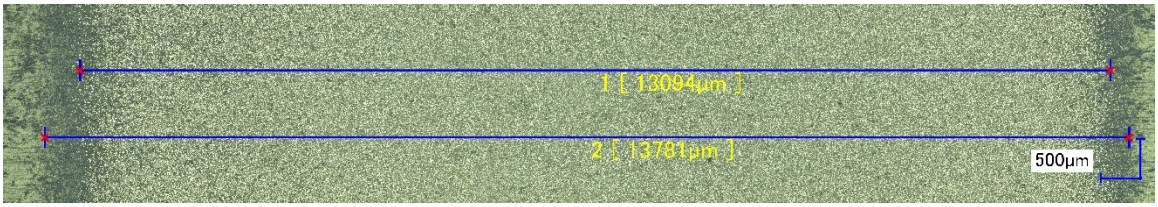

Figure 5.44 – Coating on polyamide substrate produced by the PBI dual injection nozzle, using parameters from Table 5.11

Once again, the deposited coating is slightly wider than the nozzle outlet, measuring approximately 13.1 mm. However, when comparing Figure 5.42 with Figure 5.44, it is clear that the discrepancy in coverage previously seen in the center of the coating is gone. The increase in gas flow rate when injecting the powder follows the trend previously seen when spraying on aluminum; it provides a more desirable coating profile for this application.

For comparison, the WC prototype was also tested on the polyamide substrate. The parameters from Table 5.12 were used for a direct comparison with the dual injection PBI nozzle, including the 6.52×10^{-4} kg/s (60 SCFH) gas flow rate. Considering there is only

one injection point in the WC nozzle, the rotational velocity of the feeding wheel was increased to match the total feed rate used with the dual injection nozzle (~7.6 g/min). With the increased velocity, the powder feed rate was measured to be 8.1 g/min which was deemed acceptable for this test as its purpose was to compare coating width, not thickness.

Table 5.12 – Revised Technoform CGDS parameters for polyamide substrates and optimised powder inlet mass flow rate for WC prototype (90° inlet)

Pressure [MPa]	*Temperature [°C]*	*Stand-off distance [mm]*	*Traverse speed [mm/s]*	*Powder feeding [g/min]*	*Number of passes*	*Injection gas flow rate [kg/s]*
1.21 (175 psi)	350	15	40	8.1	1	6.52×10^{-4} (60 SCFH)

The coating produced by the WC nozzle when using these parameters is shown in Figure 5.45. The coating has a width of approximately 8.6 mm, while impacts on the surface can be seen on a total width of 12.4 mm, nearly the full width of the nozzle. While these parameters provide a wider coating than what was initially deposited on an aluminum substrate (Figure 5.4), the coating produced here by the WC nozzle is approximately 4.5 mm narrower than the one produced by the PBI nozzle using the same parameters.

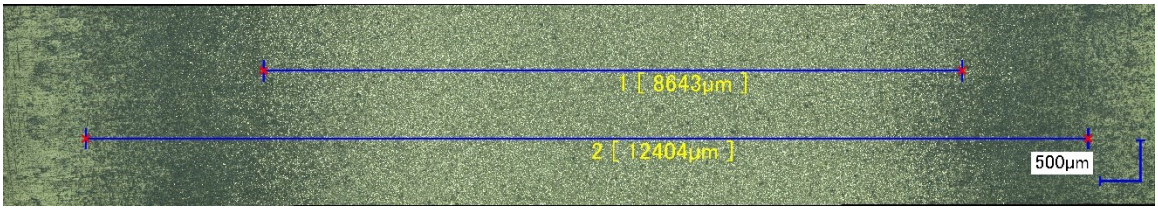

Figure 5.45 – Coating on polyamide produced by the WC nozzle (90° inlet), using the parameters from Table 5.12

Identical parameters were previously shown to favour the WC nozzle (Figure 5.24a vs. Figure 5.24b). However, increasing the process temperature drastically increased the deposition, which can only be done for extended periods of time with the PBI material. The temperature cannot be increased further in the case of the WC material due to nozzle clogging [66]. The PBI dual injection nozzle brings the possibility to further increase the process temperature to 500°C. It was shown previously, for the tests with the aluminum

6061-T6 substrates, that the PBI nozzle can be used at this temperature without clogging. The limiting factor in this case is the polyamide substrate, which could melt at elevated temperature. This could be potentially mitigated at the extreme traverse speeds achievable on Technoform's production line (2 m/s).

Figure 5.46 shows a photograph of two aluminum coatings on the polyamide substrate. Figure 5.46a shows the coating produced with the dual injection PBI prototype using the parameters from Table 5.11, which has a width of 13.1 mm. Figure 5.46b shows the coating produced with the WC prototype using parameters from Table 5.12, which has a width of 8.6 mm a the widest point. This figure shows a clear improvement of the coating when using the dual injection prototype, proving that the obround nozzle can satisfy Technoform's requirements.

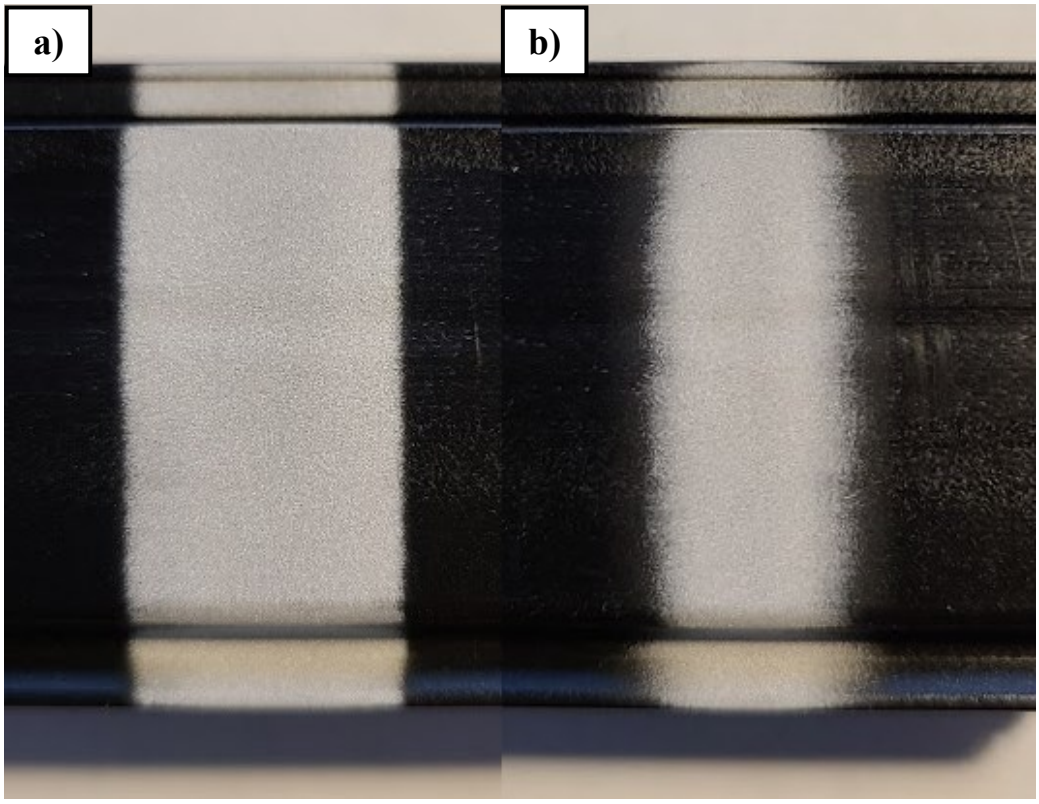

Figure 5.46 – Comparison of aluminum coatings on polyamide substrate produced by a) dual injection PBI nozzle (dual 15° inlets) and b) WC nozzle (90° inlet)

6 CONCLUSION

6.1 SUMMARY

This work explored the possibility of improving a non-axisymmetric obround nozzle for large scale use of cold gas dynamic spray. Issues with the initial design were analyzed through computational and experimental means. The two primary issues were found to be the particle distribution within the nozzle, and the material from which the prototype was manufactured.

Further computational work was performed to resolve the particle issue, in which the particles were essentially isolated to the center of the nozzle and not filling the full obround shape. Different radial powder injection points were tested; a side inlet (0° with regards to the reference plane), a 15° inlet, a 30° inlet, and 45° inlet. These were compared to the original gas powder inlet which was at the 90° position. Simulations showed that the 0° inlet and 15° inlet improved the lack of particles at the nozzle edges. The distribution within the nozzle was improved with these inlets through particle-wall interactions with all nozzle walls.

The material issue was resolved by replacing the tungsten carbide (WC) ceramic by polybenzimidazole (PBI), a high-performance thermoset polymer. Manufacturing challenges involving PBI were overcome by using a novel multi-piece design. The prototype was designed as two halves to allow for machining of the inner profile. An outer aluminum sleeve was also designed to complete the multi-piece nozzle, with the function of keeping both halves together firmly through a press fit.

Experimental tests of the PBI prototype on aluminum substrates resulted in a wider coating compared to similar tests performed with the WC prototype, up to 7.5 mm from 6.5 mm. This result is 5 mm short of the full nozzle width. The aluminum coating deposited by the PBI prototype was also offset from the nozzle center. These issues were attributed to a skewed particle size distribution within the nozzle.

Modifications to the PBI prototype were made to resolve the new issue. A second powder injection point was drilled across from the first to create a dual injection prototype. This

new approach was the result of further simulations, which showed a more even size distribution with an additional powder inlet. Additional aluminum coatings were sprayed using the modified PBI prototype, producing single-pass coatings up to 10.5 mm in width. After optimising spray parameters, a single-pass coating of up to 13.6 mm was obtained.

Next, the "flatness" of the coating was addressed, which refers to its thickness across its width. Different powder injection gas flow rates were tested through simulation to evaluate their effect on particle distribution at the nozzle outlet. Cases for 3.26×10^{-4} kg/s (30 SCFH) and 6.52×10^{-4} kg/s (60 SCFH) were compared, where significant differences in distribution were observed. Experimental tests were then performed to compare flowrates of 1.63×10^{-4} kg/s (15 SCFH), 4.89×10^{-4} kg/s (45 SCFH), and 6.52×10^{-4} kg/s (60 SCFH) to the flow rate of 3.26×10^{-4} kg/s (30 SCFH) that was previously used in all tests. The cross-section of these coatings revealed that the 6.52×10^{-4} kg/s (60 SCFH) gas flow rate produced a flatter coating across the entire width, with a variance of 187 µm between its highest and lowest points.

Finally, single-pass aluminum coatings were deposited on polyamide substrates provided by the main industrial partner, Technoform. These coatings were produced using the WC prototype and the dual injection PBI prototype for a one to one comparison. With the new and revised parameters from Technoform, the WC nozzle produced an 8.6 mm aluminum coating. The dual injection PBI prototype, using identical parameters, produced a 13 mm coating. This proved that the dual injection PBI nozzle is a viable solution for Technoform to produce wider coatings with a single nozzle, while using a nozzle material that is more resistant to clogging.

6.2 FUTURE WORK

While the feasibility of producing a wide and flat coating using an obround dual injection PBI nozzle has been proven in this work, many aspects of dual injection cold spray have yet to be studied. Experiments can be devised to further test and improve the dual injection as part of Technoform's application and more. Further studies could be undertaken, such as:

1. Study the feasibility of using a single powder feeder to deliver feedstock to both radial powder inlets on the nozzle.
2. Investigate the effect of powder loading on coating quality and properties when significantly increasing powder feed rate by using a dual injection nozzle
3. Perform deposition efficiency tests to determine if it is affected when going from a single injection to dual injections.

REFERENCES

[1] V. K. Champagne, "Introduction," in *The Cold Spray Materials Deposition Process: Fundamentals and Applications*, Elsevier Ltd., 2007, pp. 1–7.

[2] Y. Wu, W. Wu, W. Zhao, and X. Lan, "Revealing the antibacterial mechanism of copper surfaces with controllable microstructures," *Surf. Coatings Technol.*, vol. 395, p. 125911, May 2020, doi: 10.1016/j.surfcoat.2020.125911.

[3] V. Champagne, K. Sundberg, and D. Helfritch, "Kinetically deposited copper antimicrobial surfaces," *Coatings*, vol. 9, no. 4, pp. 1–9, 2019, doi: 10.3390/coatings9040223.

[4] J. Villafuerte, *Modern Cold Spray: Materials, Process, and Applications*. 2015.

[5] S. Natarajan, V. Sivan, P. G. Tennyson, and V. R. Kiran, "Protective coatings on magnesium and its alloys: A critical review," *Corros. Prev. Control*, vol. 51, no. 4, pp. 142–163, 2004, Accessed: Jun. 03, 2020. [Online]. Available: www.elsevier.com/locate/jallcom.

[6] R. C. McCune, "The use of cold spray coating for corrosion protection," in *The Cold Spray Materials Deposition Process: Fundamentals and Applications*, Elsevier Ltd., 2007, pp. 302–314.

[7] N. Dalili, A. Edrisy, and R. Carriveau, "A review of surface engineering issues critical to wind turbine performance," *Renew. Sustain. Energy Rev.*, vol. 13, no. 2, pp. 428–438, 2009, doi: 10.1016/j.rser.2007.11.009.

[8] A. Moridi, S. M. Hassani-Gangaraj, M. Guagliano, and M. Dao, "Cold spray coating: Review of material systems and future perspectives," *Surf. Eng.*, vol. 30, no. 6, pp. 369–395, 2014, doi: 10.1179/1743294414Y.0000000270.

[9] P. Richer, M. Yandouzi, M. Brochu, A. Zúñiga, A. Corbeil, and B. Jodoin, "Oxidation behaviour of conventional and nanocrystalline conicraly bond coats manufactured by cold spray," in *Proceedings of the ASME Turbo Expo*, 2011, vol. 4, pp. 737–745, doi: 10.1115/GT2011-45747.

[10] W. R. Chen, E. Irissou, X. Wu, J. G. Legoux, and B. R. Marple, “The oxidation behavior of TBC with cold spray CoNiCrAlY bond coat,” in *Journal of Thermal Spray Technology*, 2011, vol. 20, no. 1–2, pp. 132–138, doi: 10.1007/s11666-010-9601-1.

[11] L. Y. Kong *et al.*, “Preparation of TiAl 3-Al composite coating by cold spray and its high temperature oxidation behavior,” *J. Therm. Spray Technol.*, vol. 19, no. 6, pp. 1206–1210, 2010, doi: 10.1007/s11666-010-9516-x.

[12] M. J. Vucko, P. C. King, A. J. Poole, M. Z. Jahedi, and R. de Nys, “Polyurethane seismic streamer skins: an application of cold spray metal embedment,” *Biofouling*, vol. 29, no. 1, pp. 1–9, Jan. 2013, doi: 10.1080/08927014.2012.741682.

[13] M. J. Vucko, P. C. King, A. J. Poole, C. Carl, M. Z. Jahedi, and R. de Nys, “Cold spray metal embedment: an innovative antifouling technology,” *Biofouling*, vol. 28, no. 3, pp. 239–248, 2012, doi: 10.1080/08927014.2012.670849.

[14] V. K. Champagne, “The repair of magnesium rotorcraft components by cold spray,” *J. Fail. Anal. Prev.*, vol. 8, no. 2, pp. 164–175, 2008, doi: 10.1007/s11668-008-9116-y.

[15] R. Lupoi, “Current design and performance of cold spray nozzles: Experimental and numerical observations on deposition efficiency and particle velocity,” *Surf. Eng.*, vol. 30, no. 5, pp. 316–322, 2014, doi: 10.1179/1743294413Y.0000000214.

[16] A. Sova, I. Smurov, M. Doubenskaia, and P. Petrovskiy, “Deposition of aluminum powder by cold spray micronozzle,” *Int. J. Adv. Manuf. Technol.*, vol. 95, no. 9–12, pp. 3745–3752, 2018, doi: 10.1007/s00170-017-1443-2.

[17] B. Jodoin, “Cold spray nozzle mach number limitation,” *J. Therm. Spray Technol.*, vol. 11, no. 4, pp. 496–507, 2002, doi: 10.1361/105996302770348628.

[18] J. Pattison, S. Celotto, A. Khan, and W. O’Neill, “Standoff distance and bow shock phenomena in the Cold Spray process,” *Surf. Coatings Technol.*, vol. 202, no. 8, pp. 1443–1454, 2008, doi: 10.1016/j.surfcoat.2007.06.065.

[19] W. Y. Li *et al.*, “Effect of standoff distance on coating deposition characteristics in cold spraying,” *Mater. Des.*, vol. 29, no. 2, pp. 297–304, 2008, doi: 10.1016/j.matdes.2007.02.005.

[20] C. Feng *et al.*, “B4C/Ni Composite Coatings Prepared by Cold Spray of Blended or CVD-Coated Powders,” *J. Therm. Spray Technol.*, vol. 21, no. 3–4, pp. 561–570, Jun. 2012, doi: 10.1007/s11666-012-9774-x.

[21] J. Wu, J. Yang, H. Fang, S. Yoon, and C. Lee, “The bond strength of Al-Si coating on mild steel by kinetic spraying deposition,” *Appl. Surf. Sci.*, vol. 252, no. 22, pp. 7809–7814, Sep. 2006, doi: 10.1016/j.apsusc.2005.09.015.

[22] M. Bray, A. Cockburn, and W. O’Neill, “The Laser-assisted Cold Spray process and deposit characterisation,” *Surf. Coatings Technol.*, vol. 203, no. 19, pp. 2851–2857, 2009, doi: 10.1016/j.surfcoat.2009.02.135.

[23] A. Sova, S. Grigoriev, A. Okunkova, and I. Smurov, “Cold spray deposition of 316L stainless steel coatings on aluminium surface with following laser post-treatment,” *Surf. Coatings Technol.*, vol. 235, pp. 283–289, 2013, doi: 10.1016/j.surfcoat.2013.07.052.

[24] T. Marrocco, T. Hussain, D. G. McCartney, and P. H. Shipway, “Corrosion performance of laser posttreated cold sprayed titanium coatings,” *J. Therm. Spray Technol.*, vol. 20, no. 4, pp. 909–917, 2011, doi: 10.1007/s11666-011-9637-x.

[25] A. C. Hall, D. J. Cook, R. A. Neiser, T. J. Roemer, and D. A. Hirschfeld, “The effect of a simple annealing heat treatment on the mechanical properties of cold-sprayed aluminum,” *J. Therm. Spray Technol.*, vol. 15, no. 2, pp. 233–238, 2006, doi: 10.1361/105996306X108138.

[26] H. Y. Lee, S. H. Jung, S. Y. Lee, and K. H. Ko, “Alloying of cold-sprayed Al-Ni composite coatings by post-annealing,” *Appl. Surf. Sci.*, vol. 253, no. 7, pp. 3496–3502, 2007, doi: 10.1016/j.apsusc.2006.07.053.

[27] M. R. Rokni, C. A. Widener, S. P. Ahrenkiel, B. K. Jasthi, and V. R. Champagne, "Annealing behaviour of 6061 Aluminium deposited by high pressure cold spray," *Surf. Eng.*, vol. 30, no. 5, pp. 361–368, Jun. 2014, doi: 10.1179/1743294413Y.0000000209.

[28] R. Ghelichi, S. Bagherifard, D. Macdonald, I. Fernandez-Pariente, B. Jodoin, and M. Guagliano, "Experimental and numerical study of residual stress evolution in cold spray coating," *Appl. Surf. Sci.*, vol. 288, pp. 26–33, 2014, doi: 10.1016/j.apsusc.2013.09.074.

[29] K. Spencer, V. Luzin, N. Matthews, and M. X. Zhang, "Residual stresses in cold spray Al coatings: The effect of alloying and of process parameters," *Surf. Coatings Technol.*, vol. 206, no. 19–20, pp. 4249–4255, 2012, doi: 10.1016/j.surfcoat.2012.04.034.

[30] V. Luzin, K. Spencer, and M. X. Zhang, "Residual stress and thermo-mechanical properties of cold spray metal coatings," *Acta Mater.*, vol. 59, no. 3, pp. 1259–1270, 2011, doi: 10.1016/j.actamat.2010.10.058.

[31] C. W. Ziemian, M. M. Sharma, B. D. Bouffard, T. Nissley, and T. J. Eden, "Effect of substrate surface roughening and cold spray coating on the fatigue life of AA2024 specimens," *Mater. Des.*, vol. 54, pp. 212–221, 2014, doi: 10.1016/j.matdes.2013.08.061.

[32] M. M. Sharma, T. J. Eden, and B. T. Golesich, "Effect of Surface Preparation on the Microstructure, Adhesion, and Tensile Properties of Cold-Sprayed Aluminum Coatings on AA2024 Substrates," *J. Therm. Spray Technol.*, vol. 24, no. 3, pp. 410–422, 2014, doi: 10.1007/s11666-014-0175-1.

[33] P. Richer, B. Jodoin, L. Ajdelsztajn, and E. J. Lavernia, "Substrate roughness and thickness effects on cold spray nanocrystalline Al-Mg coatings," *J. Therm. Spray Technol.*, vol. 15, no. 2, pp. 246–254, 2006, doi: 10.1361/105996306X108174.

[34] A. Nastic, M. Vijay, A. Tieu, S. Rahmati, and B. Jodoin, “Experimental and Numerical Study of the Influence of Substrate Surface Preparation on Adhesion Mechanisms of Aluminum Cold Spray Coatings on 300M Steel Substrates,” *J. Therm. Spray Technol.*, vol. 26, no. 7, pp. 1461–1483, 2017, doi: 10.1007/s11666-017-0602-1.

[35] T. Samson, D. MacDonald, R. Fernández, and B. Jodoin, “Effect of Pulsed Waterjet Surface Preparation on the Adhesion Strength of Cold Gas Dynamic Sprayed Aluminum Coatings,” *J. Therm. Spray Technol.*, vol. 24, no. 6, pp. 984–993, 2015, doi: 10.1007/s11666-015-0261-z.

[36] H. Che, P. Vo, and S. Yue, “Investigation of Cold Spray on Polymers by Single Particle Impact Experiments,” *J. Therm. Spray Technol.*, vol. 28, no. 1–2, pp. 135–143, Nov. 2019, doi: 10.1007/s11666-018-0801-4.

[37] R. Gonzalez, H. Ashrafizadeh, A. Lopera, P. Mertiny, and A. McDonald, “A Review of Thermal Spray Metallization of Polymer-Based Structures,” *J. Therm. Spray Technol.*, vol. 25, no. 5, pp. 897–919, 2016, doi: 10.1007/s11666-016-0415-7.

[38] A. Ganesan, M. Yamada, and M. Fukumoto, “Cold spray coating deposition mechanism on the thermoplastic and thermosetting polymer substrates,” in *Journal of Thermal Spray Technology*, 2013, vol. 22, no. 8, pp. 1275–1282, doi: 10.1007/s11666-013-9984-x.

[39] R. Lupoi and W. O’Neill, “Deposition of metallic coatings on polymer surfaces using cold spray,” *Surf. Coatings Technol.*, vol. 205, no. 7, pp. 2167–2173, 2010, doi: 10.1016/j.surfcoat.2010.08.128.

[40] A. Alkhimov, V. Kosarev, and S. Klinkov, “The features of cold spray nozzle design,” *J. Therm. Spray Technol.*, vol. 10, pp. 375–381, 2001.

[41] S. Yin, X. fang Wang, and W. ya Li, “Computational analysis of the effect of nozzle cross-section shape on gas flow and particle acceleration in cold spraying,” *Surf. Coatings Technol.*, vol. 205, no. 8–9, pp. 2970–2977, 2011, doi: 10.1016/j.surfcoat.2010.11.002.

[42] V. Varadaraajan and P. Mohanty, “Design and optimization of rectangular cold spray nozzle: Radial injection angle, expansion ratio and traverse speed,” *Surf. Coatings Technol.*, vol. 316, pp. 246–254, Apr. 2017, doi: 10.1016/j.surfcoat.2017.03.005.

[43] L. Xue, S. Wang, and J. Jiang, “Cold Gas Dynamic Spray Apparatus, System and Method,” U.S. Patent 9,168,546 B2, Oct. 27, 2015.

[44] *Regulation No 1907/2006 of the European Parliament and of the Council*. European Parliament, 2006.

[45] X. Wang, B. Zhang, J. Lv, and S. Yin, “Investigation on the Clogging Behavior and Additional Wall Cooling for the Axial-Injection Cold Spray Nozzle,” *J. Therm. Spray Technol.*, vol. 24, no. 4, pp. 696–701, 2015, doi: 10.1007/s11666-015-0227-1.

[46] J. D. Haynes and S. A. Sanders, “Cold spray nozzle design,” U.S. Patent US 20040191449 A1, 2004.

[47] P. Liebersbach, A. Foelsche, V. K. Champagne, M. Siopis, A. Nardi, and D. P. Schmidt, “CFD Simulations of Feeder Tube Pressure Oscillations and Prediction of Clogging in Cold Spray Nozzles,” *J. Therm. Spray Technol.*, vol. 29, no. 3, pp. 400–412, Feb. 2020, doi: 10.1007/s11666-020-00992-0.

[48] A. Sova, A. Okunkova, S. Grigoriev, and I. Smurov, “Velocity of the particles accelerated by a cold spray micronozzle: Experimental measurements and numerical simulation,” *J. Therm. Spray Technol.*, vol. 22, no. 1, pp. 75–80, 2013, doi: 10.1007/s11666-012-9846-y.

[49] O. C. Ozdemir and C. A. Widener, “Influence of Powder Injection Parameters in High-Pressure Cold Spray,” *J. Therm. Spray Technol.*, vol. 26, no. 7, pp. 1411–1422, 2017, doi: 10.1007/s11666-017-0606-x.

[50] S. Yin, Q. Liu, H. Liao, and X. Wang, “Effect of injection pressure on particle acceleration, dispersion and deposition in cold spray,” *Comput. Mater. Sci.*, vol. 90, pp. 7–15, Jul. 2014, doi: 10.1016/j.commatsci.2014.03.055.

[51] M. Siopsis and et al., “Study of Nozzle Clogging During Cold Spray,” 2017.

[52] S. H. Thurston, “Method of Impacting One Metal Upon Another,” U.S. Patent 706,701, 1902.

[53] E. Irissou, J. G. Legoux, A. N. Ryabinin, B. Jodoin, and C. Moreau, “Review on cold spray process and technology: Part I - Intellectual property,” *J. Therm. Spray Technol.*, vol. 17, no. 4, pp. 495–516, Dec. 2008, doi: 10.1007/s11666-008-9203-3.

[54] H. Singh, T. S. Sidhu, and S. B. S. Kalsi, “Cold spray technology: Future of coating deposition processes,” *Frat. ed Integrita Strutt.*, vol. 22, no. 22, pp. 69–84, Sep. 2012, doi: 10.3221/IGF-ESIS.22.08.

[55] C. F. Rocheville, “Device for Treating the Surface of a Workpiece,” U.S. Patent 3,100,724, 1963.

[56] A. Alkhimov, N. I. Nesterovich, A. Papyrin, V. Kosarev, and M. M. Shushpanov, “Device for Applying Coatings,” SU1618777, 1986.

[57] A. Alkhimov, V. Kosarev, N. I. Nesterovich, and A. Papyrin, “Method for Deposition of Coatings,” SU1618778, 1986.

[58] A. Alkhimov, A. Papyrin, and V. Kosarev, “Gas-Dynamic Spraying Method for Applying a Coating,” U.S. Patent 5,302,414, 1994.

[59] T. Schmidt, F. Gärtner, H. Assadi, and H. Kreye, “Development of a generalized parameter window for cold spray deposition,” *Acta Mater.*, vol. 54, no. 3, pp. 729–742, 2006, doi: 10.1016/j.actamat.2005.10.005.

[60] T. Stoltenhoff, H. Kreye, and H. J. Richter, “An Analysis of the Cold Spray Process and Its Coatings,” *J. Therm. Spray Technol.*, vol. 11, no. 4, pp. 542–550, 2002, doi: 10.1361/105996302770348682.

[61] P. J. Pritchard and J. W. Mitchell, *Fox and McDonald’s Introduction to Fluid Mechanics*, vol. 1. 2015.

[62] R. C. Dykhuizen and M. F. Smith, “Gas Dynamic Principles of Cold Spray,” *J. Therm. Spray Technol.*, vol. 7, no. 2, pp. 205–212, 1998, doi: 10.1361/105996398770350945.

[63] J. G. Legoux, E. Irissou, and C. Moreau, “Effect of Substrate Temperature on the Formation Mechanism of Cold-Sprayed Aluminum, Zinc and Tin Coatings,” doi: 10.1007/s11666-007-9091-y.

[64] A. G. McDonald, A. N. Ryabinin, E. Irissou, and J. G. Legoux, “Gas-substrate heat exchange during cold-gas dynamic spraying,” in *Journal of Thermal Spray Technology*, 2013, vol. 22, no. 2–3, pp. 391–397, doi: 10.1007/s11666-012-9828-0.

[65] F. Gärtner, T. Stoltenhoff, T. Schmidt, and H. Kreye, “The Cold Spray Process and Its Potential for Industrial Applications,” *J. Therm. Spray Technol.*, vol. 15, pp. 223–232, 2006, doi: 10.1361/105996306X108110.

[66] D. Macdonald, S. Leblanc-Robert, R. Fernández, A. Farjam, and B. Jodoin, “Effect of Nozzle Material on Downstream Lateral Injection Cold Spray Performance,” *J. Therm. Spray Technol.*, vol. 25, pp. 1149–1157, 2016, doi: 10.1007/s11666-016-0426-4.

[67] O. C. Ozdemir, C. A. Widener, D. Helfritch, and F. Delfanian, “Estimating the Effect of Helium and Nitrogen Mixing on Deposition Efficiency in Cold Spray,” *J. Therm. Spray Technol.*, vol. 25, doi: 10.1007/s11666-016-0394-8.

[68] D. Macdonald, S. Rahmati, B. Jodoin, and W. Birtch, “An Economical Approach to Cold Spray Using In-line Nitrogen-Helium Blending,” *J. Therm. Spray Technol.*, vol. 28, pp. 161–173, 2019, doi: 10.1007/s11666-018-0813-0.

[69] X. T. Luo, Y. J. Li, and C. J. Li, “A comparison of cold spray deposition behavior between gas atomized and dendritic porous electrolytic Ni powders under the same spray conditions,” *Mater. Lett.*, vol. 163, pp. 58–60, Jan. 2016, doi: 10.1016/j.matlet.2015.10.048.

[70] M. R. Rokni, C. A. Widener, and G. A. Crawford, “Microstructural evolution of 7075 Al gas atomized powder and high-pressure cold sprayed deposition,” *Surf. Coatings Technol.*, vol. 251, pp. 254–263, Jul. 2014, doi: 10.1016/j.surfcoat.2014.04.035.

[71] X.-J. Ning, J.-H. Jang, and H.-J. Kim, “The effects of powder properties on in-flight particle velocity and deposition process during low pressure cold spray process,” *Appl. Surf. Sci.*, vol. 253, no. 18, pp. 7449–7455, Jul. 2007, doi: 10.1016/J.APSUSC.2007.03.031.

[72] J. Song, J. Liu, Q. Chen, and K. Li, “Effect of the Shape Factor on the Cold-Spraying Dynamic Characteristics of Sprayed Particles,” *J. Therm. Spray Technol.*, vol. 26, no. 8, pp. 1851–1858, 2017, doi: 10.1007/s11666-017-0616-8.

[73] O. Stier, “Fundamental cost analysis of cold spray,” *J. Therm. Spray Technol.*, vol. 23, no. 1–2, pp. 131–139, 2014, doi: 10.1007/s11666-013-9972-1.

[74] M. Fukumoto *et al.*, “Effect of substrate temperature on deposition behavior of copper particles on substrate surfaces in the cold spray process,” in *Journal of Thermal Spray Technology*, 2007, vol. 16, no. 5–6, pp. 643–650, doi: 10.1007/s11666-007-9121-9.

[75] K. Taylor, B. Jodoin, and J. Karov, “Particle loading effect in cold spray,” *J. Therm. Spray Technol.*, vol. 15, no. 2, pp. 273–279, 2006, doi: 10.1361/105996306X108237.

[76] D. MacDonald, A. Nastic, and B. Jodoin, “Understanding Adhesion,” in *Cold-Spray Coatings*, Springer International Publishing, 2018, pp. 421–450.

[77] T. Hussain, D. G. McCartney, P. H. Shipway, and D. Zhang, “Bonding mechanisms in cold spraying: The contributions of metallurgical and mechanical components,” *J. Therm. Spray Technol.*, vol. 18, no. 3, pp. 364–379, 2009, doi: 10.1007/s11666-009-9298-1.

[78] T. Schmidt *et al.*, “From particle acceleration to impact and bonding in cold spraying,” *J. Therm. Spray Technol.*, vol. 18, no. 5–6, pp. 794–808, 2009, doi: 10.1007/s11666-009-9357-7.

[79] M. Grujicic, C. L. Zhao, W. S. DeRosset, and D. Helfritch, “Adiabatic shear instability based mechanism for particles/substrate bonding in the cold-gas dynamic-spray process,” *Mater. Des.*, vol. 25, no. 8, pp. 681–688, Dec. 2004, doi: 10.1016/j.matdes.2004.03.008.

[80] H. Assadi, F. Gärtner, T. Stoltenhoff, and H. Kreye, “Bonding mechanism in cold gas spraying,” *Acta Mater.*, vol. 51, no. 15, pp. 4379–4394, Sep. 2003, doi: 10.1016/S1359-6454(03)00274-X.

[81] R. W. Armstrong and S. M. Walley, “High strain rate properties of metals and alloys,” *Int. Mater. Rev.*, vol. 53, no. 3, pp. 105–128, 2008, doi: 10.1179/174328008X277795.

[82] P. C. King, S. H. Zahiri, and M. Jahedi, “Microstructural refinement within a cold-sprayed copper particle,” *Metall. Mater. Trans. A Phys. Metall. Mater. Sci.*, vol. 40, no. 9, pp. 2115–2123, Jun. 2009, doi: 10.1007/s11661-009-9882-5.

[83] R. Nikbakht, S. H. Seyedein, S. Kheirandish, H. Assadi, and B. Jodoin, “Asymmetrical bonding in cold spraying of dissimilar materials,” *Appl. Surf. Sci.*, vol. 444, pp. 621–632, Jun. 2018, doi: 10.1016/j.apsusc.2018.03.103.

[84] W. Y. Li, C. Zhang, X. Guo, C. J. Li, H. Liao, and C. Coddet, “Study on impact fusion at particle interfaces and its effect on coating microstructure in cold spraying,” *Appl. Surf. Sci.*, vol. 254, no. 2, pp. 517–526, Nov. 2007, doi: 10.1016/j.apsusc.2007.06.026.

[85] S. Yin, Y. Xie, X. Suo, H. Liao, and X. Wang, “Interfacial bonding features of Ni coating on Al substrate with different surface pretreatments in cold spray,” *Mater. Lett.*, vol. 138, pp. 143–147, Jan. 2015, doi: 10.1016/j.matlet.2014.10.016.

[86] V. K. Champagne, D. J. Helfritch, S. P. G. Dinavahi, and P. F. Leyman, “Theoretical and experimental particle velocity in cold spray,” *Journal of Thermal Spray Technology*, vol. 20, no. 3. Springer, pp. 425–431, Mar. 06, 2011, doi: 10.1007/s11666-010-9530-z.

[87] D. L. Gilmore, R. C. Dykhuizen, R. A. Neiser, T. J. Roemer, and M. F. Smith, “Particle Velocity and Deposition Efficiency in the Cold Spray Process,” *J. Therm. Spray Technol.*, vol. 8, pp. 576–582, 1999.

[88] T. Schmidt, F. Gaertner, and H. Kreye, “New developments in cold spray based on higher gas and particle temperatures,” in *Proceedings of the International Thermal Spray Conference*, 2006, pp. 488–494, doi: 10.1361/105996306X147144.

[89] P. Alkimov, V. Kosarev, and A. Papyrin, “A Method of Cold Gas-Dynamic Deposition,” *Sov. Physics-Doklady*, vol. 35, no. 12, pp. 1047–1049, 1990.

[90] R. C. McCune, A. Papyrin, J. N. Hall, W. L. Riggs II, and P. H. Zajchowski, “An Exploration of the Cold Gas-Dynamic Spray Method for Several Materials Systems,” 1995.

[91] Y. Watanabe, C. Yoshida, K. Atsumi, M. Yamada, and M. Fukumoto, “Influence of Substrate Temperature on Adhesion Strength of Cold-Sprayed Coatings,” *J. Therm. Spray Technol.*, vol. 24, no. 1–2, pp. 86–91, 2014, doi: 10.1007/s11666-014-0165-3.

[92] A. P. Alkhimov, V. F. Kosarev, and A. N. Papyrin, “Gas-dynamic spraying. An experimental study of the spraying process,” *J. Appl. Mech. Tech. Phys.*, vol. 39, no. 2, pp. 318–323, 1998, doi: 10.1007/bf02468100.

[93] S. Kalpakjan and S. R. Schmid, *Manufacturing Engineering and Technology*, 6th ed. Prentice Hall, 2009.

[94] M. Groppe, “Cemented Carbides,” in *CIRP Encyclopedia of Production Engineering*, L. Laperrière and G. Reinhart, Eds. Berlin, Heidelberg: Springer Berlin Heidelberg, 2014, pp. 127–135.

[95] J. Sheikh-Ahmad and J. Davim, “Tool wear in machining processes for composites,” 2012.

[96] Hyperion Materials and Technologies, “Cemented carbide,” 2020. https://www.hyperionmt.com/en/technologies/cemented-carbide/ (accessed Mar. 16, 2020).

[97] R. M. German, “Sintering,” in *Encyclopedia of Materials: Science and Technology*, K. H. J. Buschow, R. W. Cahn, M. C. Flemings, B. Ilschner, E. J. Kramer, S. Mahajan, and P. Veyssière, Eds. Oxford: Elsevier, 2001, pp. 8641–8643.

[98] H. El-Hofy, *Fundamentals of Machining Processes: Conventional and Nonconventional Processes*, 2nd ed. Taylor & Francis, 2014.

[99] J. R. Walker and B. Dixon, *Machining Fundamentals*, 10th ed. Goodheart-Wilcox, 2018.

[100] M. Gardon, A. Latorre, M. Torrell, S. Dosta, J. Fernández, and J. M. Guilemany, “Cold gas spray titanium coatings onto a biocompatible polymer,” *Mater. Lett.*, vol. 106, pp. 97–99, Sep. 2013, doi: 10.1016/j.matlet.2013.04.115.

[101] P. C. King, A. J. Poole, S. Horne, R. de Nys, S. Gulizia, and M. Z. Jahedi, “Embedment of copper particles into polymers by cold spray,” *Surf. Coatings Technol.*, vol. 216, pp. 60–67, Feb. 2013, doi: 10.1016/j.surfcoat.2012.11.023.

[102] D. Giraud, F. Borit, V. Guipont, M. Jeandin, and J. M. Malhaire, “Metallization of a polymer using cold spray: Application to aluminum coating of polyamide 66,” *Proc. Int. Therm. Spray Conf.*, no. May 2012, pp. 265–270, 2012.

[103] X. L. Zhou, A. F. Chen, J. C. Liu, X. K. Wu, and J. S. Zhang, “Preparation of metallic coatings on polymer matrix composites by cold spray,” *Surf. Coatings Technol.*, vol. 206, no. 1, pp. 132–136, Oct. 2011, doi: 10.1016/j.surfcoat.2011.07.005.

[104] M. R. Rokni, C. A. Widener, O. C. Ozdemir, and G. A. Crawford, “Microstructure and mechanical properties of cold sprayed 6061 Al in As-sprayed and heat treated condition,” *Surf. Coatings Technol.*, vol. 309, pp. 641–650, Jan. 2017, doi: 10.1016/j.surfcoat.2016.12.035.

[105] J. C. Lee, H. J. Kang, W. S. Chu, and S. H. Ahn, “Repair of Damaged Mold Surface by Cold-Spray Method,” *CIRP Ann. - Manuf. Technol.*, vol. 56, no. 1, pp. 577–580, Jan. 2007, doi: 10.1016/j.cirp.2007.05.138.

[106] P. Cavaliere and A. Silvello, “Crack Repair in Aerospace Aluminum Alloy Panels by Cold Spray,” *J. Therm. Spray Technol.*, vol. 26, no. 4, pp. 661–670, 2017, doi: 10.1007/s11666-017-0534-9.

[107] S. Rech, A. Trentin, S. Vezzù, J. G. Legoux, E. Irissou, and M. Guagliano, “Influence of pre-heated Al 6061 substrate temperature on the residual stresses of multipass Al coatings deposited by cold spray,” in *Journal of Thermal Spray Technology*, 2011, vol. 20, no. 1–2, pp. 243–251, doi: 10.1007/s11666-010-9596-7.

[108] L. Ajdelsztajn, B. Jodoin, G. E. Kim, and J. M. Schoenung, “Cold spray deposition of nanocrystalline aluminum alloys,” *Metall. Mater. Trans. A Phys. Metall. Mater. Sci.*, vol. 36, no. 3, pp. 657–666, 2005, doi: 10.1007/s11661-005-0182-4.

[109] A. C. Hall, L. N. Brewer, and T. J. Roemer, “Preparation of aluminum coatings containing homogenous nanocrystalline microstructures using the cold spray process,” *J. Therm. Spray Technol.*, vol. 17, no. 3, pp. 352–359, 2008, doi: 10.1007/s11666-008-9180-6.

[110] A. Nastic and B. Jodoin, “Evaluation of Heat Transfer Transport Coefficient for Cold Spray Through Computational Fluid Dynamics and Particle In-Flight Temperature Measurement Using a High-Speed IR Camera,” *J. Therm. Spray Technol.*, vol. 27, no. 8, pp. 1491–1517, Dec. 2018, doi: 10.1007/s11666-018-0787-y.

[111] A. Sova, M. Doubenskaia, S. Grigoriev, A. Okunkova, and I. Smurov, “Parameters of the gas-powder supersonic jet in cold spraying using a mask,” *J. Therm. Spray Technol.*, vol. 22, no. 4, pp. 551–556, Apr. 2013, doi: 10.1007/s11666-013-9891-1.

[112] S. Yin, M. Meyer, W. Li, H. Liao, and R. Lupoi, “Gas Flow, Particle Acceleration, and Heat Transfer in Cold Spray: A review,” *Journal of Thermal Spray Technology*, vol. 25, no. 5. Springer New York LLC, pp. 874–896, Jun. 01, 2016, doi: 10.1007/s11666-016-0406-8.

[113] “ANSYS FLUENT 12.0 Theory Guide,” *ANSYS, Inc.*, 2009. https://www.afs.enea.it/project/neptunius/docs/fluent/html/th/main_pre.htm (accessed Dec. 08, 2020).

[114] S. A. Morsi and A. J. Alexander, “An investigation of particle trajectories in two-phase flow systems,” *J. Fluid Mech.*, vol. 55, no. 2, pp. 193–208, Sep. 1972, doi: 10.1017/S0022112072001806.

[115] R. Clift, M. E. Weber, and J. R. Grace, *Bubbles, Drops, and Particles*. 1978.

[116] F. Ghirelli, “Accurate RANS modeling of turbulent dispersion from arbitrary sources,” *Comput. Fluids*, vol. 100, pp. 59–64, Sep. 2014, doi: 10.1016/j.compfluid.2014.04.029.

[117] “ANSYS FLUENT 12.0/12.1 Documentation,” *ANSYS, Inc.*, 2009. https://www.afs.enea.it/project/neptunius/docs/fluent/ (accessed Jul. 29, 2020).

[118] J. H. Ferziger and M. Peric, *Computational Methods for Fluid Dynamics*, 3rd ed., vol. 53, no. 9. Springer, 2002.

[119] A. Syrakos, S. Varchanis, Y. Dimakopoulos, A. Goulas, and J. Tsamopoulos, “A critical analysis of some popular methods for the discretisation of the gradient operator in finite volume methods,” *Phys. Fluids*, vol. 29, no. 12, p. 127103, Dec. 2017, doi: 10.1063/1.4997682.

[120] J. Hrvoje, “Finite Volume Discretisation in OpenFOAM.” Chalmers University, Gothenburg, 2015.

[121] E. W. Weisstein, “Stadium,” *MathWorld - A Wolfram Web Resource*. https://mathworld.wolfram.com/Stadium.html (accessed Jul. 20, 2020).

[122] M. Trott, *The mathematica guidebook for symbolics*. Springer Science+Business Media, 2006.

APPENDIX A – RELEVANT SPRAY COMPARISONS

The following appendix section shows some spray comparisons at a quick glance for convenience by combining images in a single figure. This is simply done to compare results between the WC nozzle, and following tests using the single or dual injection PBI prototype. Note that parameters may change between sprays.

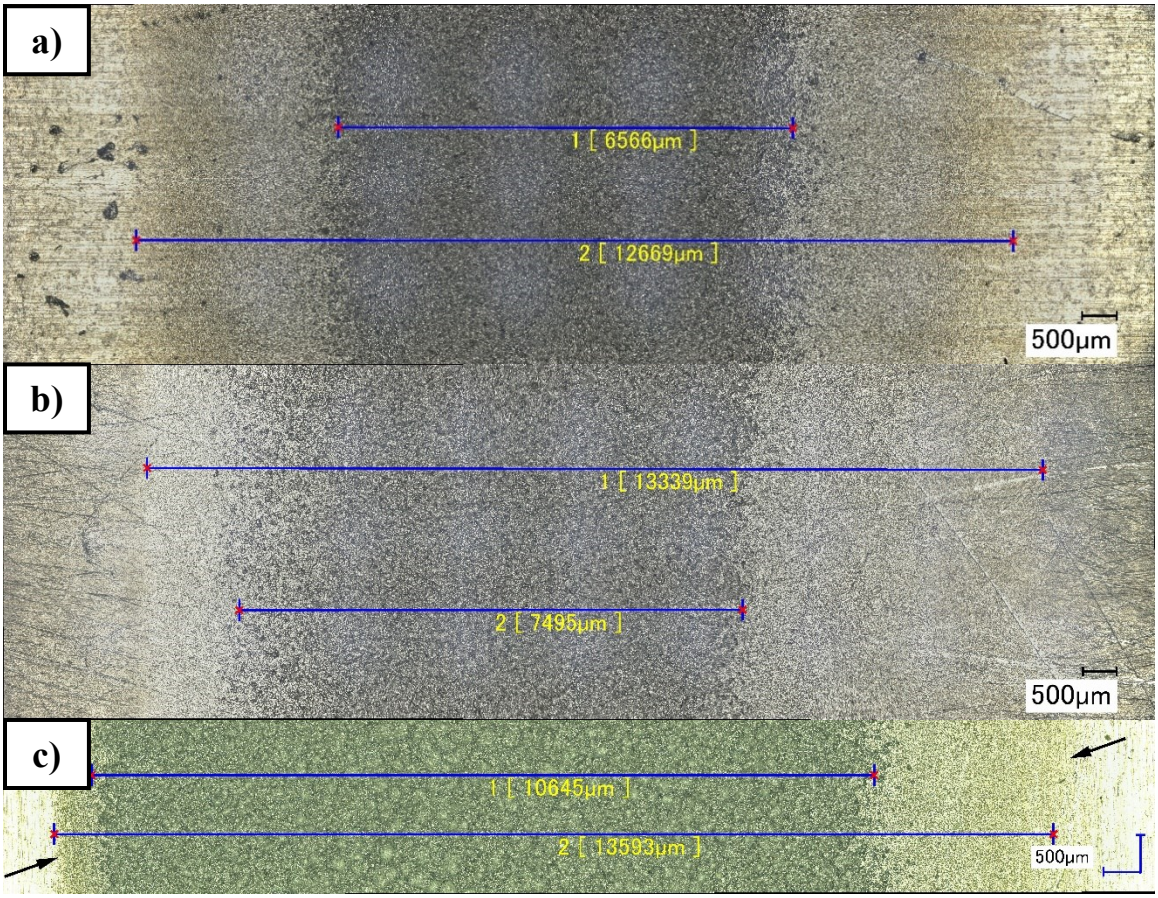

Figure A.1 – Initial prototype sprays on Al 6061-T6 substrate, a) WC nozzle (90° inlet), b) PBI nozzle (single 15° inlet), and c) PBI nozzle (dual 15° inlets)

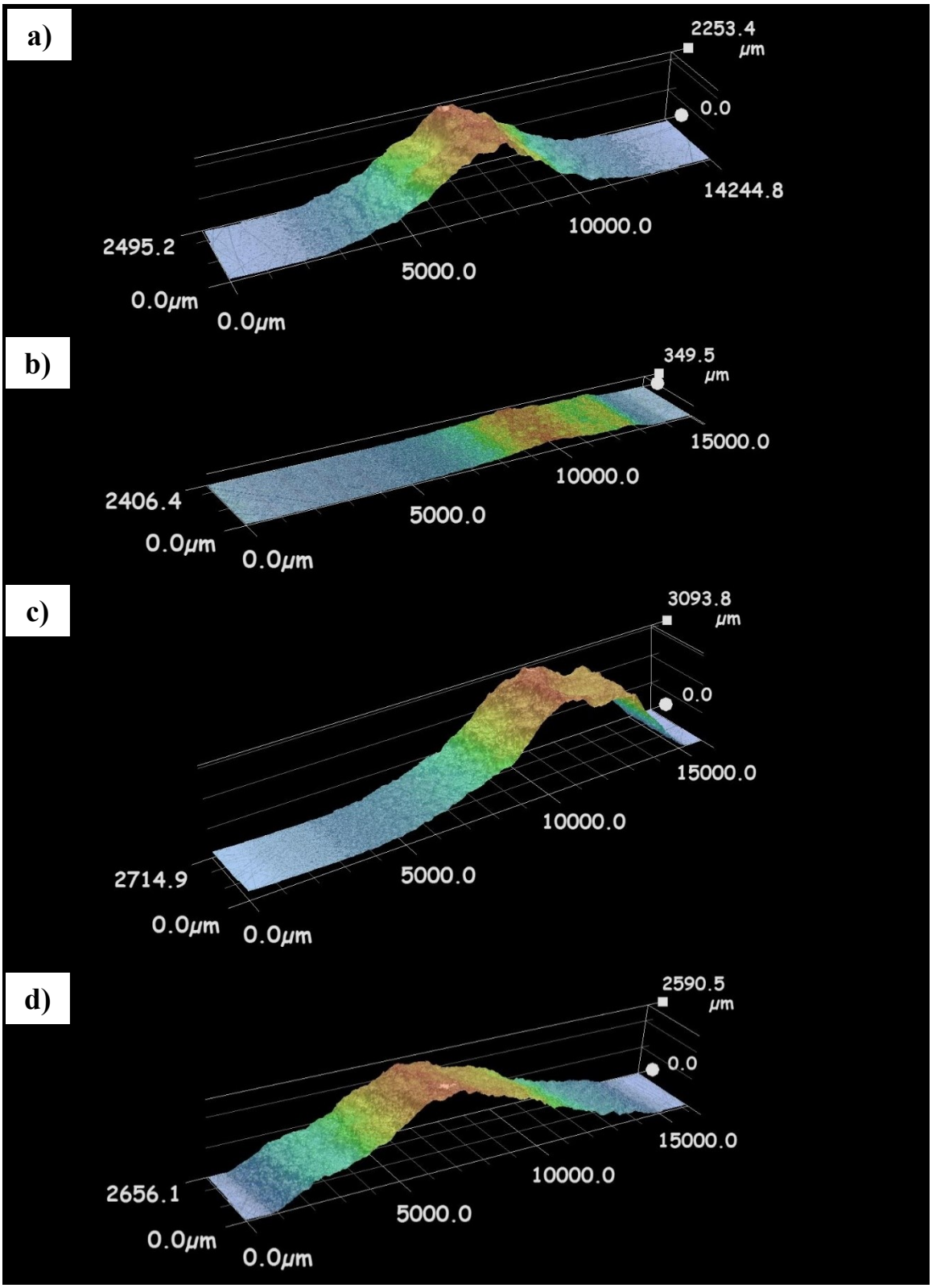

Figure A.2 – Comparison of 3D profiles from multi-pass coatings on Al 6061-T6, a) WC (90° inlet) at 300°C, b) PBI (single 15° inlet) at 300°C, c) PBI (single 15° inlet) at 500°C, d) PBI (dual 15° inlets) at 500°C

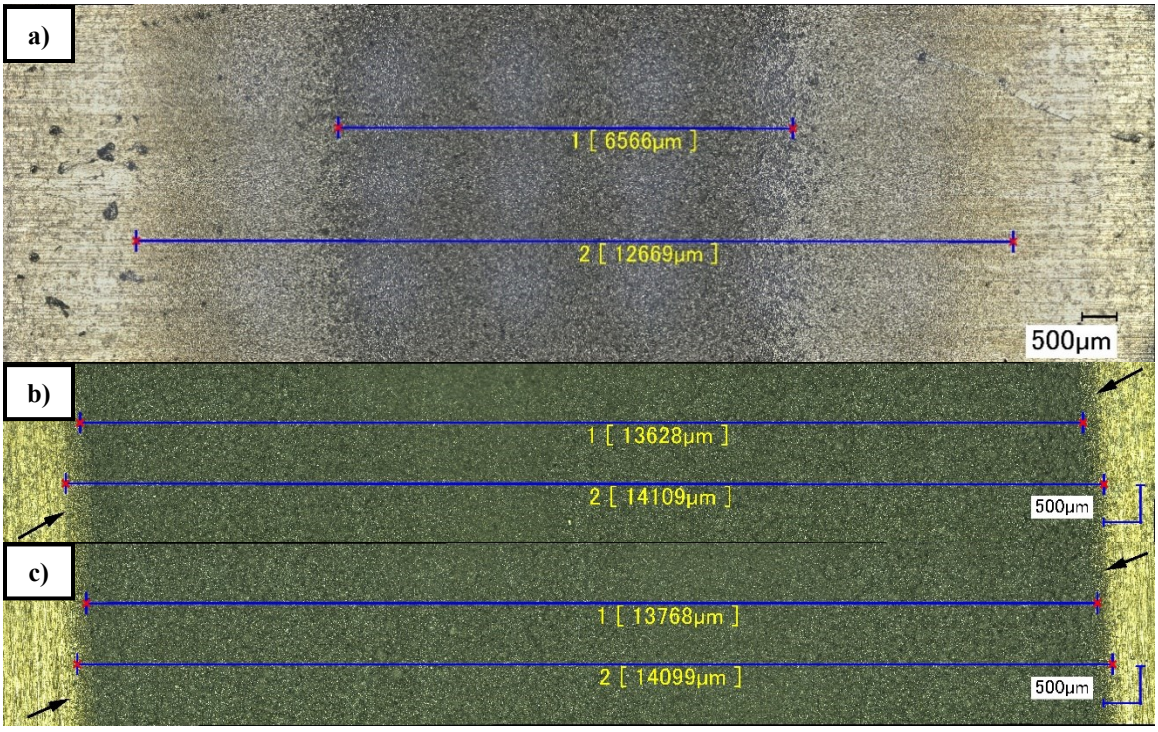

Figure A.3 – Comparison of single pass coatings on Al 6061-T6 substrate, a) WC (90° inlet), b) PBI (dual 15° inlet – $3.26x10^{-4}$ kg/s (30 SCFH)), c) PBI (dual 15° inlet – $6.52x10^{-4}$ kg/s (60 SCFH))

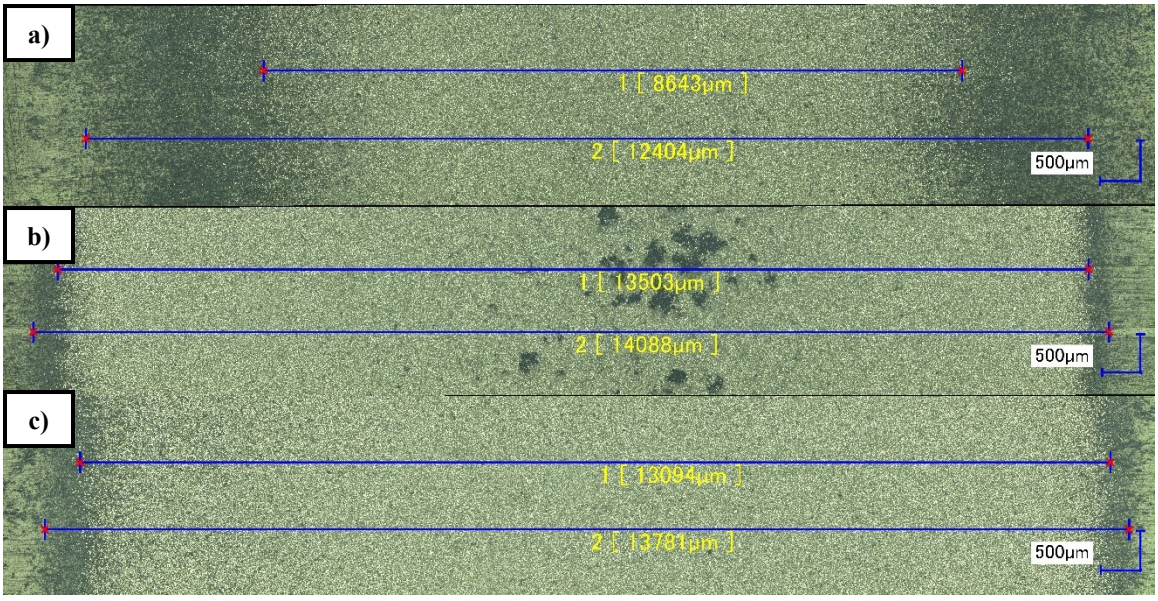

Figure A.4 – Comparison of single-pass coatings on polyamide substrate, a) WC (90° inlet), b) PBI (dual 15° inlet), c) PBI (dual 15° inlet) with optimized parameters

APPENDIX B – ALL PARTICLE SIMULATION RESULTS

This appendix section shows the simulation results of particle distribution at the nozzle outlet plane, for each particle diameter bin.

B.1 WC PROTOTYPE (90° INLET)

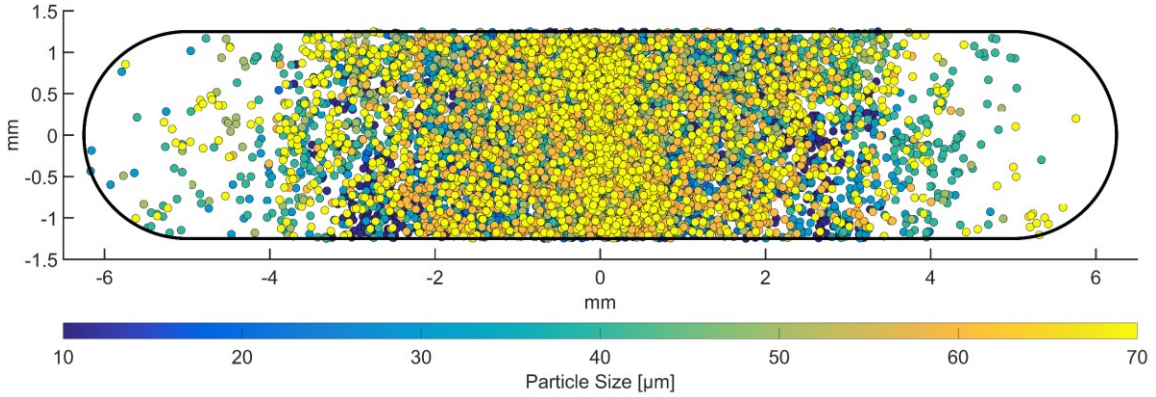

Figure B.1 – Full particle distribution for the WC prototype inlet (90°)

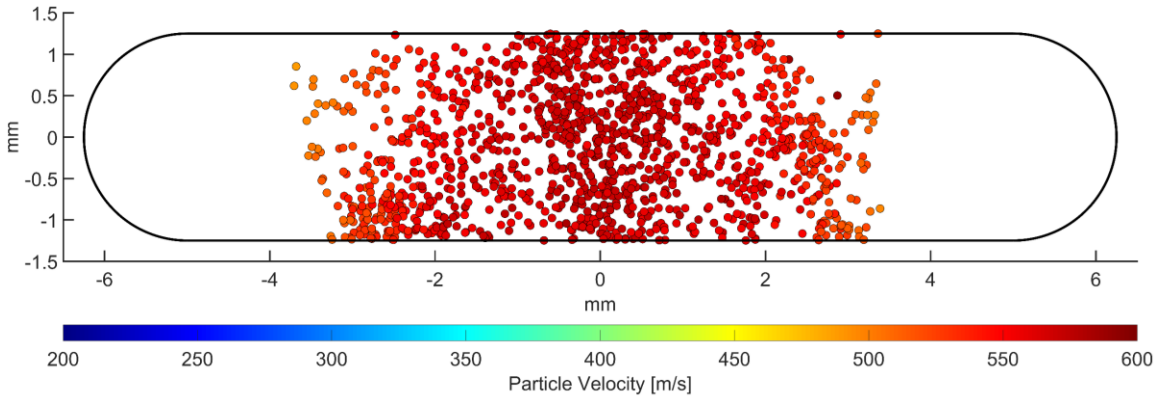

Figure B.2 – 10 µm particle distribution for WC prototype inlet (90°)

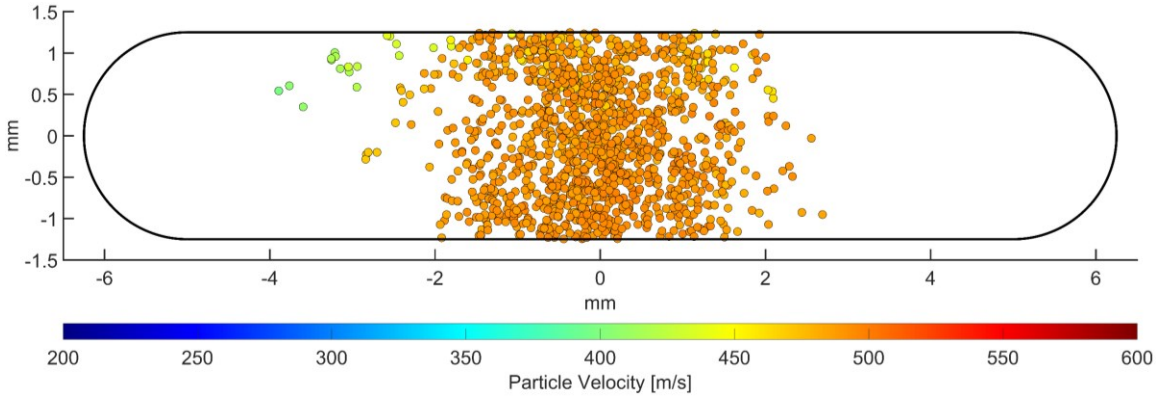

Figure B.3 – 20 µm particle distribution for WC prototype inlet (90°)

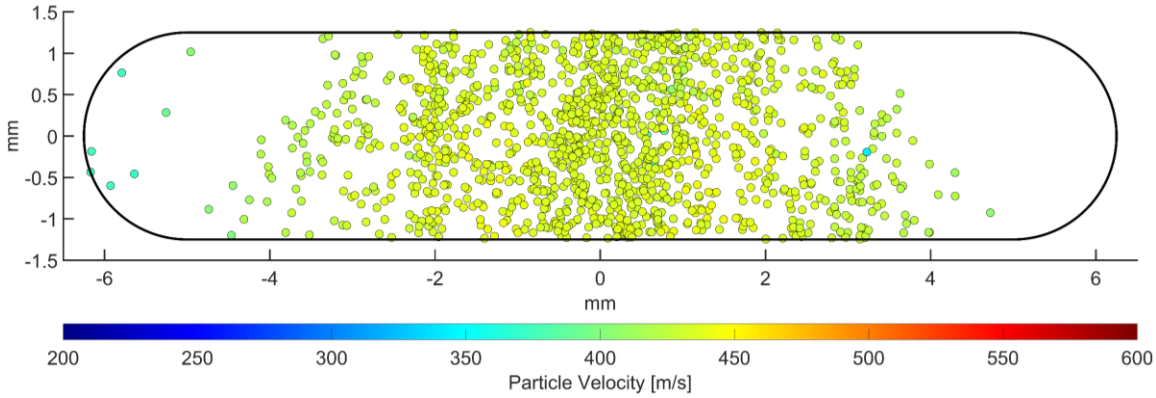

Figure B.4 – 30 µm particle distribution for WC prototype inlet (90°)

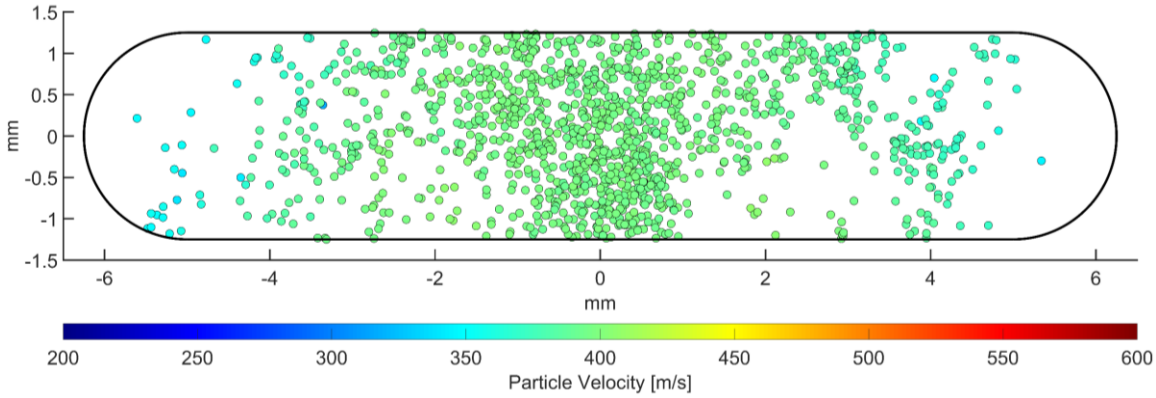

Figure B.5 – 40 µm particle distribution for WC prototype inlet (90°)

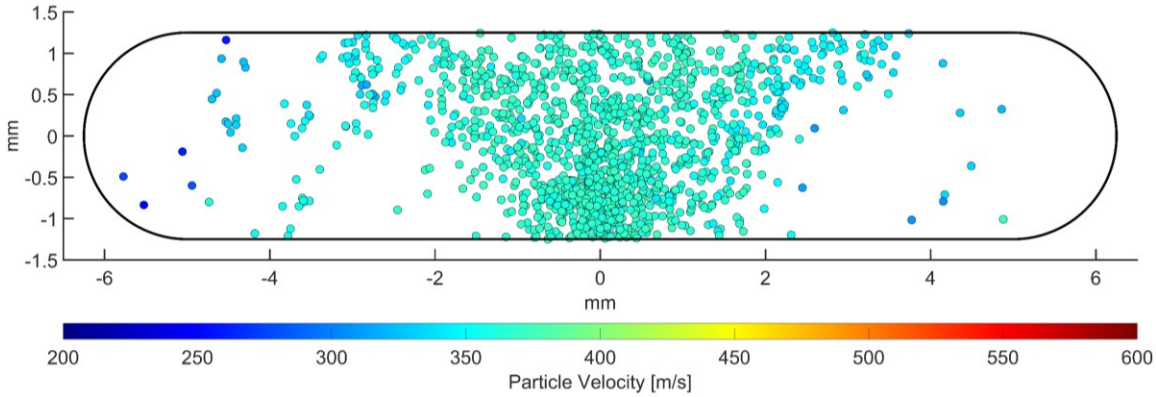

Figure B.6 – 50 µm particle distribution for WC prototype inlet (90°)

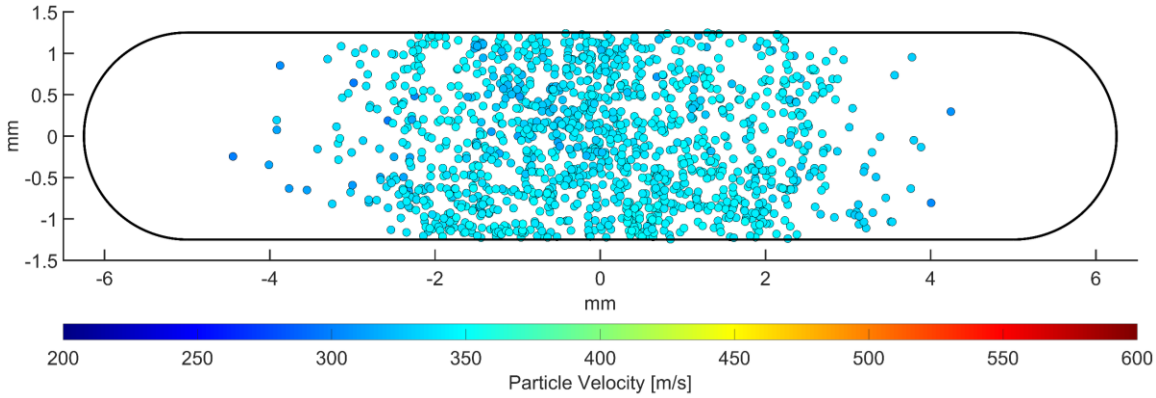

Figure B.7 – 60 µm particle distribution for WC prototype inlet (90°)

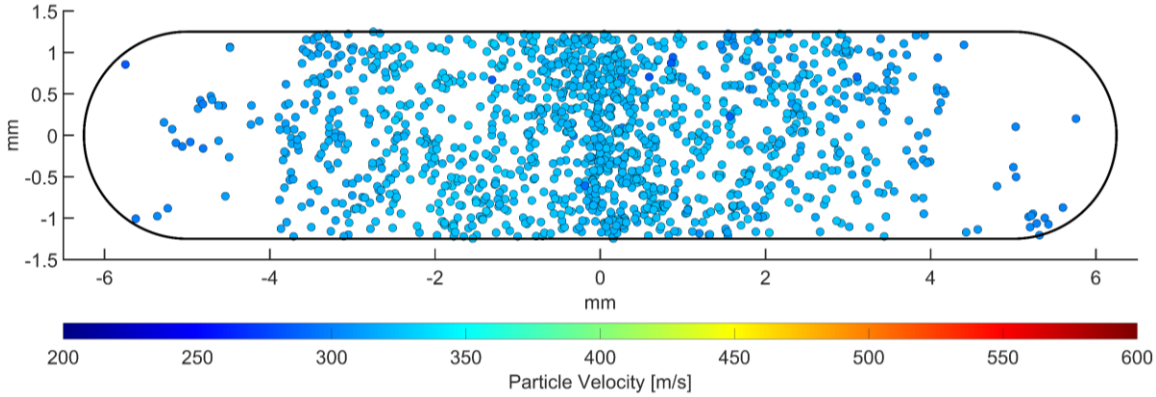

Figure B.8 – 70 µm particle distribution for WC prototype inlet (90°)

B.2 SIDE (0°) INLET

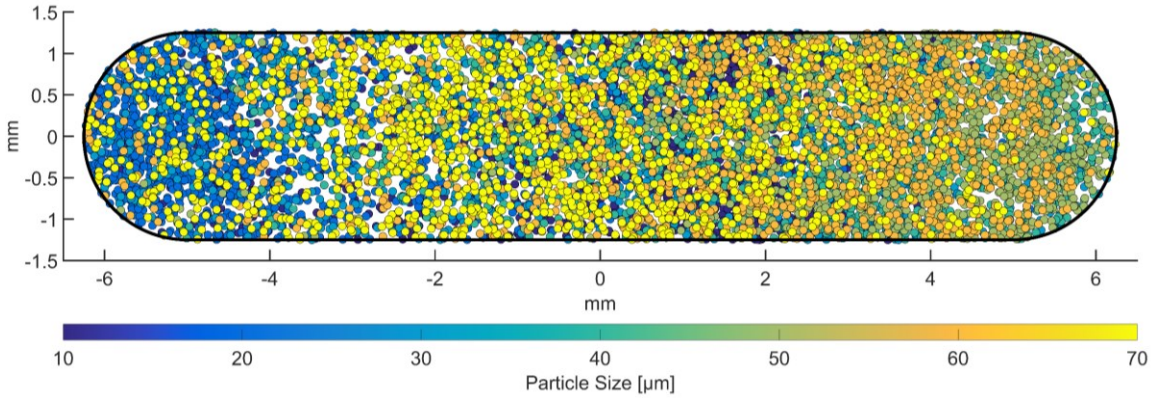

Figure B.9 – Full particle distribution for the side inlet (0°)

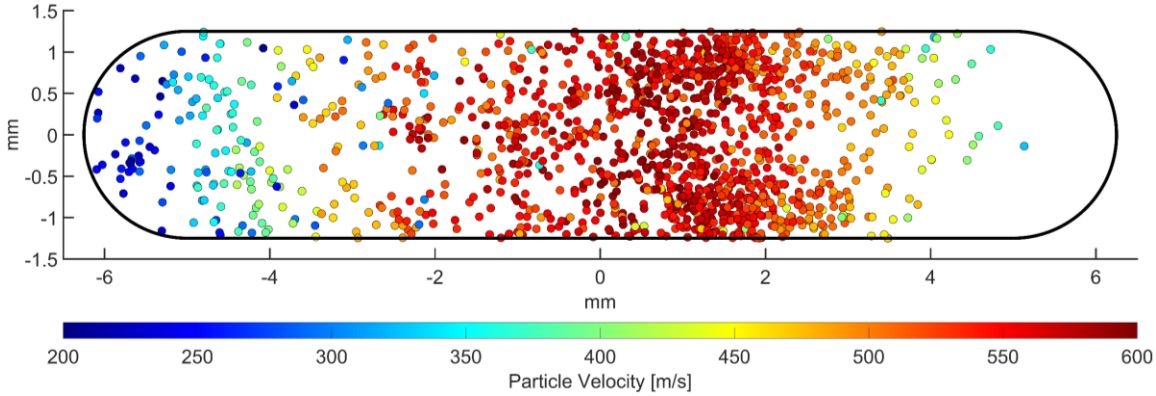

Figure B.10 – 10 µm particle distribution for the side inlet (0°)

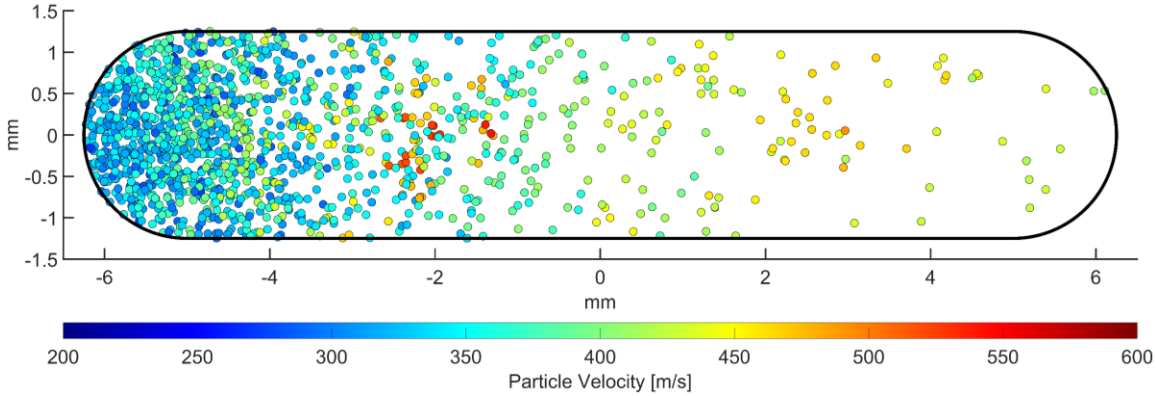

Figure B.11 – 20 µm particle distribution for the side inlet (0°)

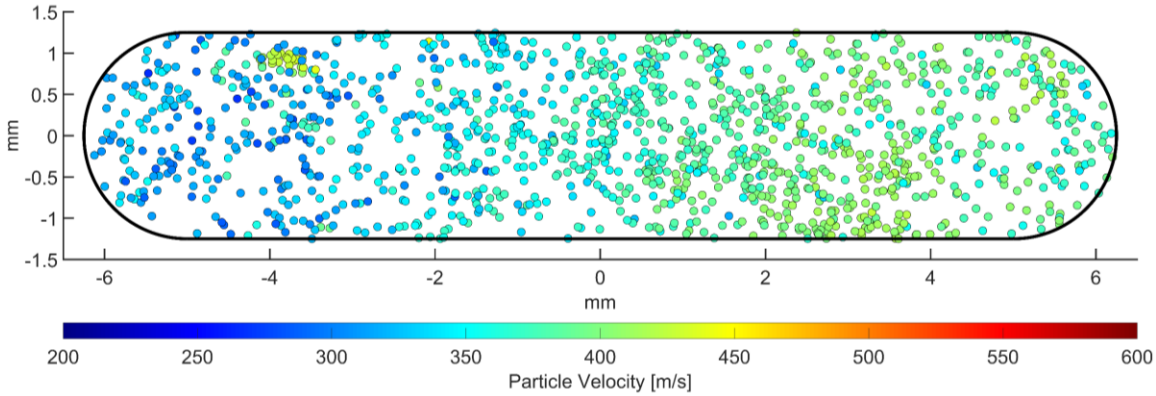

Figure B.12 – 30 µm particle distribution for the side inlet (0°)

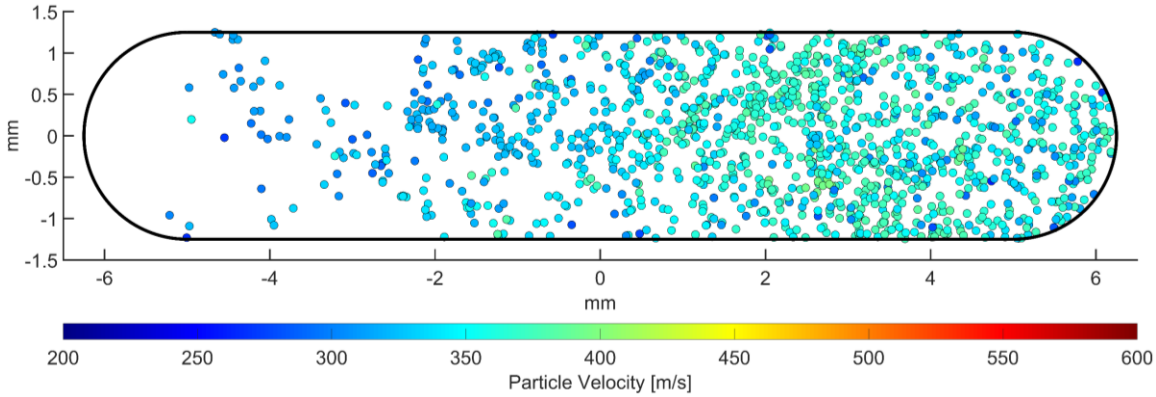

Figure B.13 – 40 µm particle distribution for the side inlet (0°)

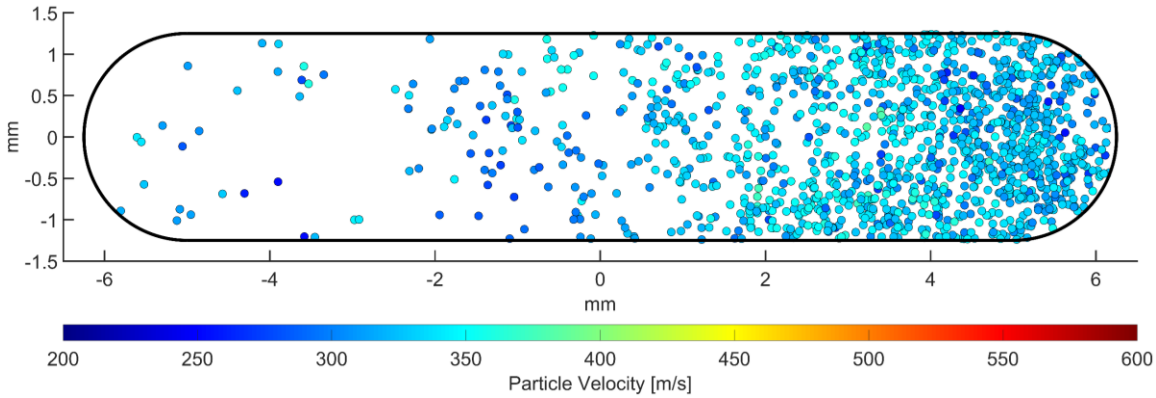

Figure B.14 – 50 µm particle distribution for the side inlet (0°)

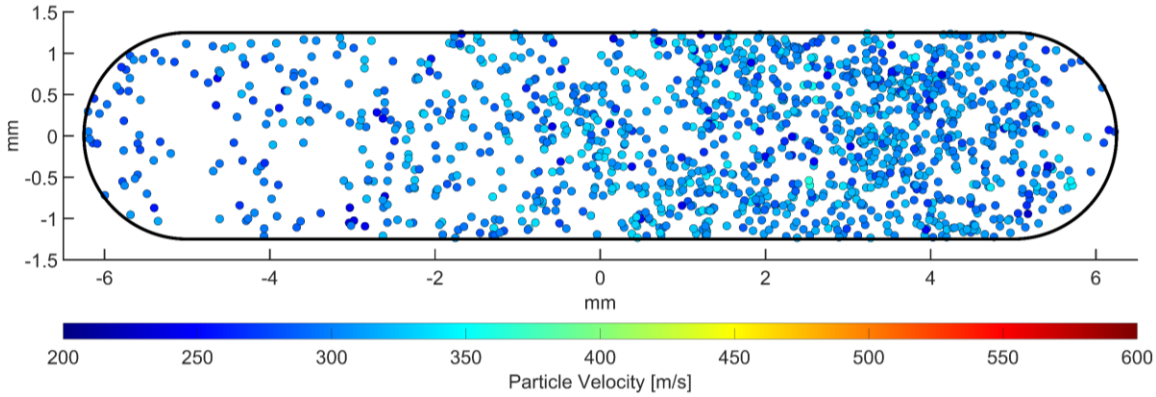

Figure B.15 – 60 µm particle distribution for the side inlet (0°)

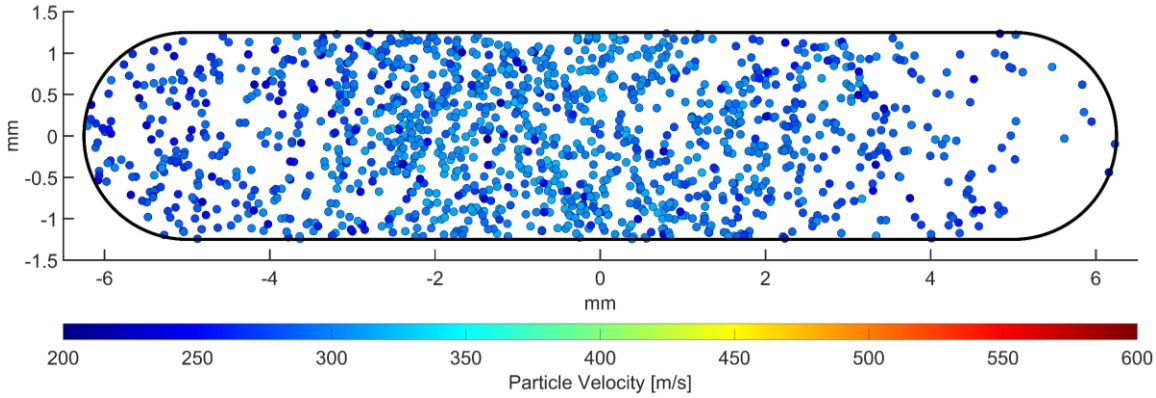

Figure B.16 – 70 µm particle distribution for the side inlet (0°)

B.3 15° INLET

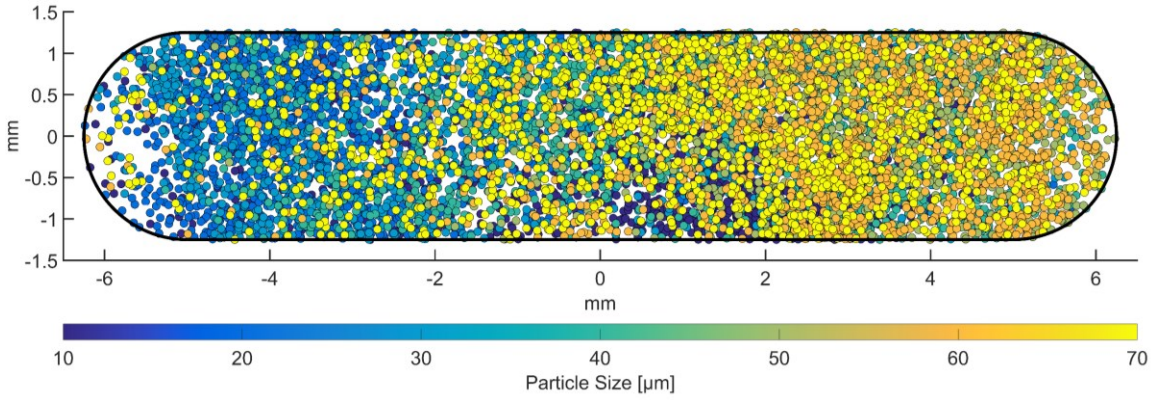

Figure B.17 – Full particle distribution for the 15° inlet

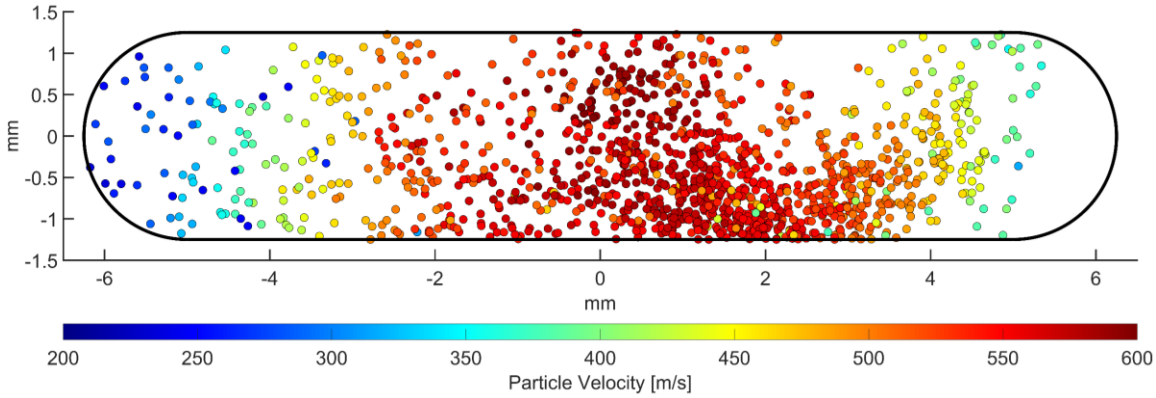

Figure B.18 – 10 µm particle distribution for the 15° inlet

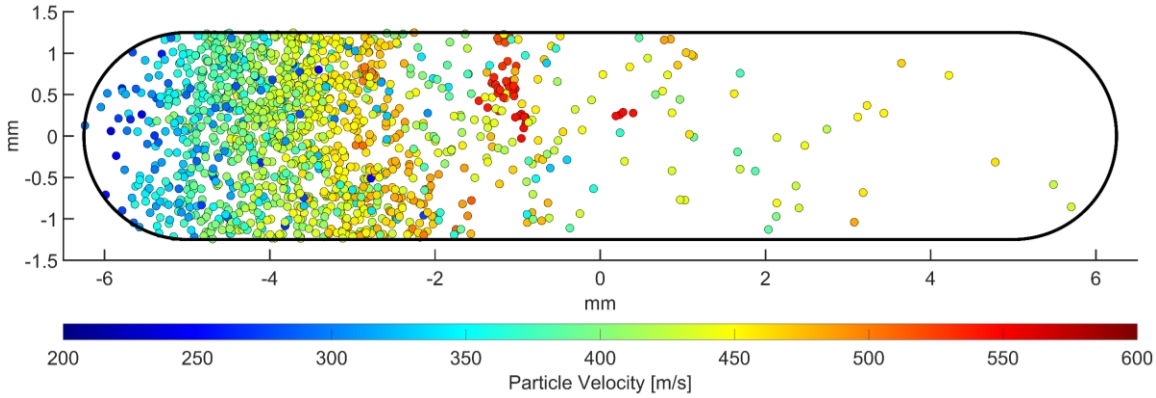

Figure B.19 – 20 µm particle distribution for the 15° inlet

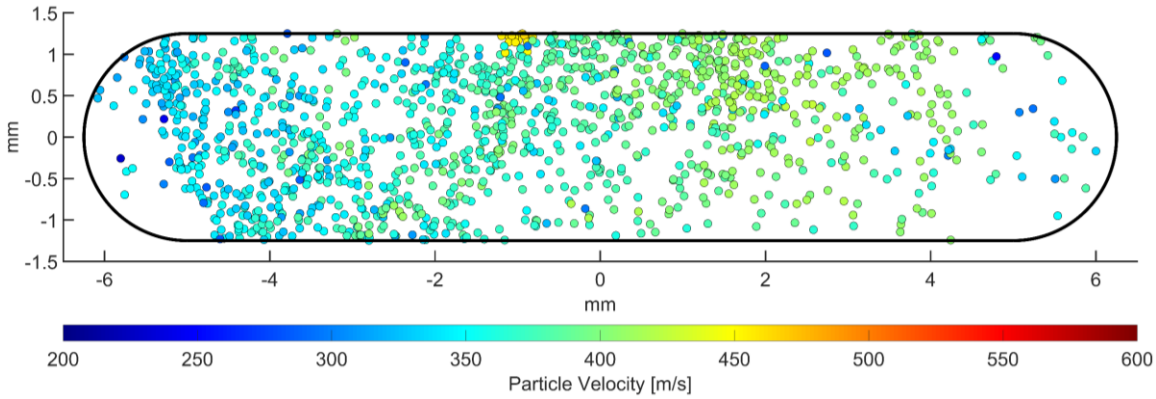

Figure B.20 – 30 µm particle distribution for the 15° inlet

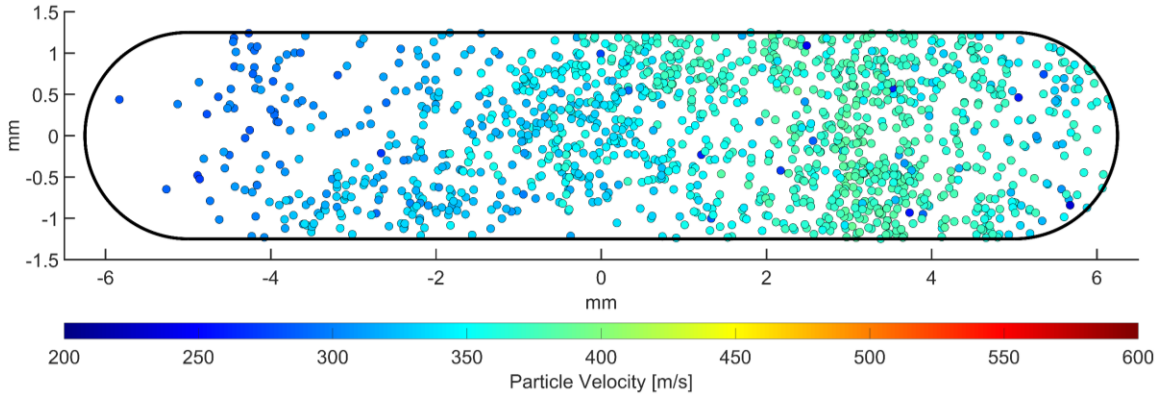

Figure B.21 – 40 µm particle distribution for the 15° inlet

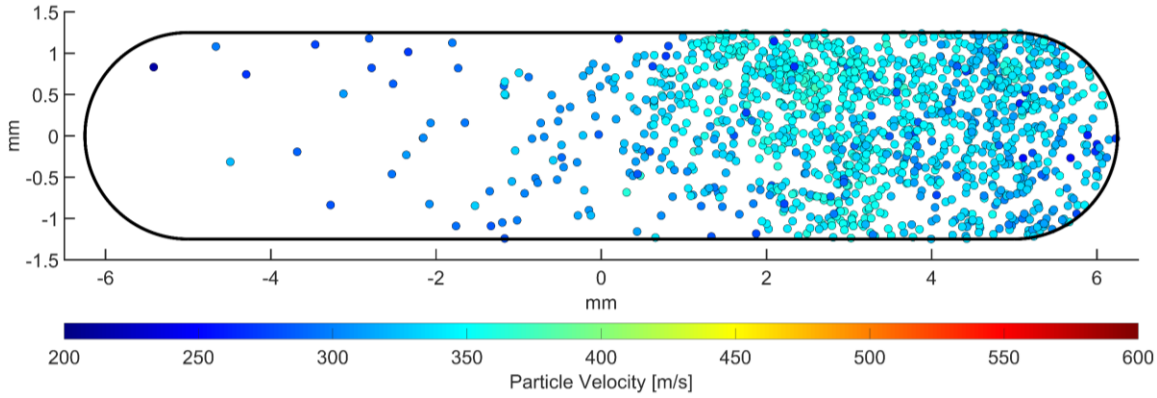

Figure B.22 – 50 µm particle distribution for the 15° inlet

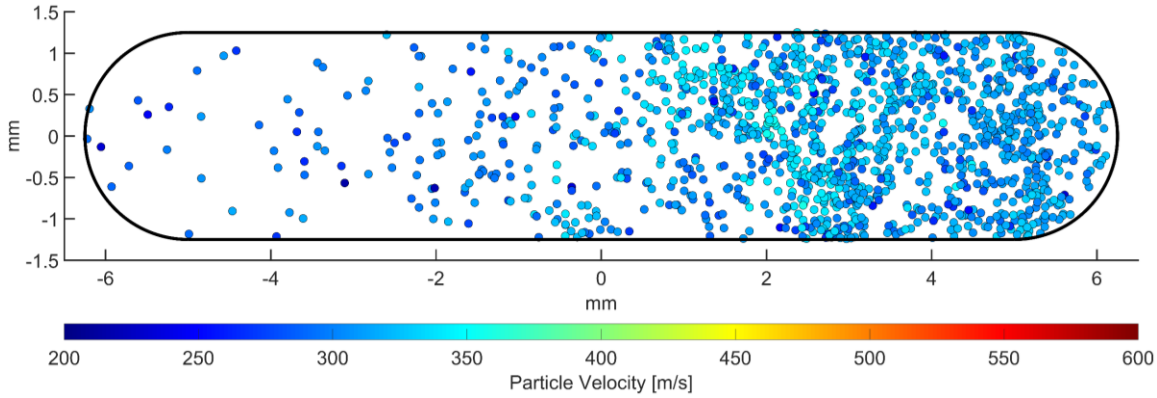

Figure B.23 – 60 µm particle distribution for the 15° inlet

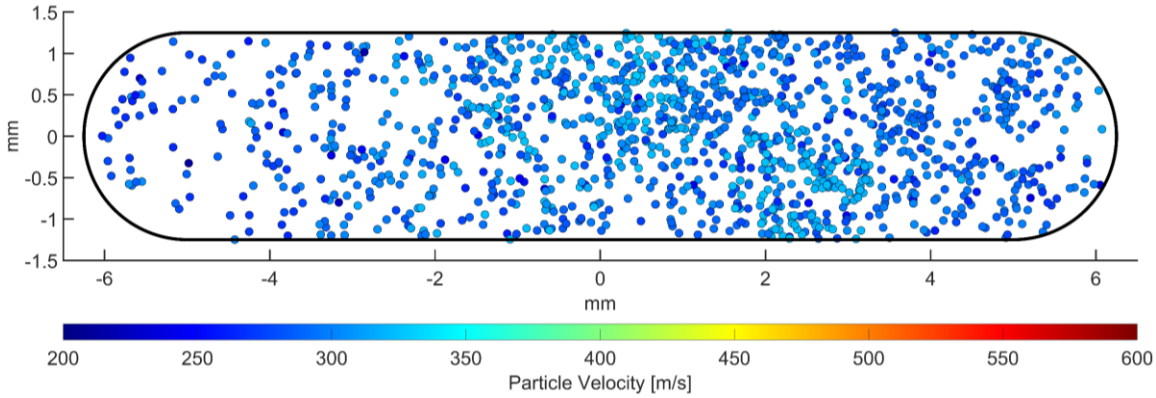

Figure B.24 – 70 µm particle distribution for the 15° inlet

B.4 30° INLET

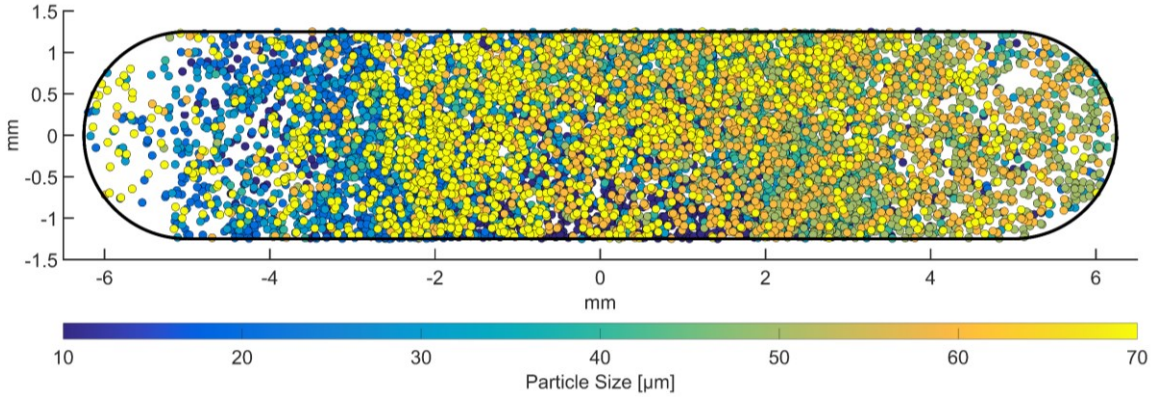

Figure B.25 – Full particle distribution for the 30° inlet

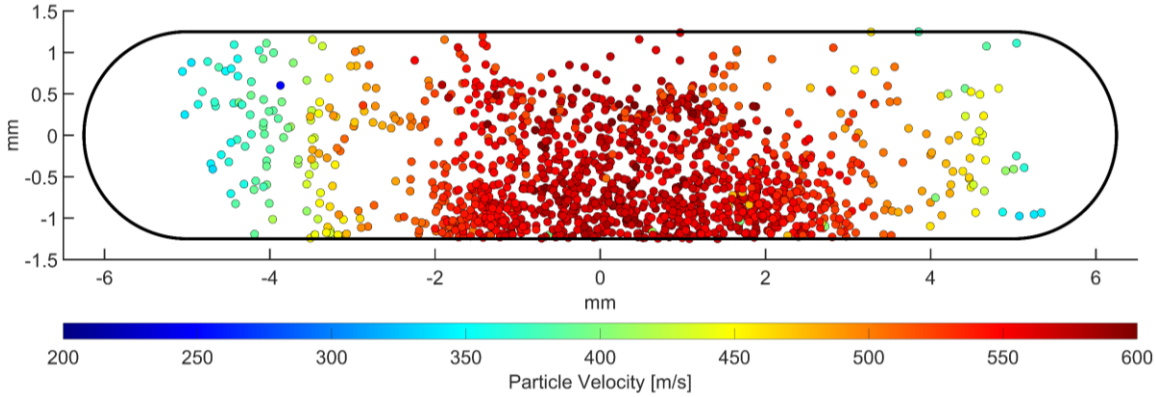

Figure B.26 – 10 µm particle distribution for the 30° inlet

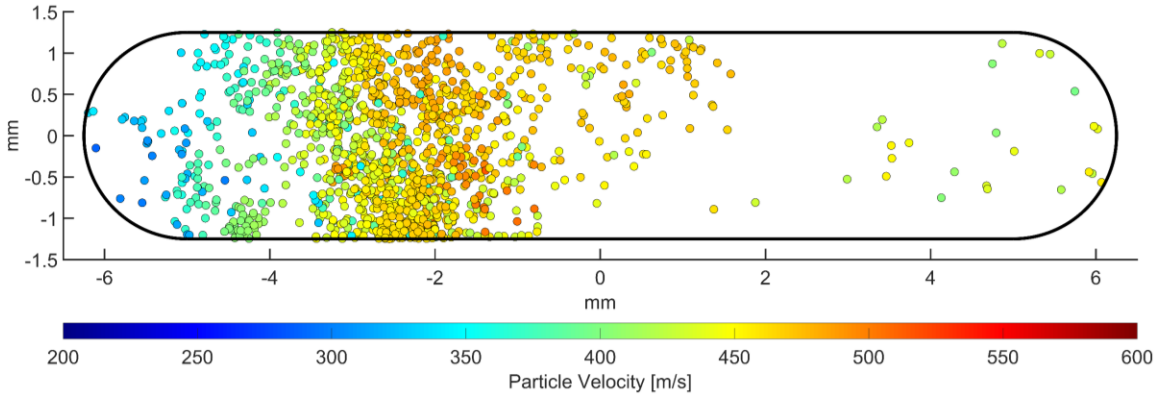

Figure B.27 – 20 µm particle distribution for the 30° inlet

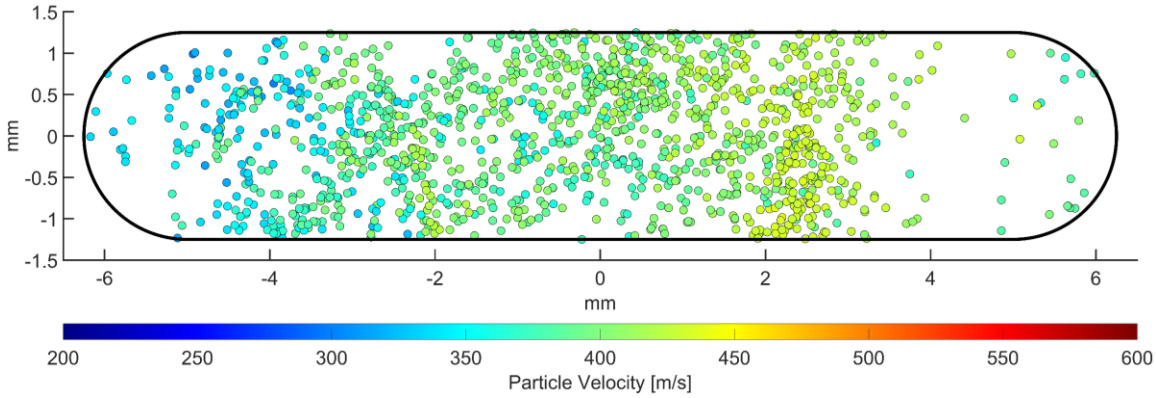

Figure B.28 – 30 µm particle distribution for the 30° inlet

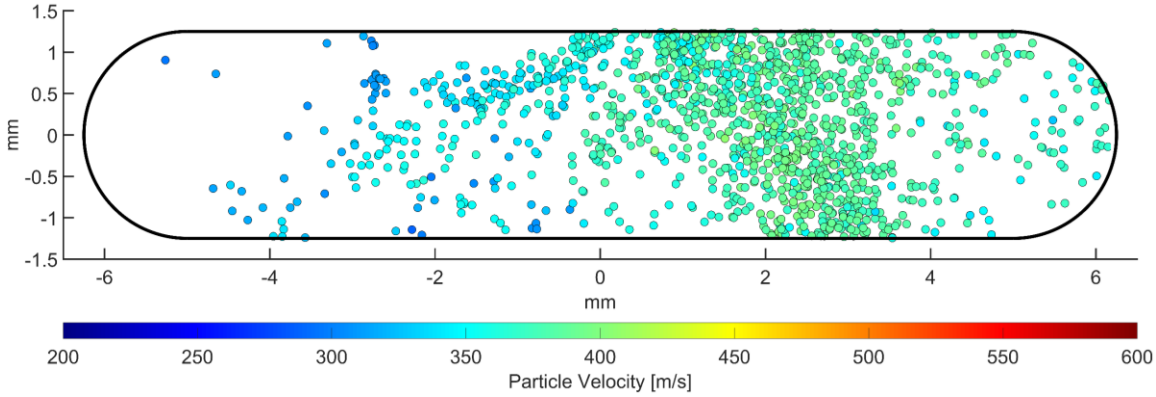

Figure B.29 – 40 µm particle distribution for the 30° inlet

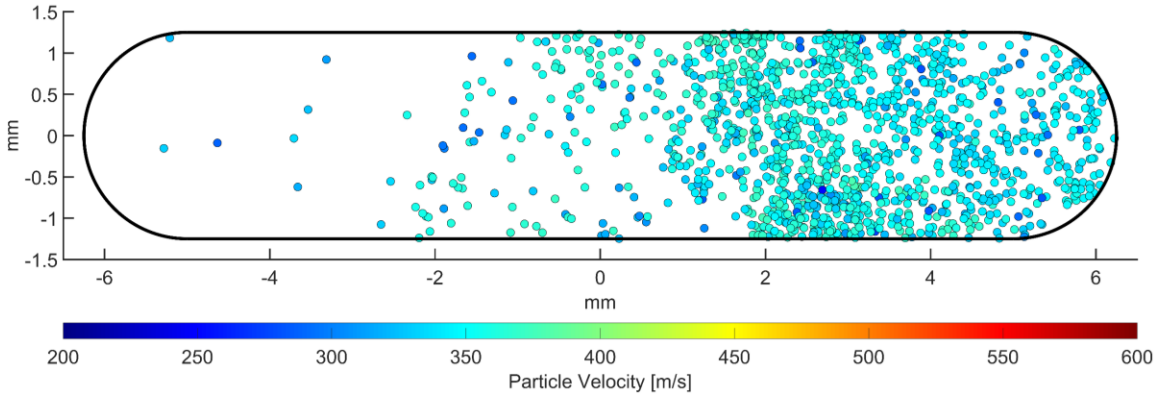

Figure B.30 – 50 µm particle distribution for the 30° inlet

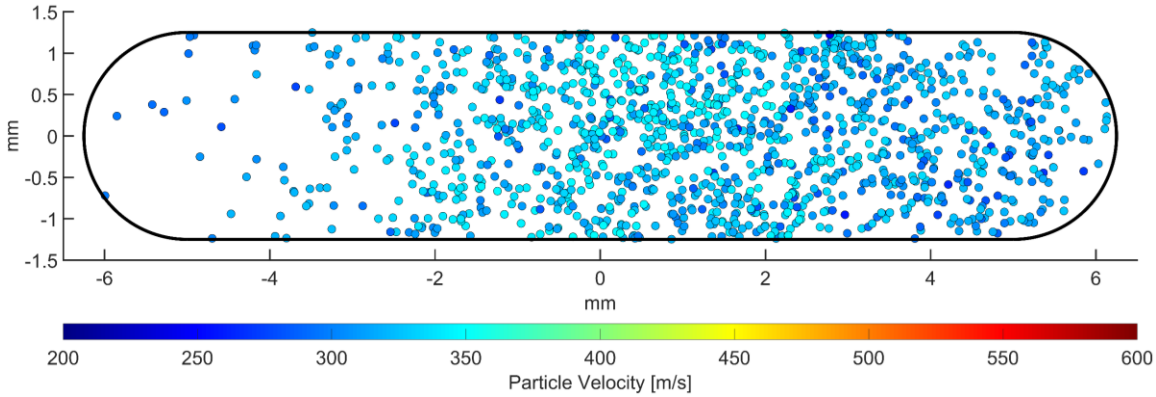

Figure B.31 – 60 µm particle distribution for the 30° inlet

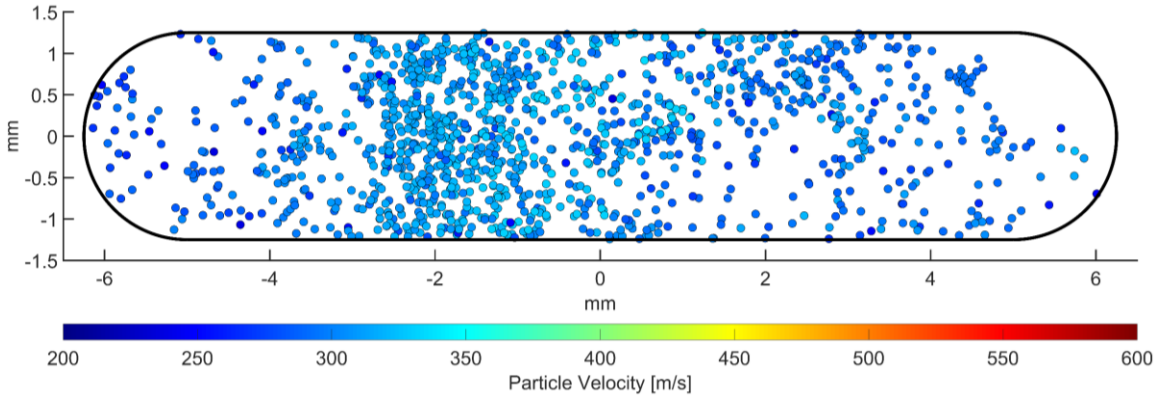

Figure B.32 – 70 µm particle distribution for the 30° inlet

B.5 45° INLET

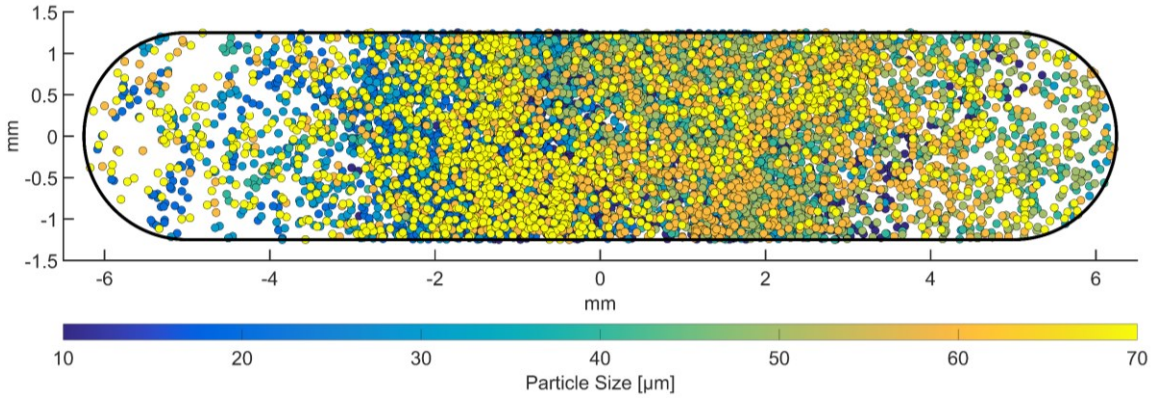

Figure B.33 – Full particle distribution for the 45° inlet

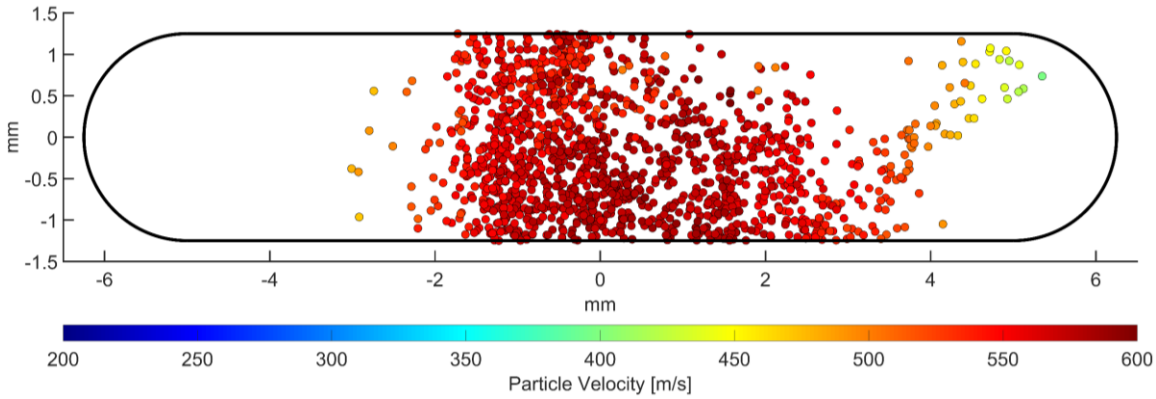

Figure B.34 – 10 µm particle distribution for the 45° inlet

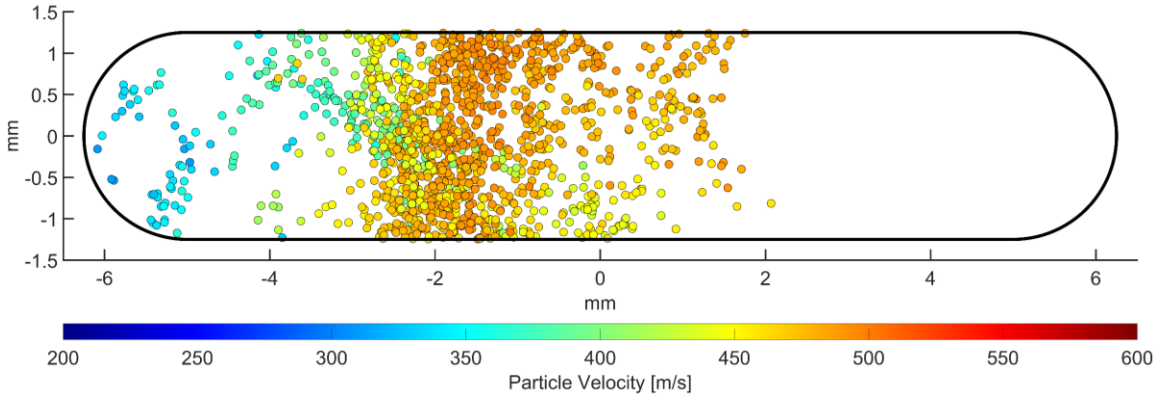

Figure B.35 – 20 µm particle distribution for the 45° inlet

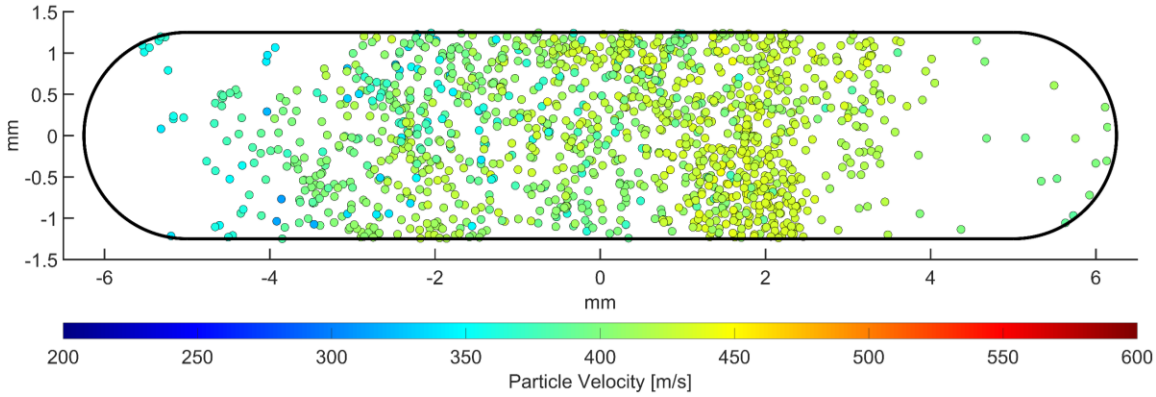

Figure B.36 – 30 µm particle distribution for the 45° inlet

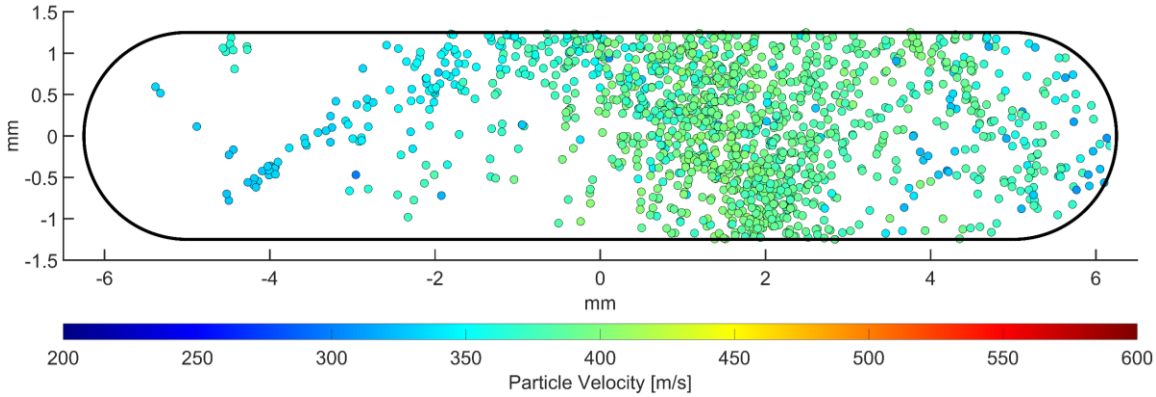

Figure B.37 – 40 µm particle distribution for the 45° inlet

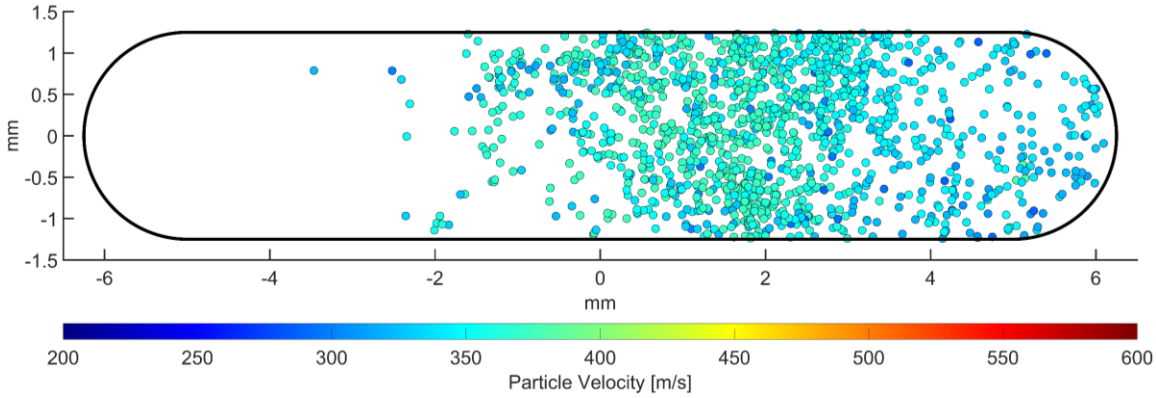

Figure B.38 – 50 µm particle distribution for the 45° inlet

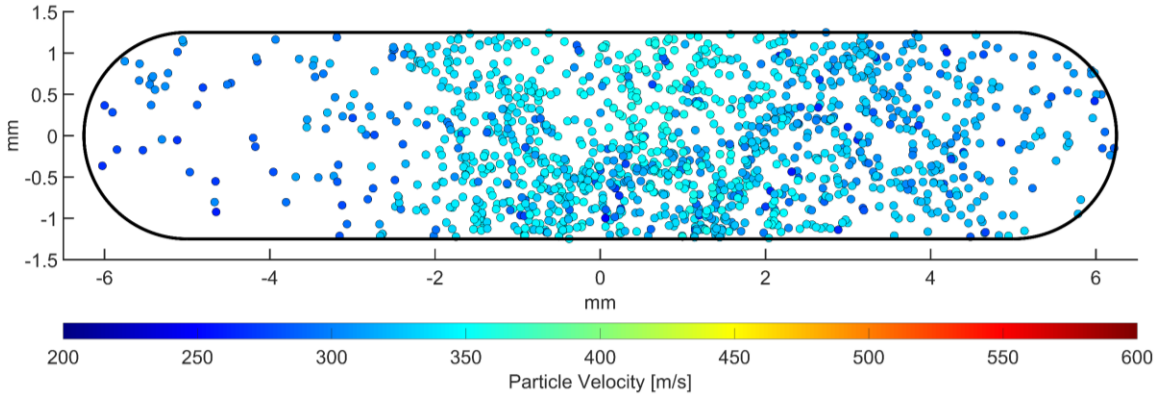

Figure B.39 – 60 µm particle distribution for the 45° inlet

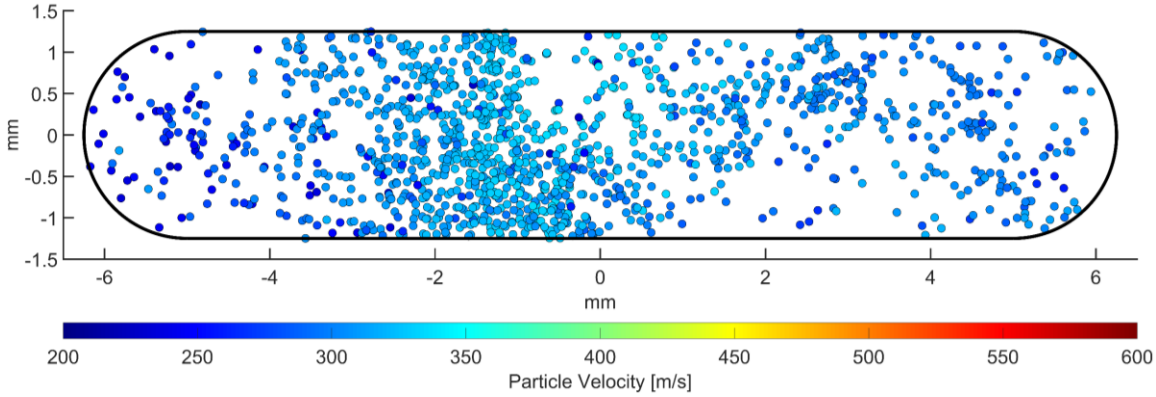

Figure B.40 – 70 µm particle distribution for the 45° inlet

B.6 DUAL 15° INLET – 3.26X10^{-4} KG/S (30 SCFH)

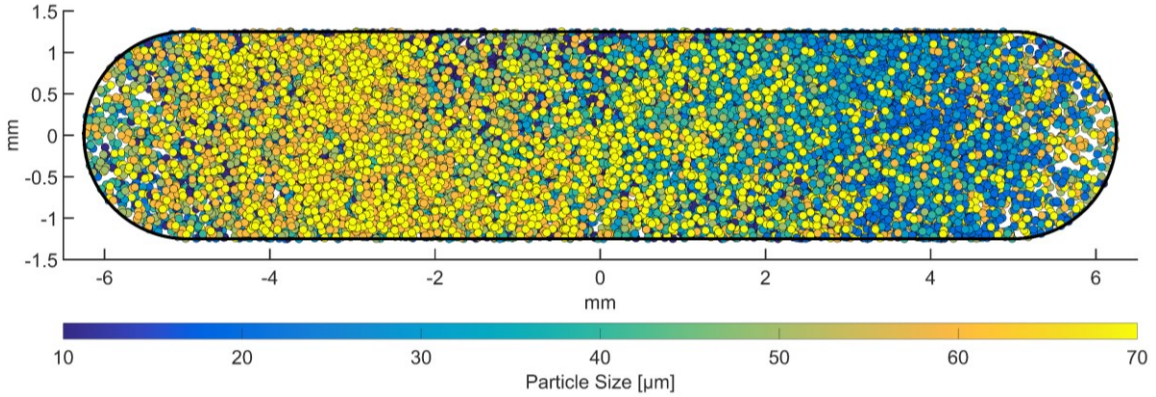

Figure B.41 – Full particle distribution for the dual injection 15° inlets at 3.26x10^{-4} kg/s (30 SCFH)

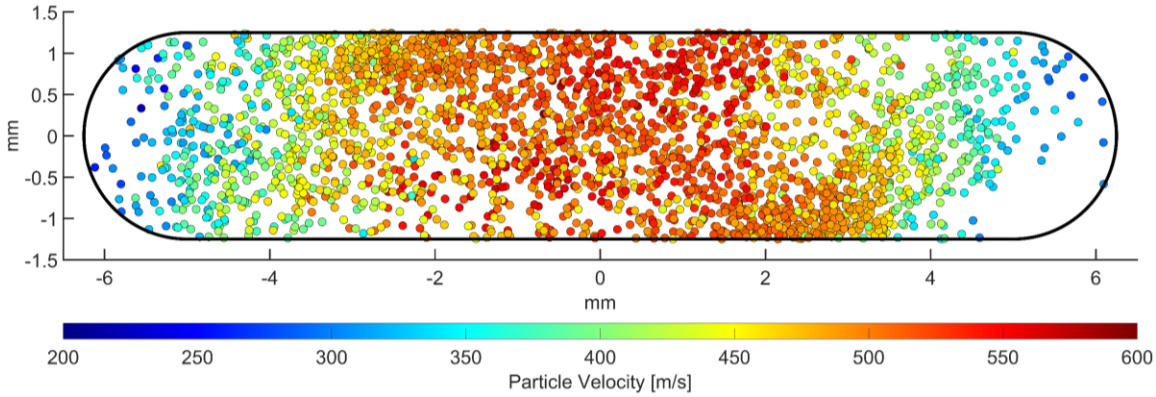

Figure B.42 – 10 µm particle distribution for the dual 15° inlets at 3.26x10^{-4} kg/s (30 SCFH)

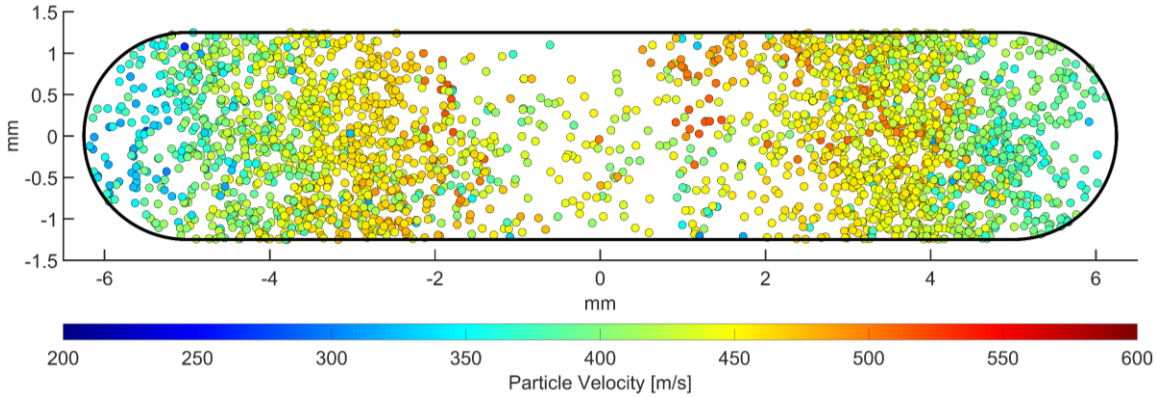

Figure B.43 – 20 µm particle distribution for the dual 15° inlets at 3.26x10^{-4} kg/s (30 SCFH)

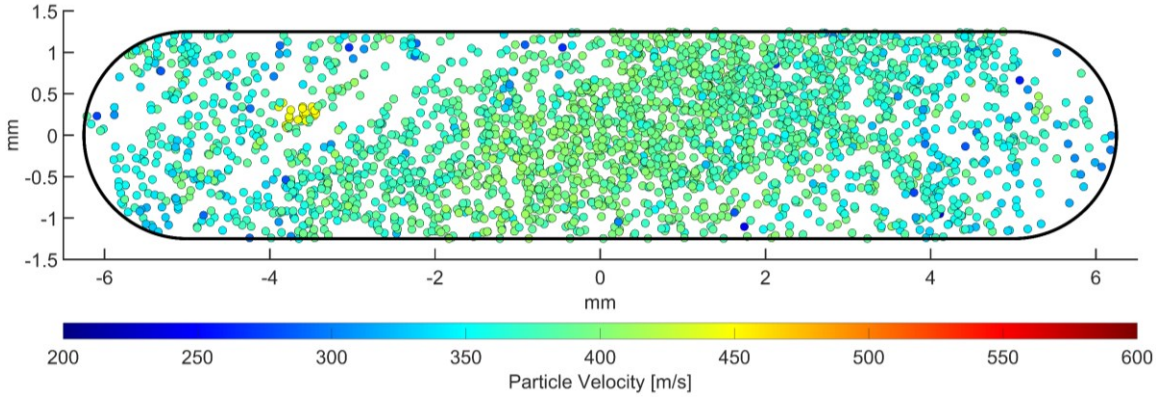

Figure B.44 – 30 µm particle distribution for the dual 15° inlets at 3.26x10^{-4} kg/s (30 SCFH)

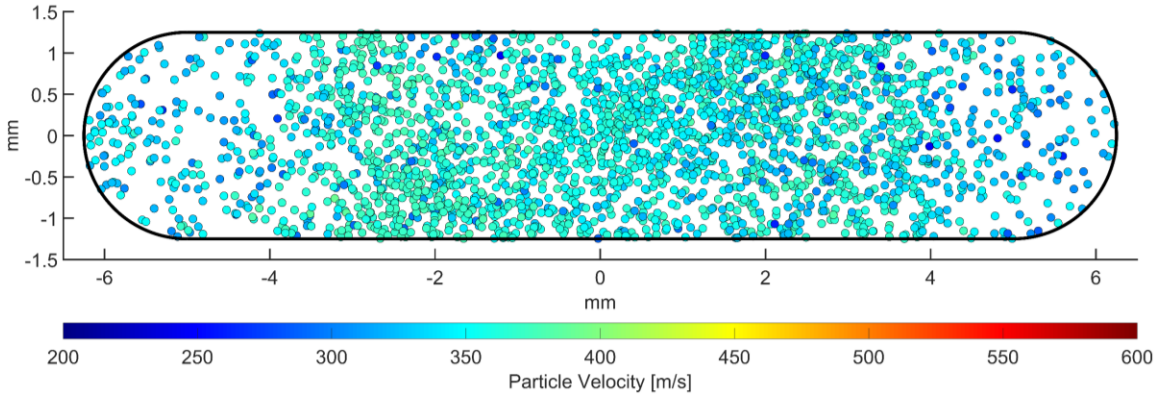

Figure B.45 – 40 µm particle distribution for the dual 15° inlets at 3.26x10^{-4} kg/s (30 SCFH)

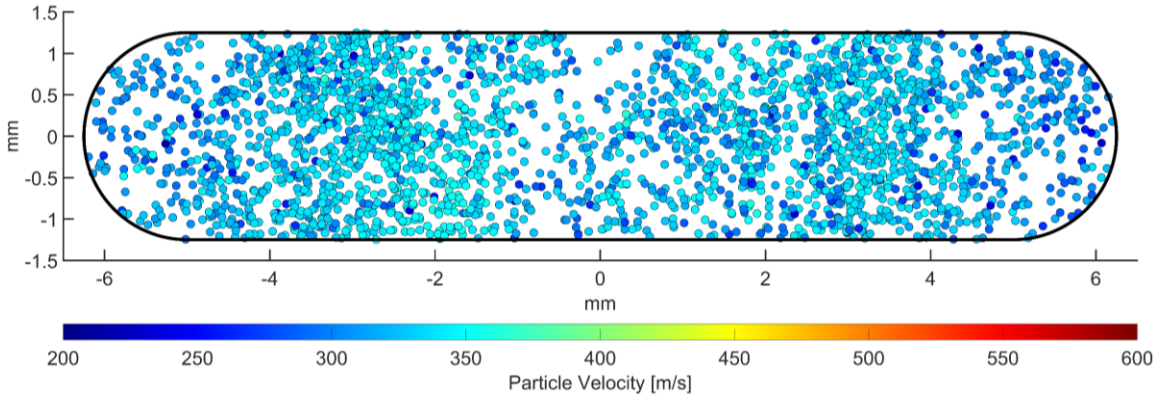

Figure B.46 – 50 µm particle distribution for the dual 15° inlets at 3.26x10^{-4} kg/s (30 SCFH)

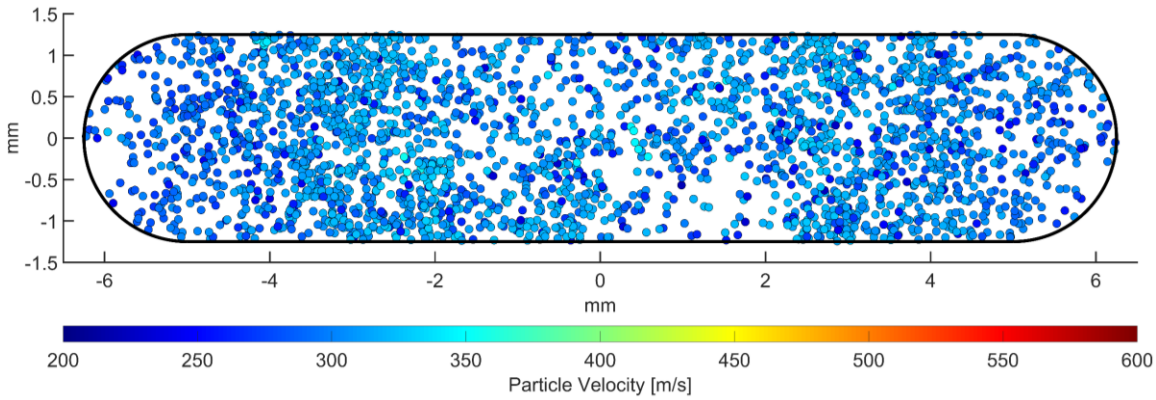

Figure B.47 – 60 µm particle distribution for the dual 15° inlets at 3.26x10^{-4} kg/s (30 SCFH)

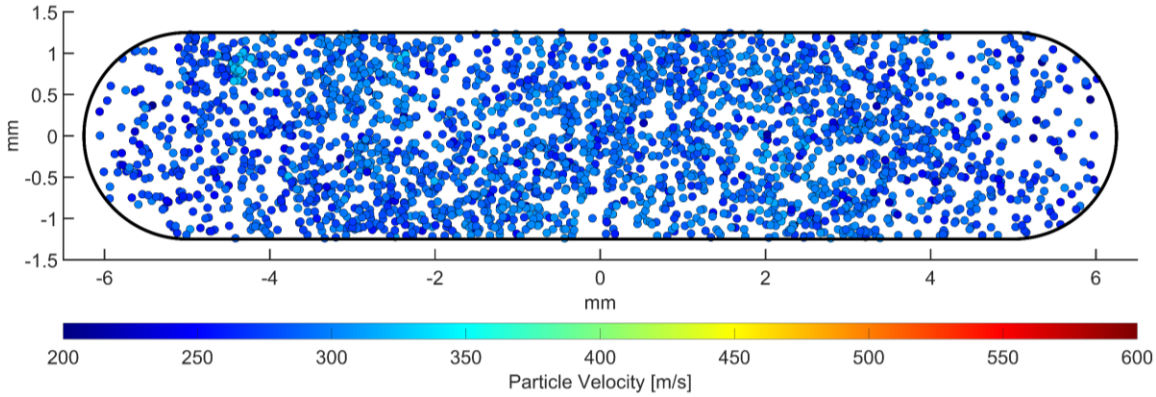

Figure B.48 – 70 µm particle distribution for the dual 15° inlets at 3.26x10^{-4} kg/s (30 SCFH)

B.7 DUAL 15° INLET – 6.52X10^{-4} KG/S (60 SCFH)

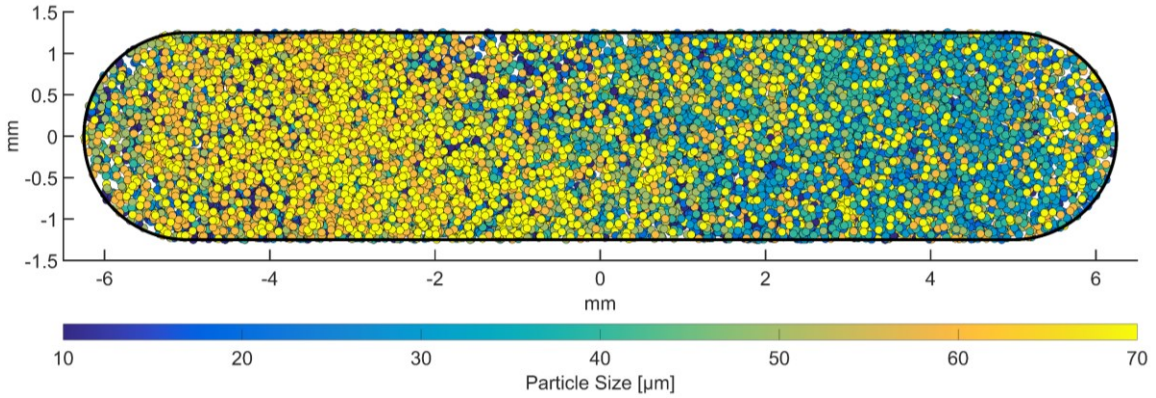

Figure B.49 – Full particle distribution for the dual injection 15° inlets at 6.52x10^{-4} kg/s (60 SCFH)

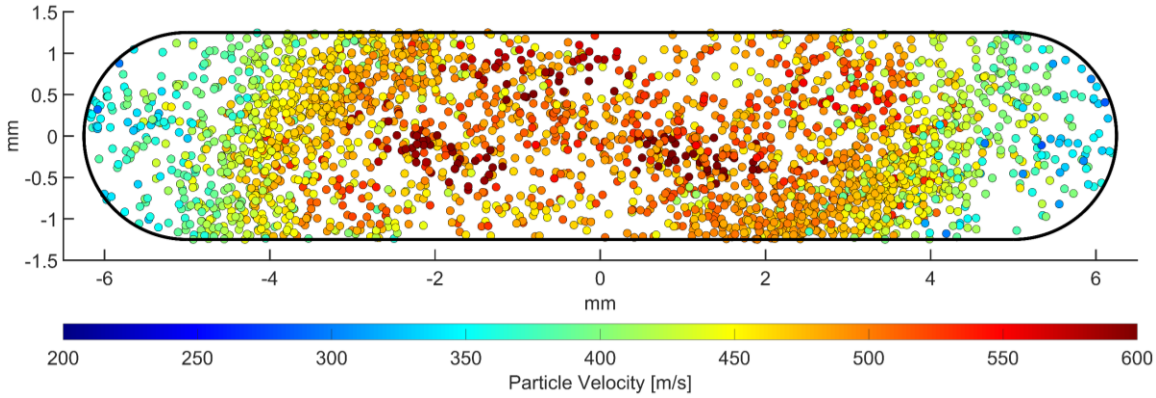

Figure B.50 – 10 µm particle distribution for the dual 15° inlets at 6.52x10^{-4} kg/s (60 SCFH)

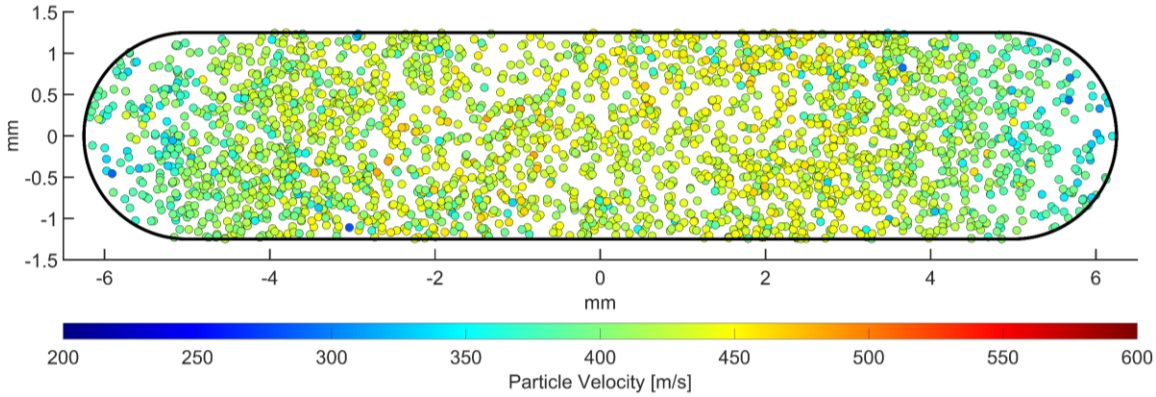

Figure B.51 – 20 µm particle distribution for the dual 15° inlets at 6.52x10^{-4} kg/s (60 SCFH)

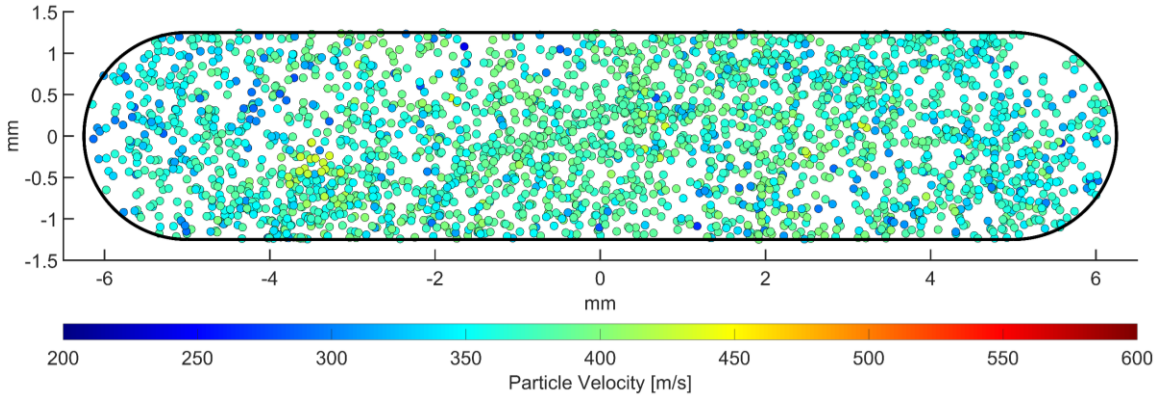

Figure B.52 – 30 µm particle distribution for the dual 15° inlets at 6.52x10^{-4} kg/s (60 SCFH)

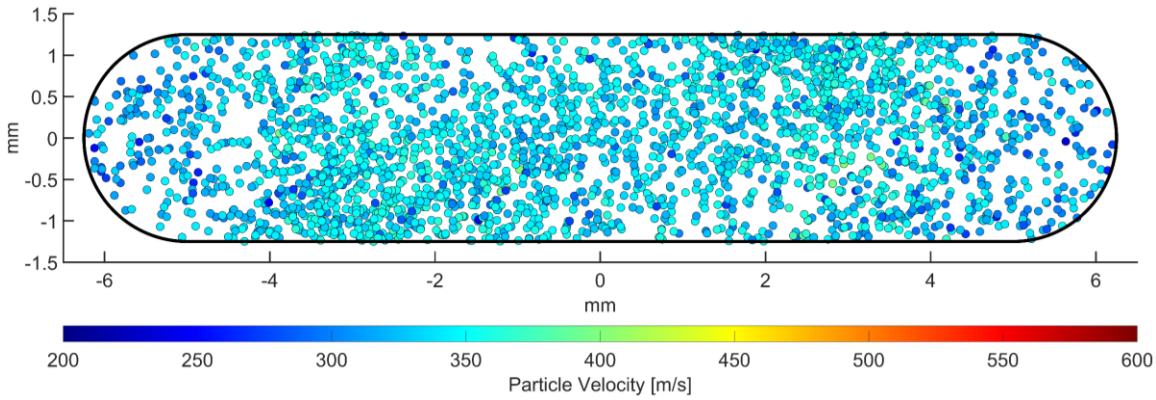

Figure B.53 – 40 µm particle distribution for the dual 15° inlets at 6.52x10^{-4} kg/s (60 SCFH)

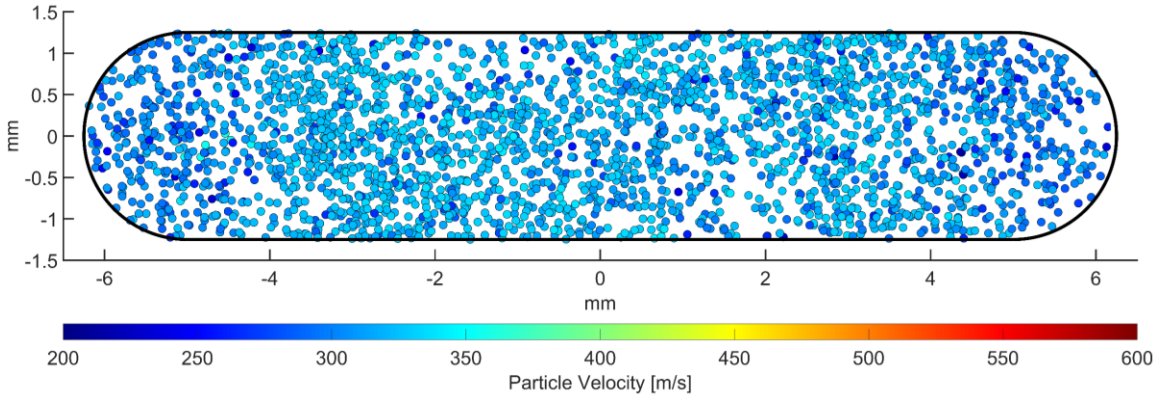

Figure B.54 – 50 µm particle distribution for the dual 15° inlets at 6.52x10^{-4} kg/s (60 SCFH)

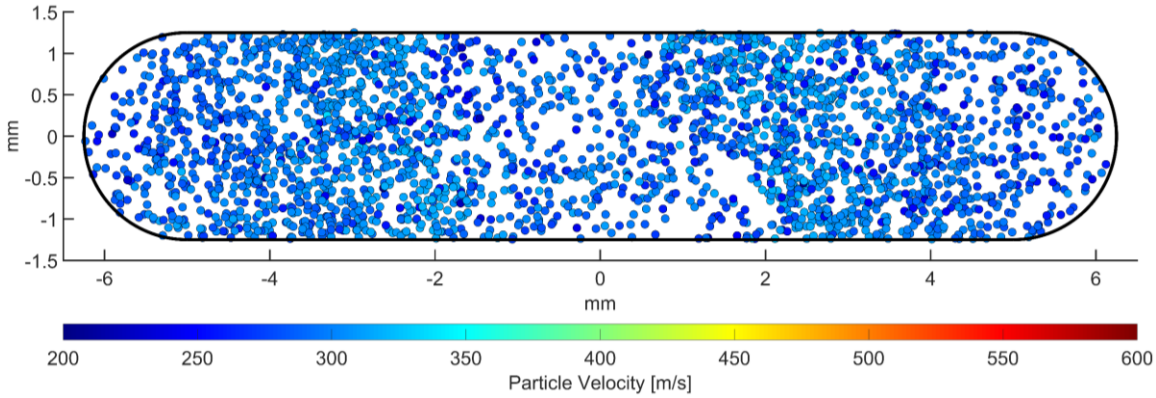

Figure B.55 – 60 µm particle distribution for the dual 15° inlets at 6.52x10^{-4} kg/s (60 SCFH)

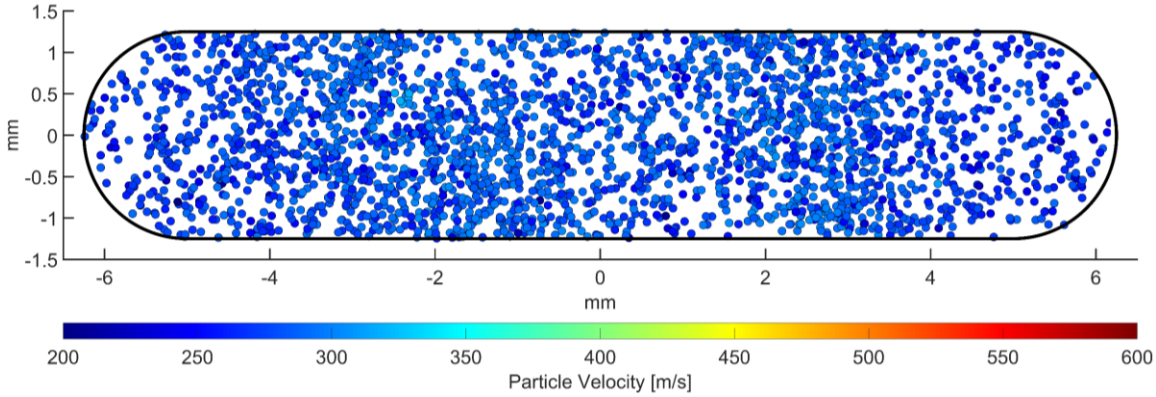

Figure B.56 – 70 µm particle distribution for the dual 15° inlets at 6.52x10^{-4} kg/s (60 SCFH)

APPENDIX C – MATLAB CODE

This appendix section shows the full code used to import particle data and represent it as a scatter plot for visualization.

```
%% Modifiers (1 = True, 0 = False)
rel_sz = 0; %Show relative size of particles (Plot of all particles)
custom_col = 1; %Set custom colorbar scale for velocity (10 - 70µm
plots)
uni_col = 1; %Set universal colorbar scale for velocity (10 - 70µm
plots)


%% Read data from file - 3 columns (X|Y|data to plot)
[num] = xlsread('TopInlet_particles_full_X-posi_filter - RWM 0.15 time
cst.xlsx');
Y = num(:,1)*1000; %Y-axis in FLUENT (m converted to mm)
Z = num(:,2)*-1000; %Z-axis in FLUENT (m converted to mm)(- sign
because axis is flipped in FLUENT)
diam = num(:,3)*10^6; %Particle Diameter (m converted to um)
vel = num(:,4); %Particle velocity (m/s)
sz = num(:,3)*1.2*10^6; %Particle Diameter (m)
pointsize = 100; %Used instead of sz for coloured points only (All the
same size)


%% Figure 1-7 Code (Scatter plot of specific size of particles)
i = 0;
while i < 7 %Loop to plot sizes from 10 - 70 µm
    i = i+1;

    switch i
        case 1
            specific_size = 10e-6;
        case 2
            specific_size = 20e-6;
        case 3
            specific_size = 30e-6;
        case 4
            specific_size = 40e-6;
        case 5
            specific_size = 50e-6;
        case 6
            specific_size = 60e-6;
        case 7
            specific_size = 70e-6;
    end

figure(i)
spec = num(num(:,3)== specific_size,:);
%Create scatter plot
%scatter(x,y, size of points, colour of points, 'filled circles')
```

```
s = scatter(spec(:,2)*-1000, spec(:,1)*1000, pointsize, spec(:,4),
'filled');
colormap(jet(256));
s.MarkerEdgeColor = 'black';
set(gca,'linewidth',2)

%Adjust figure margins
ax = gca;
outerpos = ax.OuterPosition;
ti = ax.TightInset;
left = outerpos(1) + ti(1);
bottom = outerpos(2) + ti(2);
ax_width = outerpos(3) - 1.2*ti(1) - ti(3);
ax_height = outerpos(4) - ti(2) - ti(4);
ax.Position = [left bottom ax_width ax_height];

%Set axis/dimension limits and title
hold on
title_var = specific_size*10^6;
title(['Distribution and Velocity of ',num2str(title_var),' µm
Particles - Top Inlet'])
axis equal;
axis([-6.5 6.5 -1.5 1.5])
xlabel('mm')
ylabel('mm')
c = colorbar('southoutside');
c.Label.String = 'Particle Velocity [m/s]';

if custom_col == 1
    switch i
        case 1
            caxis([250 600]);
        case 2
            caxis([300 500]);
        case 3
            caxis([250 450]);
        case 4
            caxis([240 400]);
        case 5
            caxis([200 390]);
        case 6
            caxis([200 350]);
        case 7
            caxis([200 330]);
    end
end

if uni_col == 1
    caxis([200 600]);
end

%Create nozzle shape on figure
line([-5 5],[1.25 1.25],'color','black','LineWidth',3); %top line
line([-5 5],[-1.25 -1.25],'color','black','LineWidth',3); %bottom line
```

```
th = linspace( pi/2, -pi/2, 100);
R = 1.25;
x = R*cos(th) + 5;
y = R*sin(th);
plot(x,y,'color','black','LineWidth',3); %right half-circle

a = -(R*cos(th) + 5);
b = R*sin(th);
plot(a,b,'color','black','LineWidth',3); %left half-circle

hold off
end


%% Figure 8 Code (scatter plot of all particles)
figure(8)
if rel_sz == 1
    ss = scatter(Z,Y, sz, diam,'filled'); %scatter(x,y, relative size
of points, colour of points, 'filled circles')
else
    ss = scatter(Z,Y, pointsize, diam,'filled'); %scatter(x,y, same
size of points, colour of points, 'filled circles')
end
colormap(parula(256));
ss.MarkerEdgeColor = 'black';
set(gca,'linewidth',2)

%Adjust figure margins
ax = gca;
outerpos = ax.OuterPosition;
ti = ax.TightInset;
left = outerpos(1) + ti(1);
bottom = outerpos(2) + ti(2);
ax_width = outerpos(3) - 1.2*ti(1) - ti(3);
ax_height = outerpos(4) - ti(2) - ti(4);
ax.Position = [left bottom ax_width ax_height];

%Set axis/dimension limits and title
hold on
title(['Distribution of Particles on Nozzle Exit Plane - Top Inlet'])
axis equal;
axis([-6.5 6.5 -1.5 1.5])
xlabel('mm')
ylabel('mm')
cc = colorbar('southoutside');
cc.Label.String = 'Particle Size [µm]';

%Create nozzle shape on figure
line([-5 5],[1.25 1.25],'color','black','LineWidth',4); %top line
line([-5 5],[-1.25 -1.25],'color','black','LineWidth',4); %bottom line

th = linspace( pi/2, -pi/2, 100);
R = 1.25;
x = R*cos(th) + 5;
y = R*sin(th);
```

```
plot(x,y,'color','black','LineWidth',4); %right half-circle

a = -(R*cos(th) + 5);
b = R*sin(th);
plot(a,b,'color','black','LineWidth',4); %left half-circle

hold off
%
```